Master Thesis in Geosciences

De-noising seismic data by Empirical Mode Decomposition

by

Baseem S. Saeed

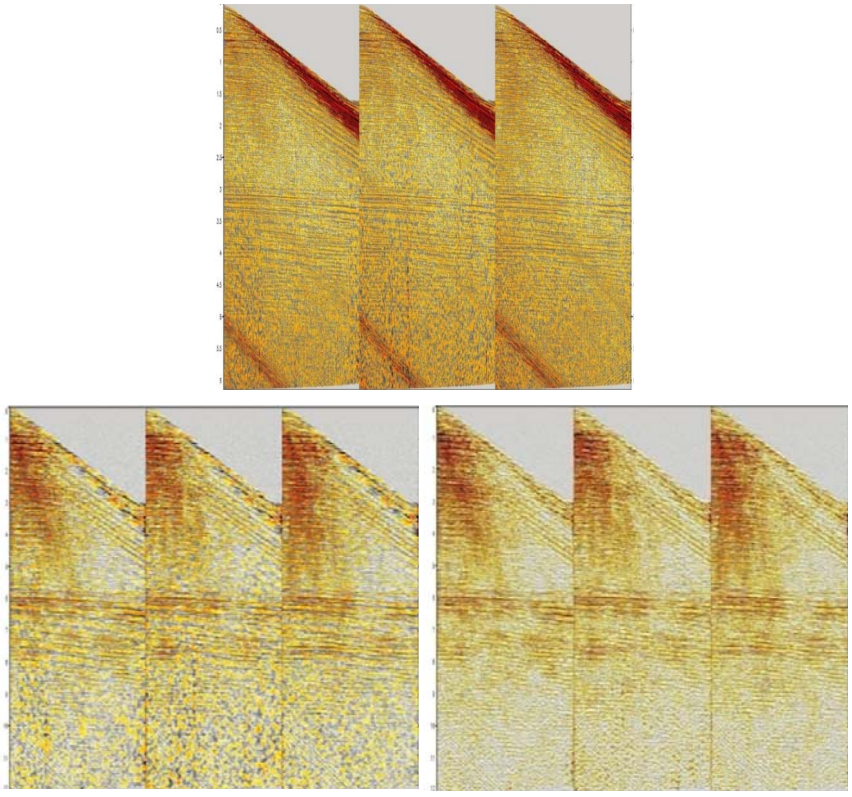

UNIVERSITY OF OSLO

FACULTY OF MATHEMATICS AND NATURAL SCIENCES

De-noising seismic data by Empirical Mode Decomposition

by

Baseem S. Saeed

Master Thesis in Geosciences

Discipline: Geophysics

Department of Geosciences

Faculty of Mathematics and Natural Sciences

UNIVERSITY OF OSLO

June 2011

Tutors: Professor Leiv-J. Gelius (UiO) and Dr. Henning Hoeber (CGGVeritas, Oslo).

This work is published digitally through DUO – Digitale Utgivelser ved UiO.

http://www.duo.uio.no

It is also catalogued in BIBSYS (http://www.bibsys.no/english)

ABSTRACT

This thesis investigates the application of the Empirical Mode Decomposition (EMD) and Ensemble Empirical Mode Decomposition (EEMD) techniques in de-noising of marine seismic data. EMD decomposes the seismic dataset into sub-datasets called Intrinsic Mode Functions (IMFs); the sum of these IMFs produces the original seismic data. EMD is a proven technique to capture the non-stationarity and non linearity of a signal; therefore, the key idea behind EMD is its use as a non-stationary filter. Marine seismic noise, such as swell, cable strum, reflected interference, ground roll, and refracted waves, causes non-stationary seismic data and represents a major challenge. Therefore, I propose to investigate in this thesis if seismic noise can be separated from target reflections by using the EMD/EEMD techniques.

The motivation of this work is to establish a reliable methodology to de-noise seismic data using the EMD/EEMD techniques. The main idea is that non-stationarity caused by noise is collected in just a few IMFs that do not carry the target (primary) reflections in the seismic dataset. The filtered section can be obtained by subtracting these IMFs from the original data leading to signal-to-noise enhancement of the data. In order to benchmark the effectiveness of the method I will compare the filtered EMD/EEMD sections to filtered reference sections generated using the GeoCluster software propriety to CGGVeritas.

In part, this thesis is an investigation of several suggestions made in the seismic literature that EMD may be an efficient method in de-noising seismic reflection data (Battista et al. (2007), Bekara and van der Baan, 2009). I shall verify if this is true in a more systematic manner than shown before. I shall also suggest some new techniques, such as the use of the EEMD method as an improvement to the previously proposed EMD methods. In another part, I attempt to improve upon the previously suggested use of the EMD/EEMD methods and propose a new application of the method to seismic data that appears more efficient than what has previously been suggested.

There are three main chapters in this thesis:

In Chapter 6, I discuss an application of the EMD technique to de-noising of seismic data in the time-space $(t-x)$ domain. Both the swell and cable strum noise are addressed. Tests on both synthetic and field datasets show that the noise distribute over all the IMFs and EMD cannot provide a good separation between the noise and target reflections, this effects is called "mixing modes". This thesis demonstrates, for the first time, that EEMD can provide a better decomposition of the seismic dataset, by reducing these mixing modes in the produced IMFs between the signal and the noise. The EEMD shows a better ability to discriminate between the signal and the noise, but both EMD and EEMD's accuracy degrades when the signal and noise fall in the same frequency bandwidth. However, the main result of this part of my thesis is that EEMD is superior to EMD in reducing mixing modes. The remainder of the work is therefore carried out with the EEMD rather than the EMD.

In Chapter 7, I investigate the application of EEMD to the de-noising of seismic data in the frequency-space $(f-x)$ domain. Constant-frequency slices of input data are decomposed to handle noise such as ambient, random, reflected interference, ground roll and refracted waves (Bekara and van der Baan, 2009). This assumes that the data are regularly sampled in space. Tests on both synthetic and field dataset show that the $f-x$ EEMD can provide a comparable filtered section compared to other filtering tools available in GeoCluster.

In Chapter 8, I propose a new filtering technique by applying EEMD to constant-time slices to target refracted events, reflected interference and swell noise assuming data regularly sampled in space. Also for the first time, we demonstrate that this technique can provide an excellent separation of the various types of noise.

Application of EMD/EEMD, either on constant-frequency slices ($f-x$ domain) or constant-time slices ($t-x$ domain), provided an improved separation of signal and noise compared with a trace-by-trace approach in the $t-x$ domain. The reason is that the decomposition of data represented by either constant-frequency or time slices deal with coherent flat and semi-fat reflection events and senses any spectral variations resulted from adding noise (i.e. random and coherent) to these events, while the decomposition of data trace by trace acts like time-variant filtering, therefore, it is hard for EMD to catch the noise located in the same signal bandwidth.

ACKNOWLEDGEMENTS

I would like to thank my advisors Professor Leiv-J. Gelius (UiO) and Dr. Henning Hoeber (CGGVeritas, Oslo) for their guidance, support and encouragement throughout my thesis work. They taught me the in-depth understanding of signal processing theories as well as the methodology of scientific research. The quality of this thesis would never been so high without their critical questions and feedbacks. Consequently, I totally recommend them for any student who wants to make valuable research in seismic signal processing.

I also thank the management team at the CGGVeritas, Oslo for the opportunity to carry out my work at the company facility. I am also grateful to the staff at the processing department, especially Sylvain de Pierrepont for helping me with Fortran 90 and GeoCluster. I consider myself totally lucky to have an opportunity to work and deal with him.

Finally, special thanks go to my family: my wife Amira, and my sons Moawia and Mustafa Saeed for their support and precious love. In more than one way, I am here largely because of you.

TABLE OF CONTENTS

1. INTRODUCTION

The main goal of noise attenuation is to condition the seismic data so that an improved and better resolved image can be obtained of the area of investigation. The objective of this thesis is to investigate the applicability and reliability of two particular de-noise techniques denoted Empirical Mode Decomposition (EMD) and Ensemble Empirical Mode Decomposition (EEMD) for de-noising marine seismic data. These methods are relatively new in the signal processing literature (Huang, 1998) and EMD has only recently been proposed for seismic processing (Battista, 2007 and Bekara, 2009). In this thesis I will investigate the properties of the EMD technique and verify the claims made in the signal processing and seismic literature. I will apply the EMD and EEMD techniques to synthetic and real data. Finally, I will propose a new way of applying EEMD to seismic data de-noising.

This thesis has been carried out in collaboration with the processing and imaging department of CGGVeritas, Oslo. I will show how the EMD method has been implemented in the processing package Geo Cluster which is proprietary to CGGVeritas and used for commercial large-scale seismic processing and imaging. I will compare the results obtained with EMD/EEMD de-noising to some of the de-noise methods routinely used in CGGVeritas' commercial processing projects.

1.1 The aim of the thesis

Marine seismic data are always contaminated by different types of random and coherent noise. Several filtering techniques are available to attenuate the seismic noise and each of these has its own range of applicability depending on the many factors characterizing the noise (and the signal) present in the data.

The EMD technique, developed by Huang et al. (1998), decomposes the data in time domain adaptively into sub-signals. One of its key features is its ability to deal with non-stationarity and non-linearity. The sub-signals can capture either the noise or the variation caused by the noise. Removing noisy sub-dataset(s) from the original data can lead to an improvement in the signal-to-noise level.

In seismic data processing, non-stationarity means that the frequency/wave-number content of the signal varies in time/space. For example, an absorptive medium can cause non-stationarity in the time dimension by making the frequency content of a seismic pulse a function of path length. Steeply hyperbolic, parabolic and linear dipping events in the $t-x$ domain can also produce non-stationary spatial signals in the $f-x$ domain at a given frequency.

The objective in this thesis is to investigate the ability of the EMD and EEMD techniques as a filter to capture the non-stationarity caused by noise and to use these methods to attenuate major types of marine noise, such as swell, cable strum, reflected interference, ground roll noise and refracted waves.

To start, my work follows the ideas of Battista et al. (2007) in the $t-x$ domain and Bekara and van der Baan (2009) in the $f-x$ domain. In addition, I then develop a new approach to attenuate reflected interference noise in the $t-x$ domain.

From a commercial point of view it is important to achieve reliable filtered results. Therefore, in this thesis, the EMD/EEMD filtered sections are compared to corresponding filtered results obtained from using the commercial processing package GeoCluster of CGGVeritas.

2. SEISMIC NOISE

2.1 Introduction

Signal-to-noise-ratio enhancement or noise attenuation is a challenging task within seismic processing because of the diversity of noise. In general, seismic noise is divided into two types: coherent noise and incoherent noise. Coherent noise can be followed across an ensemble of traces and can be predicted due to its distinct pattern; on the other hand, incoherent noise also known as random noise or background noise is unpredictable, and does not show any regular pattern from one trace to another.

Some examples of marine seismic noise (cf. Fig. 2.1) are:

- Noise from the ship engines at near offsets.
- Side-scatter of the source energy.
- Reflection from other objects like rigs and shorelines with a linear shape.
- Noise generated by other boats in the surveying area.
- Swell noise.
- Cable noise.

Some examples of land seismic noise are:

- Ground rolls also known as surface waves of Rayleigh type characterized by high amplitudes, low frequencies, and low propagation velocity. Because of the dispersive character of this type of noise, shallow reflections at short offsets and deeper reflections at larger offsets are masked and their waveforms are distorted.
- Side-scatter of source energy reflected from other objects, being either linear or random.
- Electric noise around 55Hz.
- High levels of random noise.

- Linear noise caused by refractions.

In seismic acquisition, reflections are recorded that arise from the interaction between the incident wave fields and the in-homogeneities within the Earth's subsurface. The recorded seismic data can be represented formally as:

$$\boldsymbol{y = m + n} \qquad \textbf{(2.1)}$$

where ***y*** is the noisy data, ***m*** is noise free data, and ***n*** represents the noise. The main objective of seismic data processing is to recover ***m***. The seismic data is usually contaminated with both incoherent and coherent noise.

Sheriff and Geldart (1995) used the term *signal* to refer to any event on the seismic record from which one wishes to obtain information, everything else is *noise*. Russell et al. (1990) defined noise as "*anything on the seismic data that does not fit our conceptual model of the data, that is, as clean seismic reflections"*.

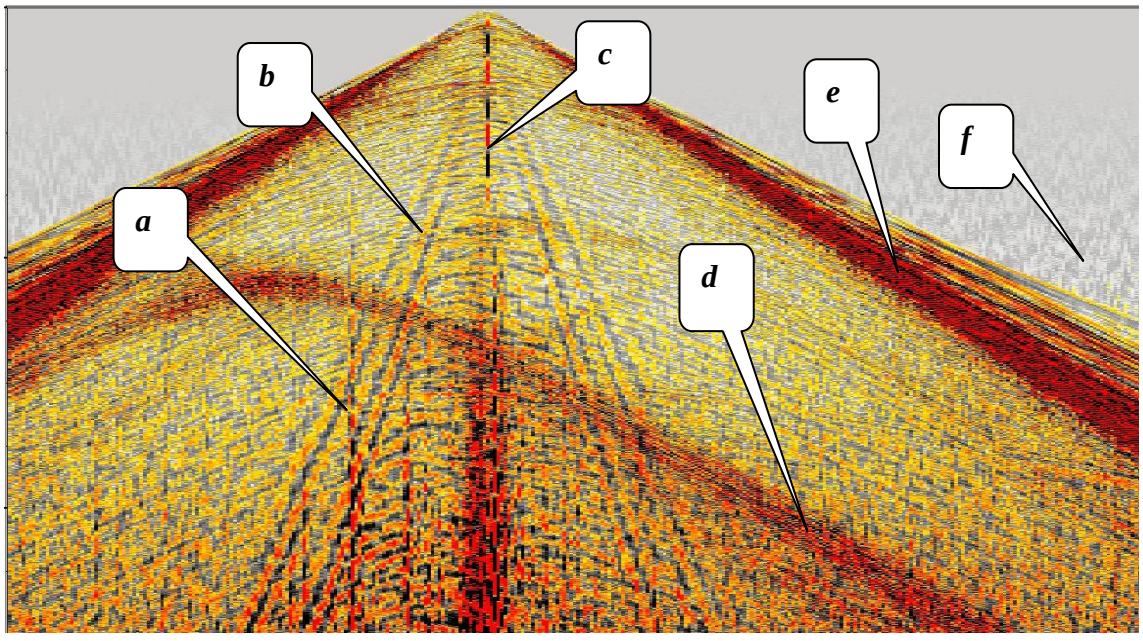

Figure 2.1: *Noise associated with marine surveying (Ocean Bottom Cable (OBC)):* ***(a)*** *Swell noise.* ***(b)*** *Ground rolls waves.* ***(c)*** *Cable noise.* ***(d)*** *Interference noise.* ***(e)*** *Refraction and Direct waves.* ***(f)*** *Ambient noise (after CGGVeritas).*

2.2 Classification of noise

Seismic noise is divided into *coherent* and *incoherent noise.* These two types of noise can often be discriminated in the frequency domain. Coherent noise like swell noise is low frequency due to rough weather conditions whereas random noise is high frequency due to the short radiation path in the near surface (Li and Tang, 2005). This is shown schematically in Fig. 2.2 in case of land data. Measuring the noise levels can be done by using different criteria such as: amplitude; frequency/phase; coherency, and apparent velocity.

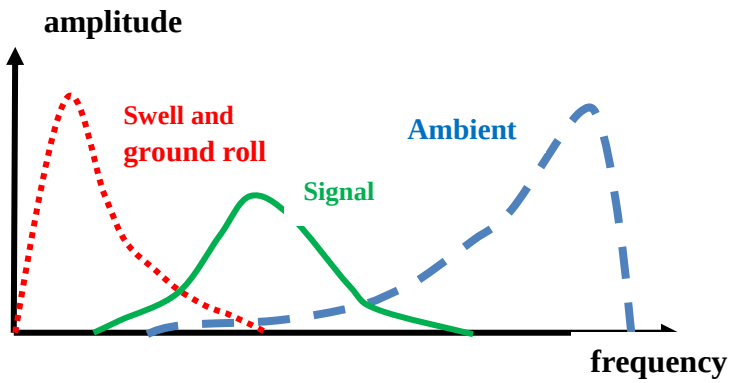

Figure 2.2: *Typical distribution of signal and noise frequencies in a land seismic record. Seismic bandwidth is defined by a combination of signal and noise bandwidths. Coherent noise is low frequency whereas random noise is high frequency (re-plotted from Li and Tang (2005)).*

2.2.1 Coherent noise

According to Telford, Geldart and Sheriff (1990), coherent noise can be divided into (a) noise that travels essentially horizontally and is repeatable (b) noise that reaches the spread more or less vertically. The three properties that characterize coherent noise are: coherency, travel direction, and repeatability. Coherent noise includes multiples, ghosts, ground rolls, swell, surface waves, reflections from near surface structure such as platforms, or buried objects and refracted waves.

Coherent noise can be removed by using $f-k$ filtering techniques, radon transform, and $f-x$ projection filters and includes also spatially repeated incoherent random noise due to scattering from the surface.

2.2.2 Non-coherent (random) noise

This type of noise is described as spatially random and eventually repeated due to scattering from near surface irregularities such as boulders, and small-scale faulting (Telford, Geldart, and Sheriff 1990). Random noise caused by wind sharking a geophone or a person walking near geophones.

Random noise is nearly always assumed to be a stationary stochastic process uncorrelated with the signal and all the coherent noise wave-trains. Its spectral (autocorrelation) function is trace-independent to within a scale factor, the variance.

Since non-coherent noise is random in a statistical sense, the sum of n signals will give an improvement of the signal-to-noise ratio of $\sqrt{n}$ (Telford, Geldart, and Sheriff, 1990). Hence, the use of multiple receivers (hydrophones) or multiple sources (air guns) will lead to noise cancellation.

Random noise is attenuated by trace stacking during seismic data processing. Vertical stacking involves combining several records and is extensively used in case of weak surface sources. In marine seismic vertical stacking rarely involves more than 4 records to avoid data being too much smeared when stacked. Random noise should be attenuated before stack, since most of the high amplitude noise often survives the stacking stage (Telford, Geldart, and Sheriff, 1990).

2.3 Signal-to-noise ratio (SNR)

The signal to noise ratio can be estimated for seismic traces inside certain discrete zones or windows where the signal is present. In this thesis, I used two approaches to calculate SNR for the seismic sections.

The root-mean-square amplitude (RMS amplitude) relates to the average amplitude of a seismic trace inside a given time window. This window can either be the entire trace or a portion. The formula for the RMS amplitude is as follows:

$$r = \sqrt{\frac{1}{N}\sum_{i=1}^{N} x_i^2} \qquad \textbf{(2.2)}$$

where, N is the number of samples inside the selected window or alternatively the entire seismic trace, and x_i is the amplitude of the i^{th} sample.

The SNR ratio can be estimated inside a window as follows:

$$\frac{\textbf{RMS amplitude of the signal}}{\textbf{RMS amplitude of the noise}} \qquad \textbf{(2.3)}$$

The second approach used is implemented in CGGVeritas own processing software. A rectangular window (or group of traces) of data is selected. The main assumption is that the signal is coherent within adjacent traces while the noise is random, therefore, SNR can be estimated as follows:

- The first dataset can be computed by averaging the sum of all the auto correlation obtained from each trace.
- The second dataset can be computed by averaging the sum of all cross correlation for all adjacent traces.

- Compute the amplitude spectrum for both of the datasets by using Fast Fourier Transform (FFT). Hence, the amplitude spectrum of the second dataset is considered as signal while the amplitude spectrum of the first dataset is considered as signal and noise spectra.
- The noise spectrum is obtained by subtracting the second dataset spectrum from the first dataset spectrum.

The reader can be referred to Hatton (1986) for more details.

2.4 Noise associated with marine seismic

A brief discussion is given. For a wider discussion of noise the reader is referred to Olhovich (1964) and Gelius and Westerdal (1997).

2.4.1 Water bottom multiples and Ghost reflection

Multiples result from internal reflections in a layer when the seismic energy is trapped between two strong reflectors such as the water layer. Fig. 2.3 shows an example of such water bottom multiples. The geometry of a marine seismic acquisition also introduces a special type of multiple denoted a ghost.

The source signal will be more or less affected by the source ghost reflection from the sea surface which has a reflection coefficient close to (-1) except for rough weather. For example, placing the source at a depth of 7.5m, gives notch frequencies at 0, 100, 200, and 300 Hz. Hence, the ghost interference is minimized at such a depth. Receiver side ghosts also exist and constrain the effective towing depth of the streamer (cf. Fig. 2.4). De-ghosting techniques both for source and receiver are currently receiving wide attention in the geophysical community.

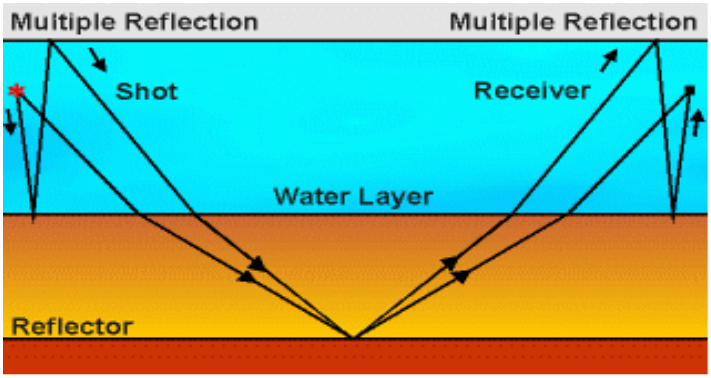

Figure 2.3: *Water bottom multiples in marine acquisition (after CGGVeritas).*

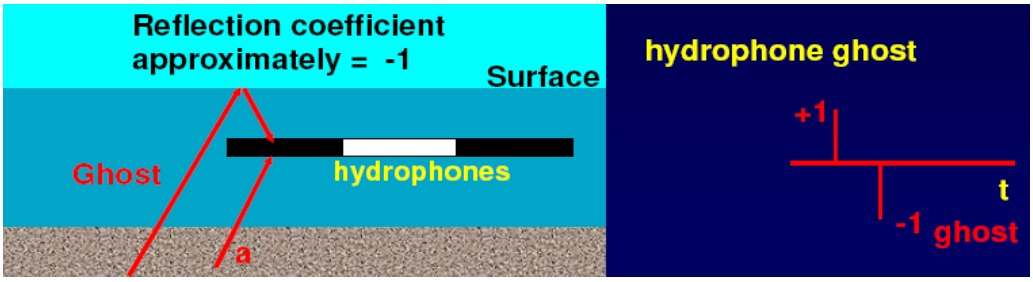

Figure 2.4: *Hydrophone ghost (after CGGVeritas).*

In case of seafloor seismic, geophones are used as marine sensors and placed directly on the sea-bottom (e.g. Ocean Bottom Cable (OBC)). The geophones measure the particle velocity field, and are directional sensitive (e.g. sensitive to the direction from which the seismic wave is coming). The ghost phase undergoes reversal at the surface but hits the geophone in the opposite direction; therefore the ghost is recorded with the same polarity as Fig. 2.5 illustrates.

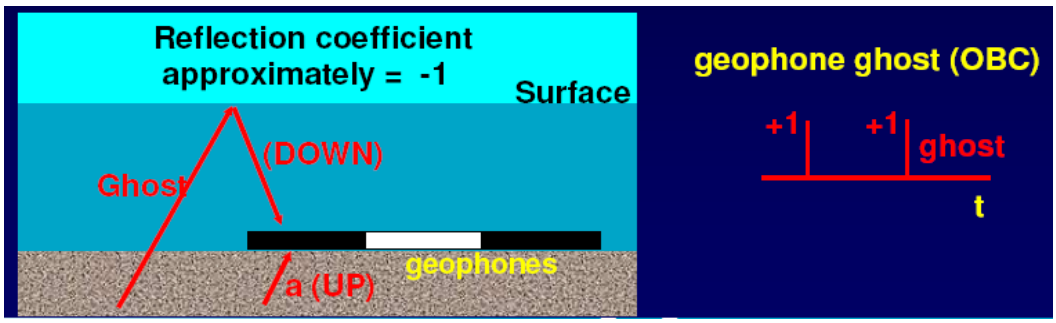

Figure 2.5: *Geophone ghost (after CGGVeritas).*

2.4.2 Swell noise

Swell-noise is large amplitude noise that normally falls within the frequency bandwidth from 2-15 Hz (cf. Fig. 2.1a). It affects an ensemble of neighboring traces, and can be observed on the seismic data as vertical stripes. Generally, swell noise arises from rough weather conditions during marine acquisition especially in shallow water. Elboth et al. (2009) has presented two different mechanisms that generate swell-noise: (1) fluid-filled streamers can generate a transversal motion called Bulge waves which gives rise to high-amplitude noise up to 10 Hz (most modern steamers are able to reduce the Bulge waves); (2) strong pressure fluctuations such as: (a) hydrostatic- pressure fluctuations caused by the vertical motion of the ocean as a result of strong sea waves, (b) dynamic pressure variations along the surface of the streamer that result from the presence of a turbulent layer surrounding it.

2.4.3 Surface waves (Ground roll)

Surface waves are common on land seismic sections, and also in marine seafloor acquisition. Surface waves are considered as coherent linear noise with high amplitudes, low frequencies, low velocities and of dispersive nature with each frequency component having its own propagation velocity (cf. Fig. 2.1b).

There are two types of surface waves:

- Rayleigh waves having a displacement in the inline $(x - z)$ plane (cf. Fig. 2.6) and representing a combination of P and SV motion.
- Love waves resulting from SH waves trapped near the surface, and with a displacement being parallel to the cross-line direction $(y\ axis)$ as shown in Fig 2.6.

Conventionally, ground roll is removed by using frequency-wave-number (f-k) or frequency-space $(f - x)$ methods (Yilmaz, 2001). However, since the near surface heterogeneities cause the ground roll to be scattered in the cross-line direction, these conventional techniques can prove to be ineffective since the cross-line scattered ground roll can occupy the same regions of $(f - k)$ and $(f - x)$ space as the reflected waves needed to be preserved.

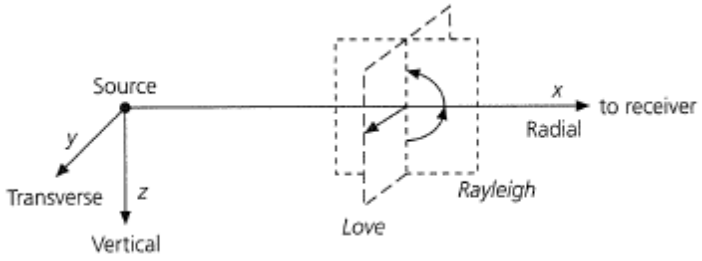

Figure 2.6: *Geometry of surface waves propagating in a vertical plane. Rayleigh (P-SV) waves appear on the vertical and radial components. Love (SH) waves appear on the transverse components (Stein, 2003).*

2.4.4 Cable noise

Cable noise is also known as cable strum noise and is caused by the motion of the cable through the water, wave action, and leakage. It is a very strong coherent noise characterized by low-frequency non-linear events. Strum noise is mostly evident on the outer cable. The energy of the cable noise increases in shallow water as is also the case for swell noise. A low-cut filter can be used to remove cable noise from the shot records (cf. Fig. 2.1c).

2.4.5 Seismic interference noise

Seismic interference (SI) noise is caused by another vessel operating nearby to the acquisition or obstructions that reflect or diffract the recording energy in the same surveying area. SI noise is wide banded, and can often have large amplitudes compared to the subsurface reflection data and appears on the seismogram as hyperbolic or umbrella shaped events (cf. Fig. 2.1d and Fig 2.7).

By making use of the different move-out behavior of the seismic signal, SI noise can be removed by Radon transform, since this noise is mapped into an area that can be muted in the transformed $(\tau - p)$ domain.

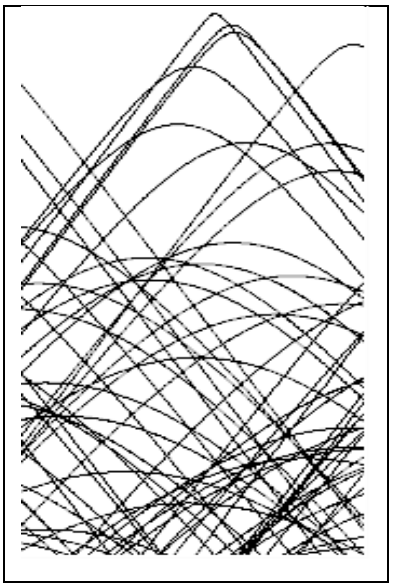

Figure 2.7: *Seismic interference noise (after CGGVeritas).*

2.4.6 Refraction and direct wave

Refraction is caused when the energy is trapped along a boundary between rapidly changing shallow velocities and then leaks up to the surface. Refracted energy will be recorded as straight lines crossing the seismic data. The direct wave travels directly from the source to the receiver with the surface (water) layer velocity (cf. Fig. 2.1e).

2.4.7 Ambient disturbance

Ambient noise does not originate from the marine acquisition itself, and usually affects the recording data from zero time to 10 ms above the first breaks (cf. Fig 2.1f). It is characterized by high frequencies, and always low amplitudes. Examples of ambient noise are lightning, rain, wind, power lines, passing vehicles, and marine life. Low pass filtering is used to filter ambient noise.

3. COMMON TECHNIQUES EMPLOYED TO ATTENUATE NOISE

Since noise normally contains appreciable energy outside the principal frequency band of the signal (cf. Fig 2.2), the use of frequency filtering can be advantageous. Very low-frequency components (such as high-energy surface waves rich in low frequencies) may be attenuated during the initial recording provided the low frequencies are sufficiently separated from the reflection frequencies. However, when the noise spectrum overlaps the signal spectrum frequency filtering can be of limited value in improving the record quality.

This chapter will start with an introduction to data sorting and gathering because these concepts are important when addressing noise and noise attenuation.

3.1 Review of data sorting and gathering

Before the actual process of seismic data analysis can start, proper geometry information must be established for each trace. This is fairly simple for 2-D marine data, but much more complex in case of 3-D. The parameters defining the geometry information are written in each trace header and can be used to select proper subsets of data in the further processing (sorting data). Seismic data are normally sorted in the following types of gathers:

3.1.1 A common shot gather gives a continuous subsurface coverage. Figure 3.1 shows twelve parallel 2-D seismic lines acquired over a single reflector with each line defined by one shot and five receivers. Common shot gathers represent an initial data sorting and these shot records can be further processed in early stages of the data analysis. Each shot provides a short slice of the sub-surface geology, but the information about the sub-surface geology will be distorted since each successive trace comes from a different receiver group offset by a different distance from the shot.

To obtain a continuous offset representation of the sub-surface, data must be sorted in Common Mid Point (CMP) gathers.

3.1.2. A common receiver gather represents all traces coming from the same receiver group. The common receiver gather is used to isolate problems associated with individual receivers. Associating bad traces with a particular receiver may be difficult until common receiver gathers are viewed. Figure 3.1 shows all rays recorded at a single receiver due to several shots. Common-receiver sorting is mostly used for static corrections in land seismic.

3.1.3 A common midpoint (CMP) gather consists of traces corresponding to a midpoint or symmetry point (cf. Fig. 3.1). This type of the sorting is needed to carry out classical velocity analysis and NMO correction. After such correction all traces in a CMP are stacked to increase the SNR.

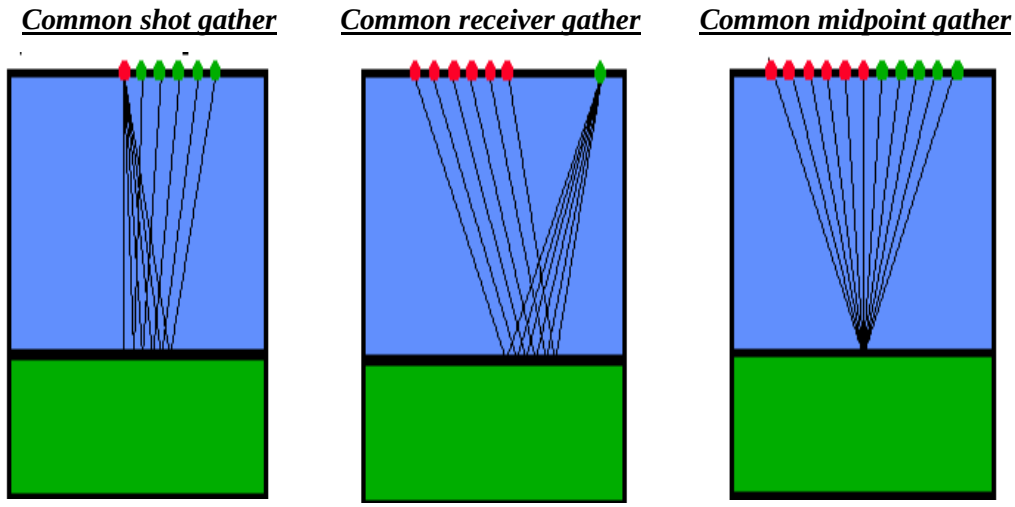

Figure 3.1: *Different types of gathers, shots are red and receivers are green (source: Excess Geophysics).*

Acquisition and processing are clearly linked in many ways, not least the resolution of the final image we can obtain. The acquired data depends on the locations of the sources and those of the receiver. In this high-dimensional space we can visualize, and also process, the data in different configurations or sorting domains.

In these different domains the kinematics of the wave propagation in the earth lead to different relationships between the energy returned to the surface across the traces. This can be used to our advantage by finding the best data sorting domains for the signal processing. The idea used most often is to find the domain in which previously coherent noise becomes more random and is this more amenable to random noise attenuation techniques.

As an example, Figure 3.2 shows the same data with different types of sorting. The shear waves appear as coherent noise in a receiver (streamer) gather and as random noise in CMP and shot gathers which make shear waves easier for attenuation using frequency filters.

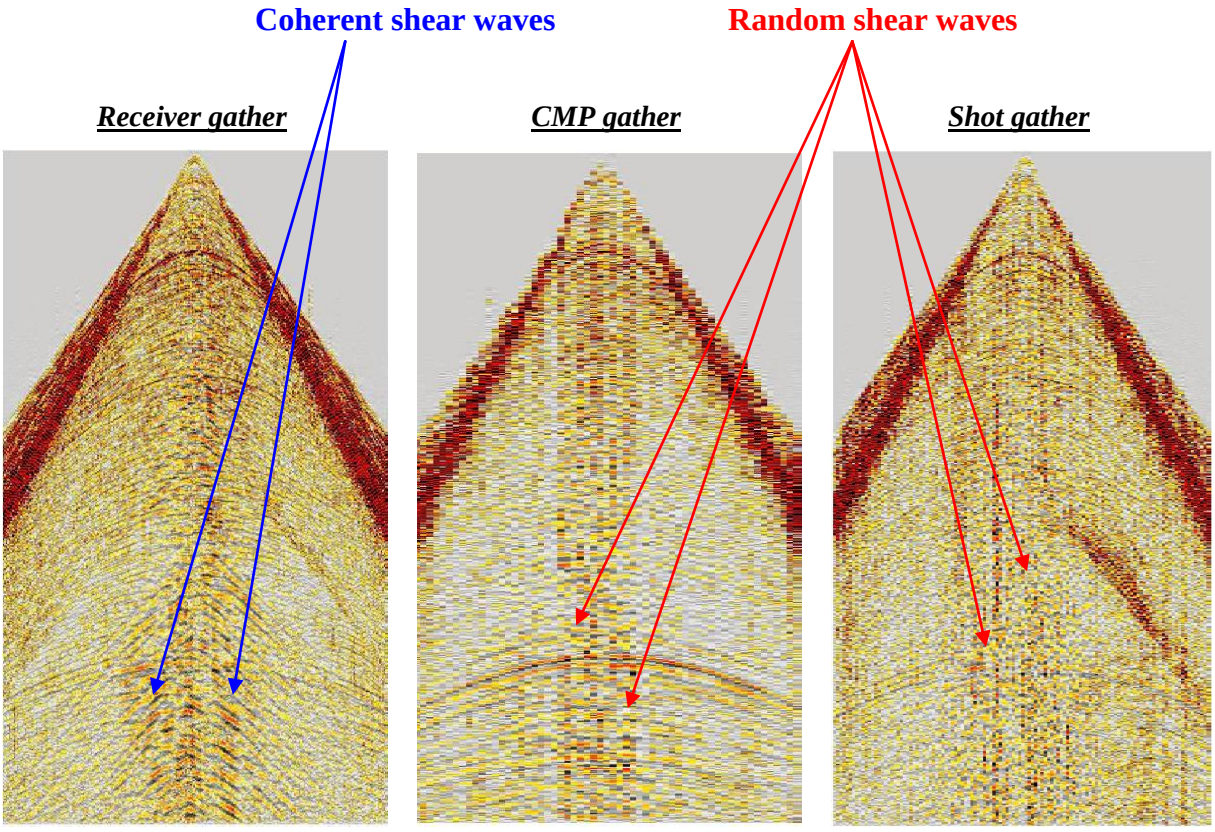

Figure 3.2: *Different types of sorting for same data.*

The next section is a review of some commonly used filtering techniques in seismic data analysis. These methods are also applied in this thesis when benchmarking the new techniques.

3.2 Frequency filtering

Frequency filtering is a suitable method to remove noise that does not fall in the signal frequency band. Example can be low frequency swell noise, and ground roll, or high frequency thermal noise. Band pass filtering can be used to remove both low and high frequencies from seismic traces. It can be carried out in the frequency domain by using a zero-phase filter that only change the amplitude spectrum of the original signal. When constructing a frequency filter tapering has to be applied at its edges to avoid ringing. Key parameters to specify are cut-off frequencies and the slope of the taper.

Example of frequency filters are shown in Fig. 3.3. A low-pass filter with high cut and a high pass filter with low cut are just special cases of a band-pass filter. The typical original bandwidth of a seismic signal is between 10 - 70 Hz with a dominant frequency around 30 Hz (Yilmaz, 2001). Due to attenuation effects the signal bandwidth will be reduced according to propagation length.

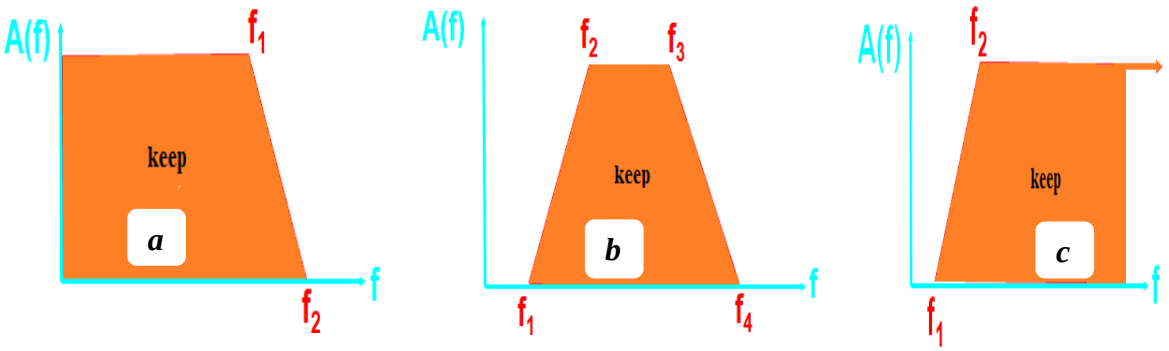

Figure 3.3: *Frequency filters:* ***(a)*** *Low-pass filter (high cut).* ***(b)*** *Band-pass filter.* ***(c)*** *High-pass filter (low cut).*

In Fig. 3.4, a band-pass filter with frequency corners of 15, 20, 60 and 70 Hz was applied to the receiver gather shown at the top containing both low frequency swell noise and ground roll, and high frequency ambient noise. Use of the band-pass filter efficiently removed the low-frequency noise as well as the ambient noise.

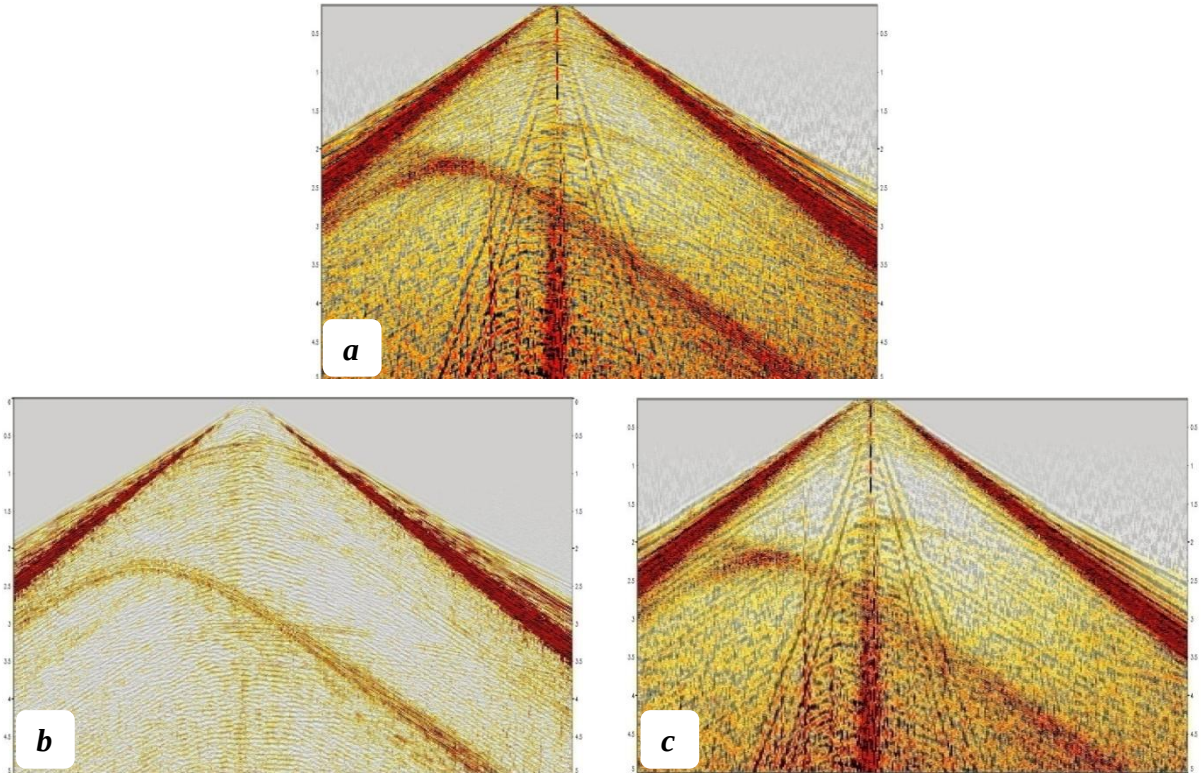

Figure 3.4: Example from a North Sea Data. *Band-pass filtering:* ***(a)*** *Marine receiver gather.* ***(b)*** *Band-pass filtered result using frequency corners of 15, 20, 60 and 70 Hz.* ***(c)*** *Difference data.*

3.3 $F - X$ deconvolution

Frequency-space deconvolution is a technique which can remove coherent and random noise from seismic traces. It operates in the frequency-space $(f - x)$ domain, so each trace is Fourier transformed with respect to time.

3.3.1 Signal model in $f - x$ domain

Canales (1984) and Gulunay (1986) describe how a linear event in the $t - x$ domain can be mapped into the $f - x$ domain of each trace.

Assume a delta-pulse so that a linear event in $t - x$ domain can be described as:

$$\boldsymbol{s(x,t) = \delta(dx - t)} \quad \textbf{(3.1)}$$

where d represents the slope or dip. After taking the Fourier Transform, this linear event can be described in the $f - x$ domain as follows:

$$\boldsymbol{S(x,f) = e^{i\,(2\pi f)dx}} \quad \textbf{(3.2)}$$

$$\boldsymbol{S(x,f) = \cos(2\pi f\, dx) + i \sin(2\pi f\, dx)} \quad \textbf{(3.3)}$$

From Eq. (3.3) it follows that for a simple linear event, this function is periodic in $\boldsymbol{x}$.

Introduce now sampling along x-axis i.e. $x = n\,\Delta x$, where n = 1, 2, 3, …,N, and with N being the total number of traces considered:

$$\boldsymbol{S_f(n) \equiv S(x_n, f) = e^{i(2\pi f)\, d\, n\, \Delta x}} \quad \textbf{(3.4)}$$

From Eq. (3.4), it follows that a given trace value $\boldsymbol{S_f(n)}$ can be predicted from its neighboring trace through (assuming frequency $\boldsymbol{f}$ constant):

$$\boldsymbol{S_f(n) = a(f)\, S_f(n-1),\ \ n \geq 2} \quad \textbf{(3.5)}$$

where $a(f) = e^{(i\,(2\pi f)\, d\ \Delta x)}$. This recursion is known as an autoregressive (AR) model of order 1.

Eq. (3.5) suggests that this event is perfectly predictable with a complex Wiener filter (Canales, 1984; Gulunay 1986; Hornbostel, 1991). In practical applications a unit-delay predictive filter is applied. Alternatively, one may solve the prediction problem by using an AR model (Tufts and Kurmaresan, 1982; Harris and White, 1997).

In case of linear events characterized by non-Dirac pulses and different dips, Eq. (3.2) is replaced by:

$$\boldsymbol{S(x,f) = W_1(f)e^{i\,(2\pi f)\,d_1\,x} + W_2(f)e^{i\,(2\pi f)\,d_2\,x} + \ldots\ldots + W_n(f)\,e^{i\,(2\pi f)\,d_n\,x}} \qquad \textbf{(3.6)}$$

where $W_1(f)$, $W_2(f)$,… $W_n(f)$ represent the frequency spectra of the linear $t - x$ events.

Fig. 3.5 shows an example where $f - x$ deconvolution is used to attenuate interference noise e.g. strong coherent noise from a nearby marine acquisition.

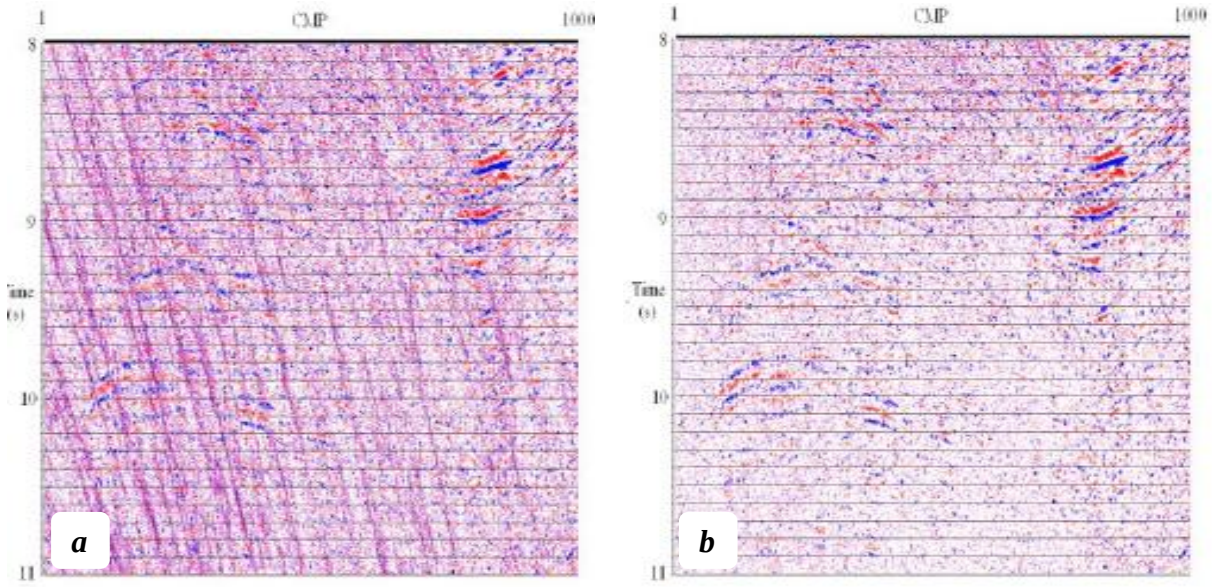

Figure 3.5: *FX-deconvolution filtering* ***(a)*** *Input data* ***(b)*** $f - x$ *deconvoluted output (adapted from Gulunay et al. 2001).*

3.3.2 Problems associated with $f - x$ deconvolution

The $f - x$ deconvolution can be problematic when handling non-stationary signals (resulting for example from dispersion of high frequency and ghost events). To handle this problem a short sliding window can be used assuming that the data inside the window are stationary (Galbraith, 1991).

Another problem associated with $f - x$ deconvolution stems from lack of handling non-linear seismic events. The $f - x$ prediction is therefore applied within small windows to ensure that

events are locally linear. Each calculated filter is first applied forward and then reversed in space, with the result arranged to maintain a symmetrical application.

Short temporal and spatial analysis windows are used in $f-x$ deconvolution to assume that the data within the window are piecewise linear and stationary. Use of windows lead to some failure in the $f-x$ deconvolution process especially when handing data from a complex geology acquired using an irregular geometry. $F-x$ prediction gives fairly good results for random attenuation, but is not amplitude preserving (Canales, 1984).

3.3.3 Relevant $f-x$ deconvolution modules in GeoCluster

The module FXNAT performs random noise attenuation in the $f-x$ domain without affecting spatially coherent events. It can be applied to receiver, shot, and CMP gathers, and post stack data. It assumes that the signal is predictable, and the random noise not and it uses spatial and temporal blocks which define a sliding window in 2D for each frequency. FXYNA is a 3D version of FXNAT which is used to attenuate random noise in the F-XY domain.

The SPARN (Signal Preserving Attenuation of Random Noise) module represents the most commonly used $f-x$ domain filter to attenuate high amplitude noise such as swell-noise and random noise. It uses projective filtering techniques that separate the signal (assumed to be predictable) from noise (non-predictable) and preserves the signal amplitudes. PRF3D is a 3D equivalent of SPARN.

SPARC is the cascaded version of SPARN over the frequency band, and the output from one SPARN is fed directly into the input of the next SPARN, so SPARC calls SPARN at each frequency step to decrease the computational speed. Fig 3.6 shows an example where SPARC has been applied to remove swell noise.

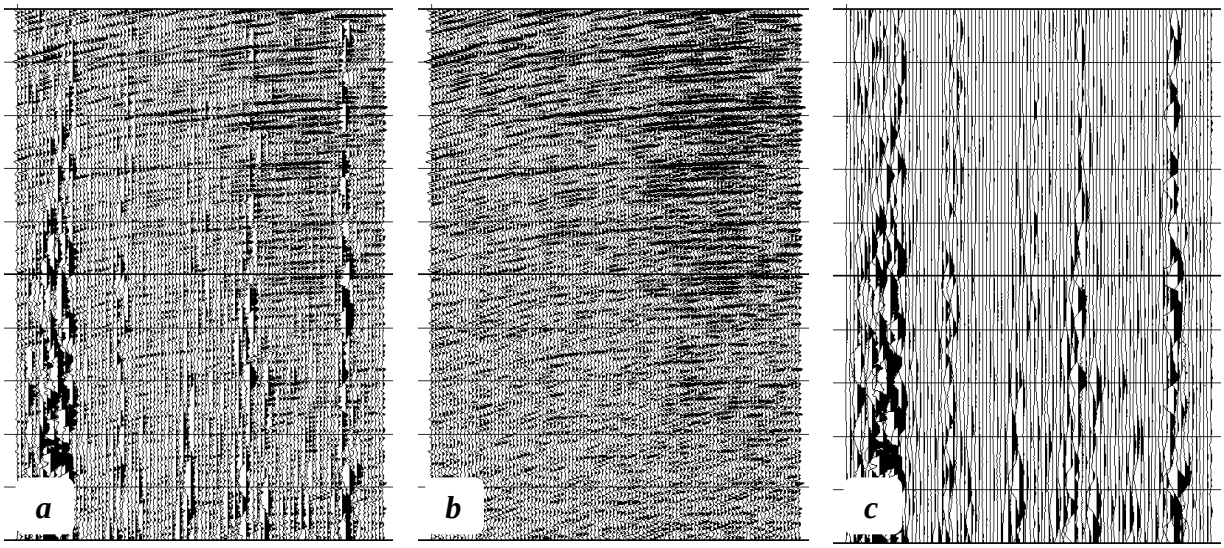

Figure 3.6: *SPARC filtering:* ***(a)*** *Input marine shot gather.* ***(b)*** *Filtered data.* ***(c)*** *Removed swell noise (source CGGVeritas).*

3.4 Frequency-wave number (*f-k*) filtering

F-K filtering is a filtering method used to attenuate linear coherent events. It is based on a 2D Fourier transform. This technique distinguishes between the signal and the noise based on their relative apparent velocities. Linear coherent noise is characterized by apparent velocities differing significantly from those of the reflection events. Such noise can therefore be attenuated by muting in the $f-k$ domain. Filtering is based on defining a rejection zone corresponding to unwanted energy (or apparent velocities). The rejection zone must be neither too wide so that it suppresses signal contributions in the pass zone nor too narrow. Hence, there must be a smooth transition from the reject zone to the pass zones (i.e. tapering of edges). $F-K$ filtering fails when the apparent velocity range defining the noise significantly overlaps those governed by the reflection or when the noise mode exhibits a large amount of dispersion.

In GeoCluster, the **FKFIL** (**F**requency-**K**(Wave-number) **FIL**ter) module uses 2D *f-k* filtering to attenuate coherent linear noise either in marine or land data. FKF3D is a 3D version of FKFIL which represents FKxKy filtering of acquisition footprint and dipping noise, and is commonly used on land data.

3.5 Radon transform

Linear Radon transform is known as Tau-P transformation or Slant Stack. It maps the data in the time offset domain based on the local slope of events p (ray parameter) against their intercepts at the time axis τ (Diebold and Stoffa, 1981). Linear events in the $t-x$ domain such as refracted events, direct wave, sound (air) waves, and ground roll map into points and hyperbolic events become ellipses in the $\tau-p$ domain. Consequently, removal of specific coherent events can be easier. After removing the unwanted parts in the $\tau-p$ domain the data are transferred back to the $t-x$ domain employing an inverse Radon transform.

Linear Radon transform can be generalized to hyperbolic or parabolic analyzing windows in space and time. These generalized Radon transforms can be used in multiples attenuation, and to weaken interference noise. The RAMUR module in GeoCluster does Parabolic Radon Transform. Figure 3.7 gives an example where RAMUR has been applied to filter interference noise.

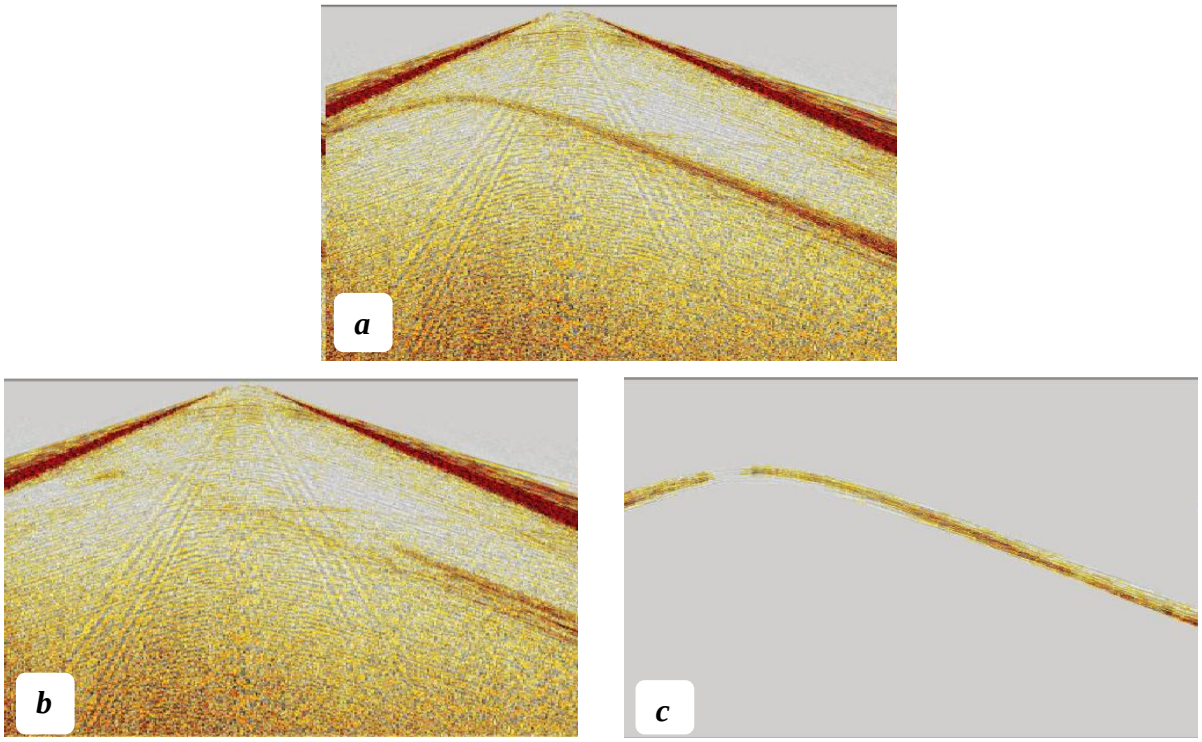

Figure 3.7: *RAMUR filtering:* ***(a)*** *Marine receiver gather.* ***(b)*** *RAMUR result.* ***(c)*** *Removed noise.*

4. EMPIRICAL MODE DECOMPOSITION (EMD)

4.1 Introduction

Time series data such as seismic recordings are often assumed to be stationary and linear at least within a given window. Dealing with non-stationarity and non-linearity of the signal is a challenge as these effects are obviously linked with the size of this window.

EMD was initially designed for use in combination with the Hilbert transform for detecting instantaneous changes in the time frequency content of a temporal signal. The correct detection of instantaneous changes in the signal may then reveal anomalies of the object that generated such a signal.

The Empirical Mode Decomposition is similar to the Short Time Fourier transform (STFT) and the wavelet transform, providing an adaptive decomposition of a signal either in the time or frequency domain, capturing the non-stationarity of the input signal. The main advantage of EMD over these alternative techniques is that it gives an automatic decomposition which is fully data adaptive, and does not require a presumed set of functions like the wavelet transformation.

The EMD method has been applied within several areas of signal processing such as financial applications (Huang et al., 2003), fluid dynamics and ocean engineering (Rao, 2008) as well as electromagnetic time series analysis (Karagiannis, 2009). Margin-Chagnolleau and Baraniuk (1999) were among the first to apply the EMD method trace by trace in the time-space domain and Battista et al. (2007) have suggested that EMD can be used to remove cable strum noise from marine seismic data.

This chapter gives a discussion of the basics of EMD, both from a theoretical as well as a practical point of view.

4.2 Intrinsic Mode Function (IMF)

By applying EMD a signal can be decomposed into a set of monocomponent functions called Intrinsic Mode Functions (IMFs) (Huang et al., 1998). A monocomponent function indicates an oscillating function close to the most common and basic elementary harmonic function. Therefore, the IMFs contain frequencies ranging from the highest to the lowest ones of the signal presented as amplitude and frequency modulated (AM-FM) signals, where the AM carries the envelope and the FM is the constant amplitude variation in frequency and calculated using a sifting process. To accomplish this, an IMF must satisfy two conditions (cf. Fig.4.1):

1) The number of extrema (local maxima and minima) and the number of zero crossings must either equal or differ at most by one.

2) At any point, the mean value of the envelope defined by the local maxima and the envelope defined by the local minima is zero.

The first condition is necessary for oscillating data to meet the strict conditions needed to calculate the instantaneous frequency that presents the oscillation frequency of a signal at certain point of the time (Huang et al., 1998 and 2009). It leads to a narrow-band signal. The second condition requires symmetric upper and lower envelopes of an IMF which makes the signal ready for modulation as the IMF component is decomposed from the original data (Huang et al., 1998, 2005 and 2008). It is quite challenging to find the envelopes because of the nonlinear and non-stationary nature of the data. Only a few functions have such characteristic envelopes, for example, the constant amplitude sinusoidal function.

Figure 4.1 shows an example of an IMF, where the green curve represents the actual IMF, the red line its upper envelope, the blue line its lower envelope, and the black line represents the mean of the envelopes. In this case, the IMF has 17 zero crossing and 16 local extrema, and the symmetry of the two envelopes leads to their zero mean value.

The main idea behind IMF is to separate the data into a slowly varying local mean part and a fast varying symmetric oscillatory part, with the latter part becoming the IMF and the local mean defining a residue. This residue serves as input for further decomposition, with the process being repeated until no more oscillations can be obtained.

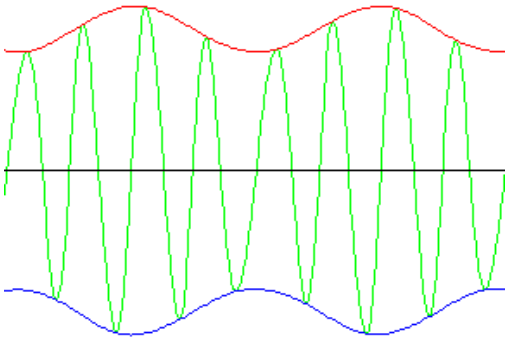

Figure 4.1: *Example of an Intrinsic Mode Function (IMF), (green curve) with corresponding envelopes.*

As an oscillatory mode, the amplitude and frequency of an IMF will vary with time in a way which is locally symmetrical and monocomponent. Hence, the instantaneous frequency can be calculated in a meaningful way (Huang et al., 2005).

EMD is based on three assumptions: (1) the signal has at least one minimum and one maximum (non-monotonic function), (2) the time difference between successive extrema defines the characteristic time scale, (3) if there are no extrema but only inflection points, the data may be differentiated, then EMD applied and the result obtained by integrating the components (Huang et al., 1998).

The characteristic time scales are used to find the intrinsic modes. A signal can be thought of as higher-frequencies waves riding upon lower-frequencies carrying waves. Each wave has its own characteristic scale. Thus, the features of the original signal are still present in the IMFs extracted by EMD because IMFs are created by searching the riding waves. In addition, the EMD process can reveal oscillations that are not clearly visible to the human eye in the original signal (Huang et al., 1998).

4.3 Sifting Process for finding the IMF

The objective of EMD is to obtain a series of oscillatory-component intrinsic mode functions (IMF) representing the input signal. A sifting process is applied to iteratively separate the different oscillatory riding components of the signal, starting with the fastest and ending with the slowest component. By adding all the IMFs the original signal can be recovered. The three assumptions mentioned above must be met before starting this sifting process.

4.3.1 Finding the first IMF

Finding the first IMF, which presents the fastest (highest) oscillatory mode in the signal, is done by using two loops. Denote a sub signal going through a sifting process as $h_{nk}(t)$,where the first index is the IMF number, $n = 1, 2,\ldots N$, and the second index is the iteration number, $k= 1, 2,\ldots K$, of the sifting process **(**cf. Fig.4.2a).

To find the first IMF of a given signal $x(t)$ follow these steps:

1) Set the initial value $h_{10,}$ equal to the signal $x(t)$ and find the extrema (local maxima and local minima points) of the input signal. (cf.fig.4.2a).

2) Connect the maxima with spline functions to form the upper envelope $e_{upper}(t)$ and connect the minima with spline functions to form the lower envelope $e_{lower}(t)$ (cf.4.2b)**.**

3) The mean of the envelope is now calculated as:

$$m_{11}(t) = \frac{e_{upper}(t) + e_{lower}(t)}{2} \qquad \textbf{(4.1)}$$

4) Subtract this mean from the input or initial signal:

$$h_{11}(t) = h_{10}(t) - m_{11}(t) \qquad \textbf{(4.2)}$$

Step 1 to 4 is one iteration of the sifting process (cf. Fig. 4.2c).

In practice this cycle has to be repeated until one or several stopping criteria have been fulfilled (see Fig. 4.2d).

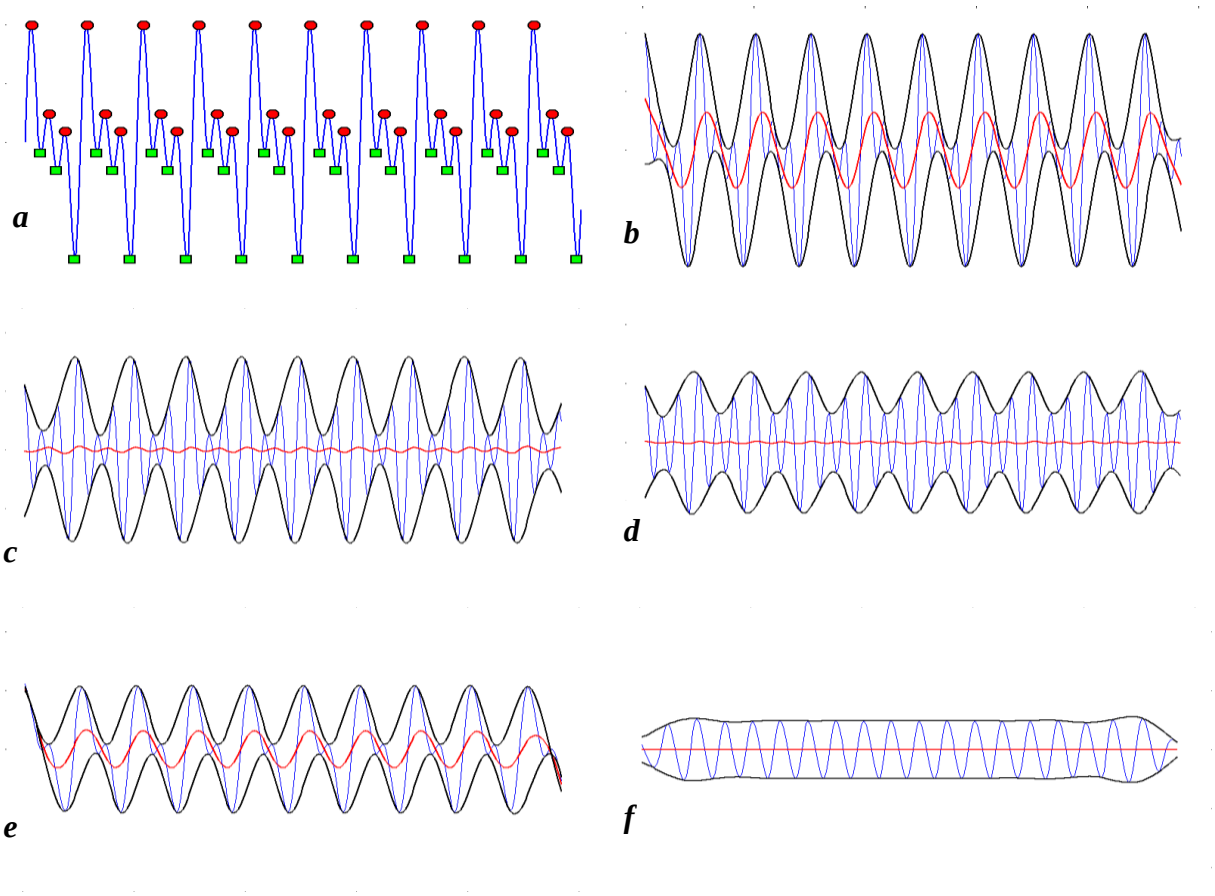

Figure 4.2: *The procedures of extracting IMFs:* ***(a)*** *the blue curve is the input signal* $x(t)$*, red circles represent the local maxima, and the green squares are local minima.* ***(b)*** *Black line is upper and lower envelopes represented by cubic spline interpolation, and the red line is the mean envelope* $m_{11}(t)$*.* ***(c)*** *the blue curve represents the input signal minus the mean envelop* $(h_{11}(t) = x(t) - m_{11}(t))$*, and the black line is the envelopes.* ***(d)*** *The blue signal is the first IMF* $(c_1(t))$ *since it meets the IMF requirements.* ***(e)*** *Blue curve is the input signal minus the first IMF (residual* $r_1(t) = x(t) - c_1(t)$*), to be considered as new input signal.* ***(f)*** *Blue curve is the second IMF* $(c_2(t))$ *together with its upper, lower and mean envelopes.*

4.3.2 Stopping criteria

The most appropriate and common stopping criteria are designed to avoid over iterating. Therefore, common stopping criteria are:

i. To sift until a residual error of a standard deviation between consecutive components is met.

If two components from successive iterations are close enough to each other, it is assumed that the extracted component represents the actual oscillation mode (Huang et al., 1998). The standard deviation between components $\boldsymbol{h_{1(k-1)}}$ and h_{1k} of the first IMF for $\boldsymbol{k}$ number of iterations is given by:

$$\boldsymbol{SD} = \sum_{t=0}^{T} \left[\frac{\left| \boldsymbol{h_{1(k-1)}(t) - h_{1k}(t)} \right|^2}{\boldsymbol{h^2_{1(k-1)}(t)}} \right] \qquad \textbf{(4.3)}$$

$\boldsymbol{SD}$ must be smaller than a predetermined threshold value $\boldsymbol{\varepsilon}$; a typical value for **SD** is between 0.2 and 0.3. The reason for using a threshold ε is to force the envelope mean signal to zero which will guarantee the symmetry of the two envelopes (maxima and minima) and the correct relation between the number of zero crossings and number of extremes that define the IMFs. The predefined limit should be small enough to let the sifting separate all the oscillations but large enough so the sifting does not overwork the signal losing the meaningful components. A smaller threshold ε could lead to over sifting which may inadvertently capture some frequencies from the neighboring modes and lead to the mixing of IMF modes. On the other hand, larger limits might lead to a too early termination and leave some modes not separated (Huang et al., 1998).

However in practice $\boldsymbol{SD}$ is often not a reliable stopping criterion because it does not test or check if the IMFs meet the conditions that guarantee robust IMF extraction.

ii. Limiting the maximum numbers of iteration by a predefined value.

Huang et al. (1998) has suggested to stop the iterations when the number of extrema and the number of zero crossing are the same or differ by one. An iteration number between 4 and 10 is normally found to be enough to comply with this condition.

iii. Limiting the amplitude of sifting results by applying a threshold.

Rilling et al. (2002) have suggested a criterion of separating global changes from local changes by introducing two thresholds $\boldsymbol{\theta_1}$ and $\boldsymbol{\theta_2}$, aimed at guaranteeing globally small fluctuations in the mean while taking into account locally large excursions. This amounts to introducing the mode amplitude $\boldsymbol{m(t) := (e_{upper}(t) - e_{lower}(t))/2,}$ and the evaluation function $\boldsymbol{\sigma(t) := |m(t)/\alpha(t)|}$ so that sifting is iterated until $\boldsymbol{\sigma(t) < \theta_1}$ for some prescribed fraction $\boldsymbol{(1-\alpha)}$ of the total duration, while $\boldsymbol{\sigma(t) < \theta_2}$ for the remaining fraction. One can typically set $\boldsymbol{\alpha \approx 0.05}$, $\boldsymbol{\theta_1 \approx 0.05}$ and $\boldsymbol{\theta_2 \approx 10\theta_1}$.

In my implementation I use a combination of stopping criterion ii and setting a maximum number of allowed iterations.

4.3.3 Continuing sifting

The signal $\boldsymbol{h_{11}}$ output from the first iteration will typically be tested using the stopping criteria. Two possibilities now exist:

I. $\boldsymbol{h_{11}}$ is not an IMF, i.e., the stopping criteria have never been met (cf. Fig. 4.2 c).

In this case, update the input signal $\boldsymbol{h_{10}}$ in step 1 with $\boldsymbol{h_{11}}$, and carry out a second iteration by repeating steps 2 to 4 (Section 4.3.1). The output from step 4 will now be:

$$\boldsymbol{h_{12}(t) = h_{11}(t) - m_{12}(t)} \qquad \textbf{(4.4)}$$

If $\boldsymbol{h_{12}}$ does not meet the IMF conditions, the iteration process is again repeated until the stopping criteria are met after an iteration $\boldsymbol{k}$ (cf. Fig .4.2 d):

$$\boldsymbol{h_{1k} = h_{1(k-1)} - m_{1(k)}} \qquad \textbf{(4.5)}$$

II. The h_{11} is found to meet the stopping criteria so no further iterations are needed. After $h_{11}(t)$ or $h_{1k}(t)$ being confirmed as the first IMF now, let:

$$h_{1k} = c_1(t) \tag{4.6}$$

$c_1(t)$ should contain the finest scale or the shortest period (highest frequency) component of the data. Next, subtract $c_1(t)$ from the original input signal $x(t)$ (cf. Fig. 4.2 e):

$$r_1(t) = x(t) - c_1(t) \quad \underline{or} \quad r_1(t) = h_{10}(t) - c_1(t) \quad \underline{since} \quad h_{10}(t) = x(t) \tag{4.7}$$

$r_1(t)$ is the residue, and is treated now as new input data as long as it is a non-monotonic function, and subject to the same sifting process from step 1 to 4 as described in section 4.3.1. Again, an iterative procedure is carried out until the stopping criteria are met and the second IMF is found (cf. Fig. 4.2 f):

$$r_2(t) = r_1(t) - c_2(t) \tag{4.8}$$

The procedure is repeated for all subsequent r_j's resulting in:

$$r_n(t) = r_{n-1}(t) - c_n(t) \tag{4.9}$$

with c_2 to c_n representing the corresponding IMFs of the data. A flow diagram of the EMD process is given by Fig. 4.3. The EMD is completed when the last residue, ideally, does not contain any extrema points. This means that it is either a constant or a monotonic function. The input signal $x(t)$ can be expressed as the sum of the IMFs and the last residue:

$$x(t) = \sum_{j=1}^{N} c_j(t) + r_N(t) \tag{4.10}$$

where $c_j(t)$ are the oscillatory components and $r_N(t)$ is the residual of $x(t)$, after N IMFs are extracted.

The first IMF captures the fast oscillation modes while the higher IMFs represent the slower oscillation modes. The residual signal reveals the general trend of the time series.

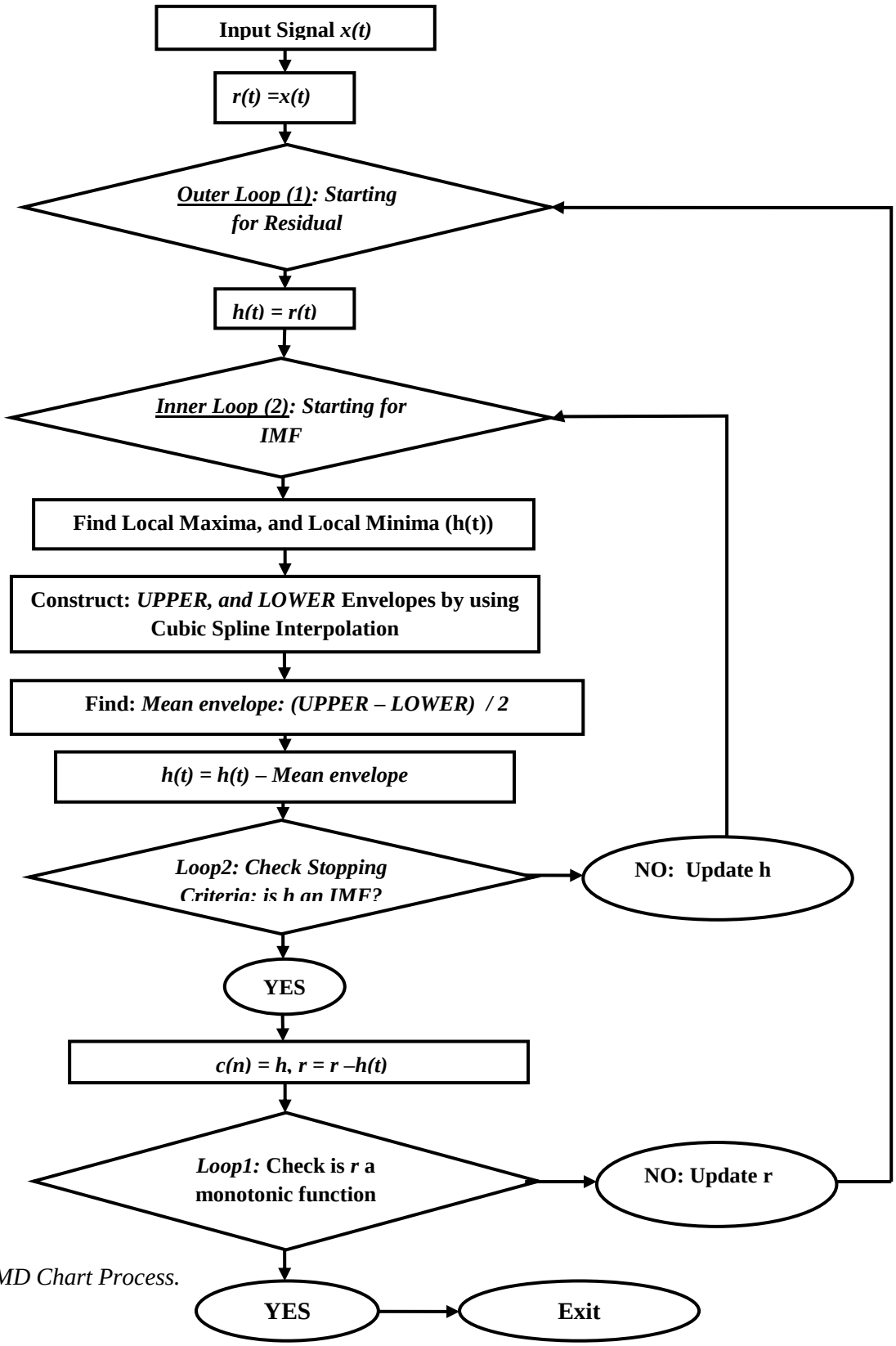

Figure 4.3: *EMD Chart Process.*

4.3.4 Finding the extrema points

A first-derivative can be used to validate any given test point *c* to identify local extrema. For a given function $\boldsymbol{f(x)}$, if its derivative $\boldsymbol{f'(x) > 0}$ in some interval range, then the function $\boldsymbol{f(x)}$ is increasing, on other hand, if its derivative $\boldsymbol{f'(x) < 0}$ in some interval range, then the function $\boldsymbol{f(x)}$ is decreasing.

The local minimum, the local maximum, the turning point and the inflection point of a function $\boldsymbol{f(x)}$ can be defined by using a small positive number ε as follows (cf. Fig. 4.4):

1. If the derivative is negative to the left of the test point $\boldsymbol{f'(c-\varepsilon) < 0}$ and positive to the right $\boldsymbol{f'(c+\varepsilon) > 0}$, then the point *c* is a local minimum.

2. If the derivative is positive to the left of the test point $\boldsymbol{f'(c-\varepsilon) > 0}$ and negative to the right $\boldsymbol{f'(c+\varepsilon) < 0}$, then the point *c* is a local maximum.

3. If $\boldsymbol{f'(c) = 0}$ or $\boldsymbol{f'(c)}$ does not exist at a point *c* then *c* is a turning point of $\boldsymbol{f(x)}$.

4. If both $\boldsymbol{f'(c+\varepsilon)}$ and $\boldsymbol{f'(c-\varepsilon)}$ have same sign, then *c* is an inflection point.

5. In any other case, the test point is neither a minimum nor a maximum.

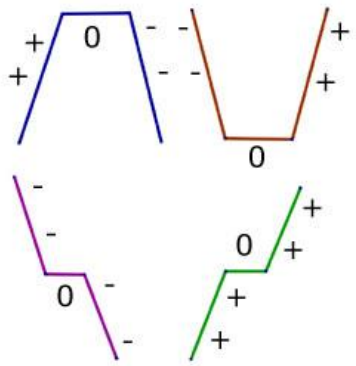

Figure 4.4: *A point of inflection has a zero gradient, but the point does not represent a maximum or a minimum.*

4.4 Problems associated with Empirical Mode decomposition

There are several problems associated with the EMD process. In the following the most important of these will be addressed.

4.4.1 Problem of end effects

In the EMD algorithm, the construction of the upper and lower envelopes is achieved through a cubic spline interpolation of the maxima and minima. Consequently, the mean envelope is also a cubic spline with knots defined by the set of extrema locations. However, if one uses the cubic spline interpolation, overshoots and undershoots are common. Hence, the resulting IMF function does not strictly guarantee symmetric envelopes (Huang et al., 1998).

Such problems occur, when the end points are not extrema causing the spline to swing wildly as shown in Fig 4.5. These effects are not limited to the neighborhood of the end points; they could propagate into the interior of the data especially in the low frequency components. It needs at least one data point at or beyond each end to stabilize the spline. This data point is an extremum, so we have to predict or extrapolate the sequence of extrema for an extra point or two beyond the end.

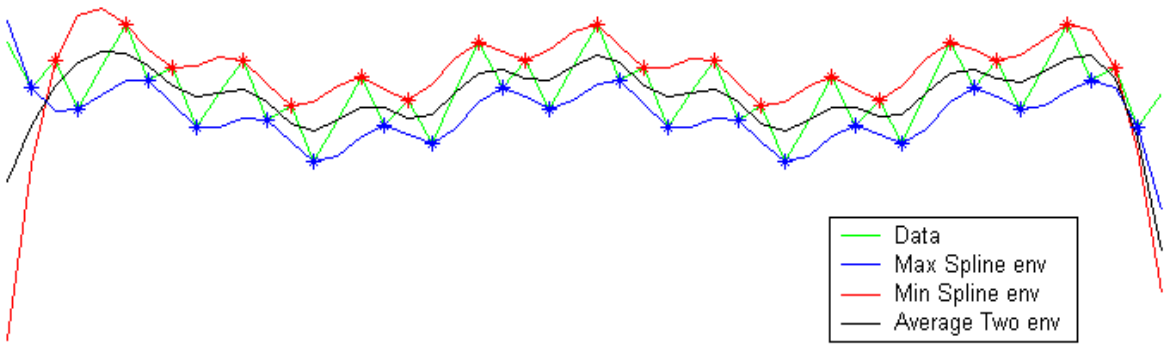

Figure 4.5: *End behavior of cubic spline interpolation.*

Some solutions to solve this problem:

a. The end effects can be treated by adding characteristic waves to the beginning and the end. Since EMD does not necessarily produce orthogonal data, this is not considered a problem since in practice the components are orthogonal at a given time (Huang et. al. 1998 and 2003).

b. The signal can be zero padded to extend it in the beginning and at the end so that the IMFs can truncate at a more controlled level. The same could be achieved by extending the extrema point vector using a linear spline fitting near the boundaries, since ultimately the envelope is calculated from them (Wu and Huang, 2009) (cf. Fig. 4.6). So far this method is considered the best approach to solve end effects (Poularikas, 2010).

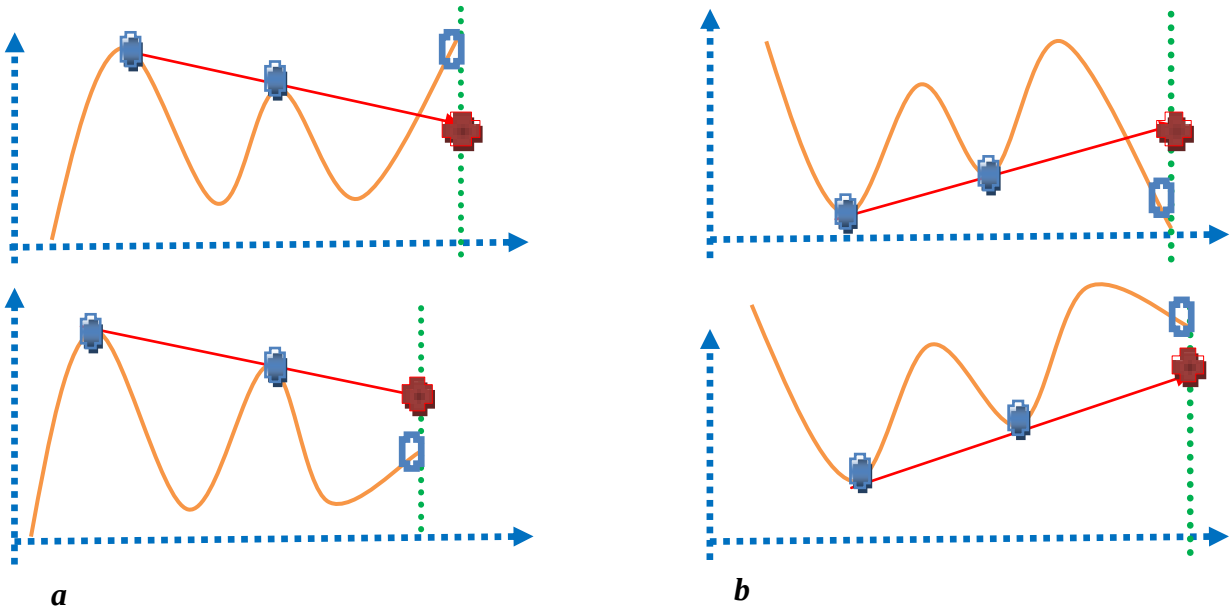

Figure 4.6: *Red point is the determined extrema. The end points are always both maxima and minima with different values.* ***(a)*** *Local maxima.* ***(b)*** *Local minima.*

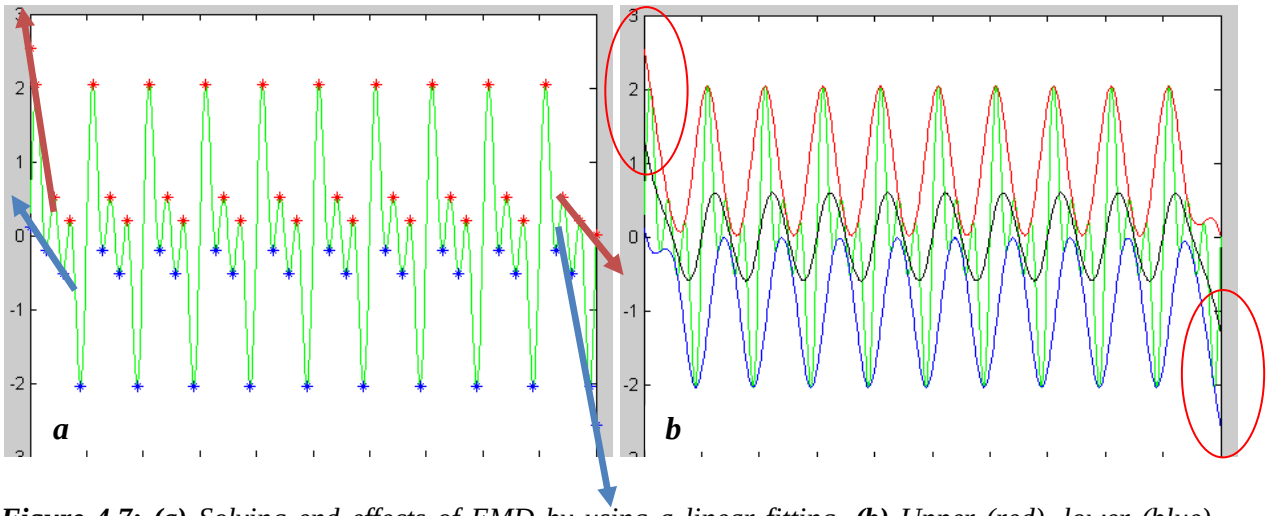

Figure 4.7: (a) *Solving end effects of EMD by using a linear fitting.* ***(b)*** *Upper (red), lower (blue) envelope together with mean envelope (black).*

Fig. 4.7a gives an example where this method creates high artificial extrema at the edges of the data, which again will manifests in the envelopes (cf. Fig. 4.7b).

c. Rilling et al. (2003) has suggested a solution where the extrema take the same value at the two end points. The average of the two envelopes will have the same value as the signal at the end points which leads to all IMFs starting and ending with zero (cf. Fig. 4.8).

d. Dating and Schlurmann (2004) have implemented a signal extension procedure by adding new maxima and minima to the edge of the signal, which leads to new extrema being derived from the original time span of the signal. This ensures that no information being added cancels out and that the original data series remain unaffected.

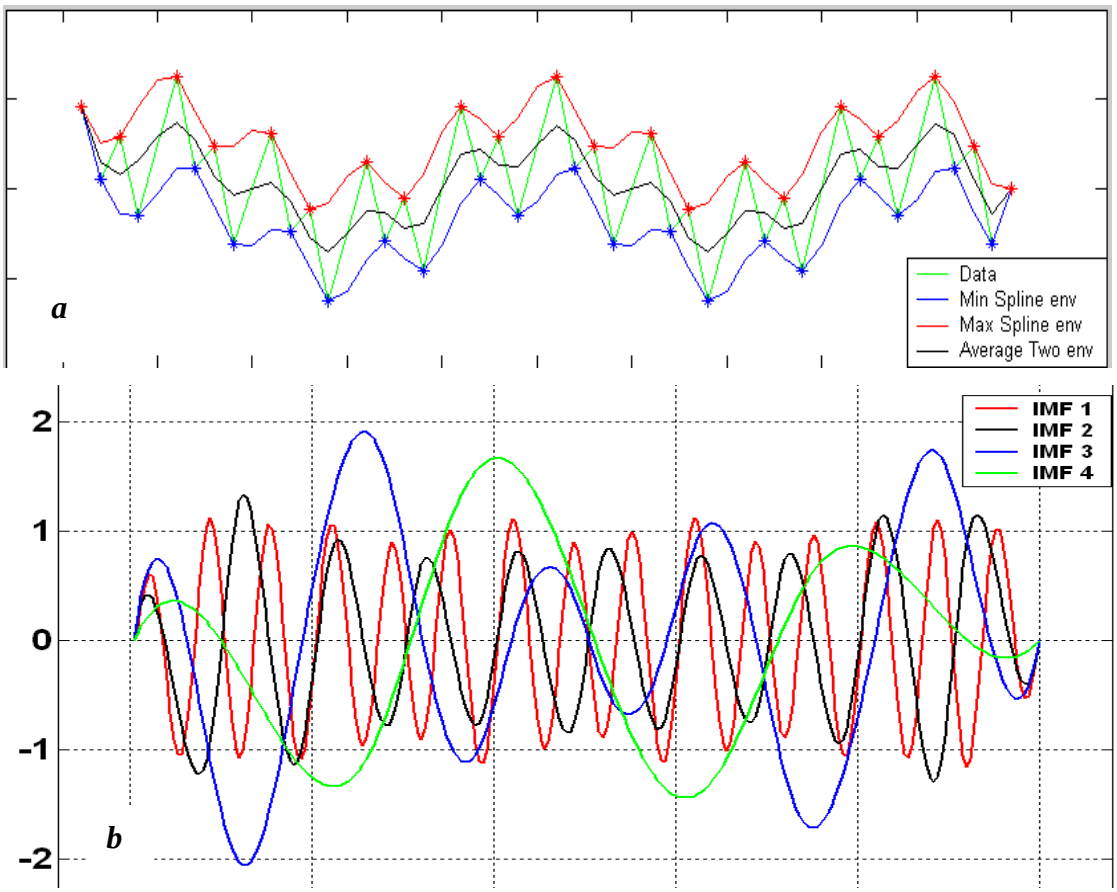

Figure 4.8: *Solving end effects using the method proposed by Rilling et al. (2003):* ***(a)*** *One iteration of extracting an IMF.* ***(b)*** *Resulting IMFs.*

4.4.2 Interpolation problems

There are some concerns with interpolating a set of extrema when using different types of interpolating functions. To overcome the problem of overshooting of the envelopes, a new method has been proposed by Xu et al. (2006) that uses finite element basis functions to construct the local mean surface of the data instead of constructing it from the upper and lower envelopes. Damerval et al. (2005) used Delaunay triangulation of the extrema, and then performed piecewise cubic interpolation on triangles to build extrema envelopes. Linderhed (2004 and 2005) discussed some advantages of using Cubic Splines over Piecewise Cubic Hermite Interpolation and investigated the issues of proper spline interpolation by using thin-plate smoothing splines and triangle-based cubic interpolation to generate upper and lower

envelopes. For sparse data, thin-plate splines were smoother than triangle-based cubic interpolation.

4.4.2.1 Piecewise Cubic Hermite Interpolation

One of the most effective interpolation methods is based on piecewise cubic polynomials (Lancaster and Salkauskas, 1986).

The polynomial output from this interpolation method, denoted $\boldsymbol{P}(\boldsymbol{x})$, is fully defined by its values, and its first derivatives at a given set of points.

The function that satisfies the interpolation conditions on the derivatives are defined as Hermite C^1 interpolants; which are characterized by having continuous first derivatives.

If the derivative values are not given explicitly, then approximations to their values can be constructed; a particularly useful property is that in the case of monotonic or piecewise monotonic data this may be done in such a way that the resulting interpolation preserves monotonicity in the data. As a result, the interpolant does not exhibit unwanted oscillations, and is often considered more 'visually pleasing' than other types of interpolators such as cubic splines (De Boor, 2001).

4.4.2.2 Cubic Splines Interpolation

The first derivative $\boldsymbol{P}'(\boldsymbol{x})$, of the piecewise cubic function is defined by different formulas on either side of a knot (a breaking point) $\boldsymbol{x_k}$. Both formulas yield the same value $\boldsymbol{d_k}$ at the knots, so $\boldsymbol{P}'(\boldsymbol{x})$ is continuous. On the $\boldsymbol{k}$**th** subinterval, the second derivative $\boldsymbol{P}''(\boldsymbol{x})$ must be continuous and this makes the difference between cubic spline and cubic Hermite. Cubic spline has several alternatives based on the boundary conditions:

- Natural Spline:

$$\boldsymbol{P}''(\boldsymbol{x_1}) = \boldsymbol{0} \;\; \boldsymbol{and}\; \boldsymbol{P}''(\boldsymbol{x_m}) = \boldsymbol{0} \qquad \textbf{(4.11)}$$

- Not-a-knot used if the derivatives of the end points are unknown. The third derivatives match at x_1 and x_2 which leads to:

$$\boldsymbol{P_1'''(x_2) = P_2'''(x_2)} \textbf{ and } \boldsymbol{P_{n-2}'''(x_{n-2}) = P_2'''(x_2)} \qquad \textbf{(4.12)}$$

By considering a continuous second derivative, this kind of spline makes the interpolating function look "nice and smooth" as it crosses over each knot. What is different about the not-a-knot conditions are that they are forcing the third derivative to also be continuous at both the second knot, and at the penultimate knot in the spline. Essentially, by forcing the third derivative to also be continuous at these particular knots it is as if those points are no longer knots at all. Single cubic segments extend from the first to the third knots, and likewise at the right hand end point, this explains the name "not-a-knot" **(**De Boor, 2001).

Matlab (which I shall be using in one implementation of the algorithm) uses not-a-knot spline, because not-a-knot end conditions form a very good compromise, i.e. well fitting for large sets of data types and performing better than the natural end conditions does.

Fig. 4.9 shows the effects of using linear interpolation, cubic Hermite interpolation, and cubic spline interpolation (not-a-knot) on regularly sampled data. The interpolation method clearly plays an important role in the sifting process determining the frequency resolution that can be achieved. However, in this case the difference between Hermitian and cubic splines interpolation are quite marginal. The cubic Hermitian interpolation is a local interpolation method in the sense that the corresponding piecewise polynomials depend only on the two nearest nodes. This implies that this interpolation method is easier to handle mathematically than natural cubic splines. One problem associated with piecewise cubic spline interpolation is that the interpolation is introducing new extrema points that are not necessarily true.

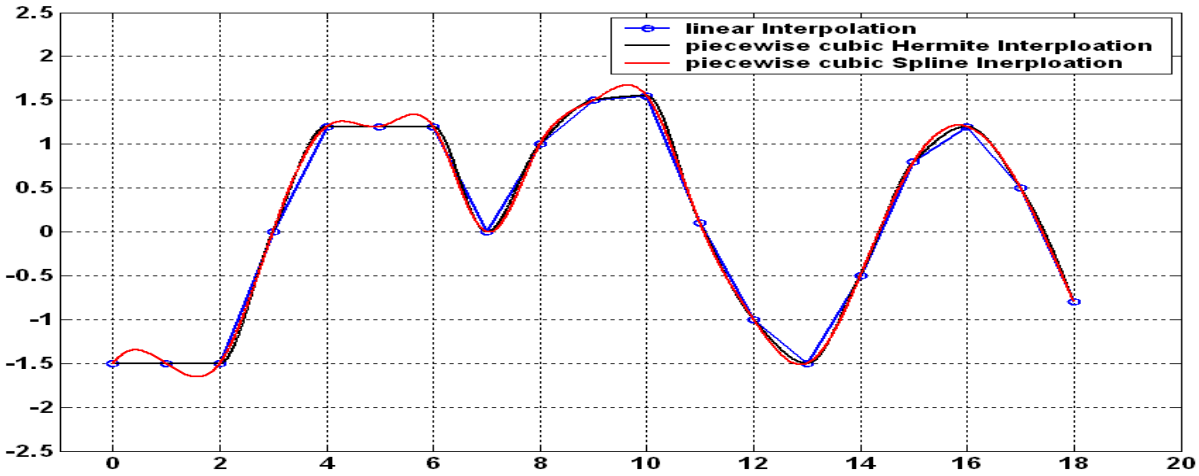

Figure 4.9: *Linear, piecewise cubic Hermite and piecewise cubic Spline Interpolation of regularly sampled data.*

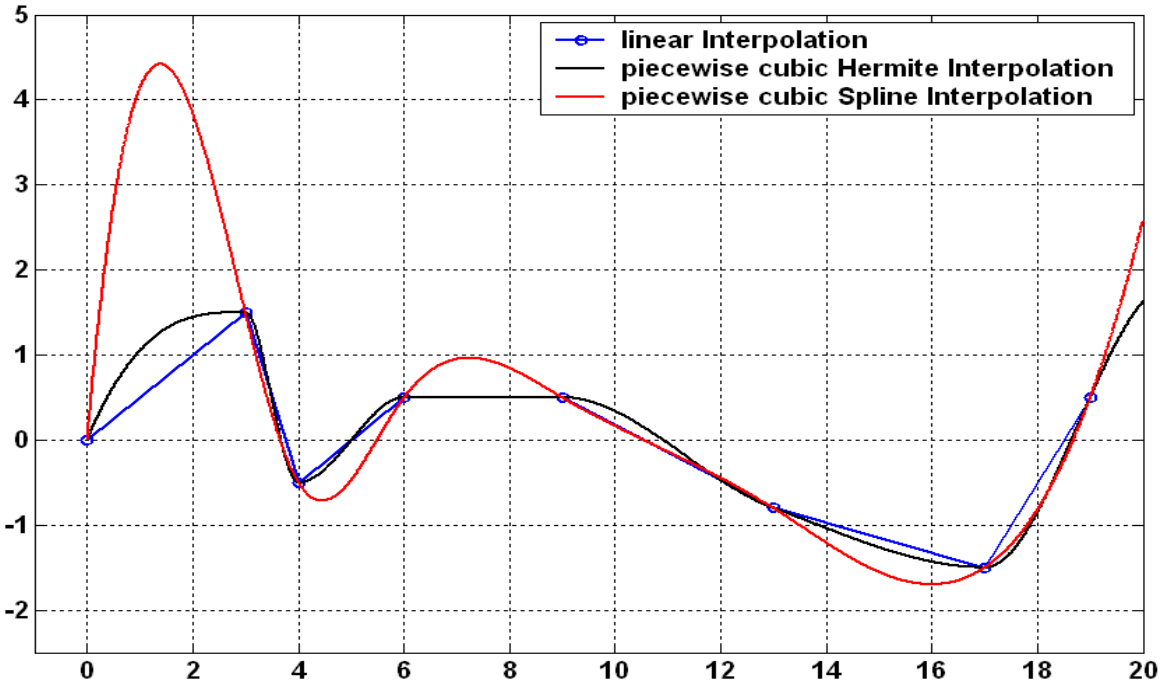

Figure 4.10: *Interpolation methods applied to sparse data.*

Figure 4.10 shows the same interpolation methods applied to irregularly spaced and sparse data. Clearly, piecewise cubic spline interpolation has introduced artificial local extrema to the data. Only linear interpolation and piecewise cubic Hermite interpolation has kept the

original extrema in the data. Consider now a signal with zero values in its middle part (between $\mathbf{0.5 < t \leq 1}$) and which is non-stationary (cf. Fig. 4.11a):

$$x(t) = \begin{cases} \sin(2 * 5\pi t) + \sin(2 * 10\pi t) + \sin(2 * 20\pi t) & 0 < t \leq 0.5 \\ 0 & 0.5 < t \leq 1 \\ \sin(2 * 5\pi t) + \sin(2 * 20\pi t) + \sin(2 * 40\pi t) & 1 < t \leq 1.5 \end{cases}$$

The performance of the cubic spline interpolation and the Hermite interpolation can now be compared (cf. Figs. 4.11 b and c). The cubic spline has been able to extract the exact frequency for each IMF, but introduces some artificial oscillations in the zero data zones. In the Hermite case, the first three IMFs could not capture the correct frequencies compared to the spline case, but no artificial oscillations were introduced in the zero data zone compared to the cubic spline interpolation. Using cubic Hermite interpolation gives slower convergence of the sifting process and a higher number of IMFs can be found for the same value of the stopping criteria. Rilling et al. (2003) suggested that cubic spline was to be preferred to linear or polynomial interpolation based on some unreported experiments. In this thesis I will employ the not-a-knot cubic spline interpolation.

4.4.3 Problem of mixing modes and the Ensemble Empirical Mode Decomposition

Mode missing occurs when two or more different modes of oscillation appear in a single IMF. The highest frequency and lowest frequency components of the signal clearly belong to different modes of oscillation but in mode mixing they are spread over all extracted IMFs. Mode mixing not only causes serious aliasing in any subsequent IMFs, but can cause individual IMFs to be devoid of physical meaning (Wu and Huang, 2004). To remedy this, Huang et al. (2009) introduced the Ensemble Empirical Mode Decomposition (EEMD), in which an ensemble mean is taken over a number of IMFs extracted from multiple applications of EMD to the original signal each time with a different white noise addition (cf. Fig. 4.12). It was shown in Flandrin et al. (2003) that EMD acts as an adaptive dyadic filter bank (see Section 4.6) when decomposing pure Gaussian noise and therefore the principle of EEMD is relatively straightforward.

The added white noise will occupy the entire time frequency space and the different parts of the signal will automatically be projected onto proper scales of reference established by the white noise, thus eliminating mode mixing.

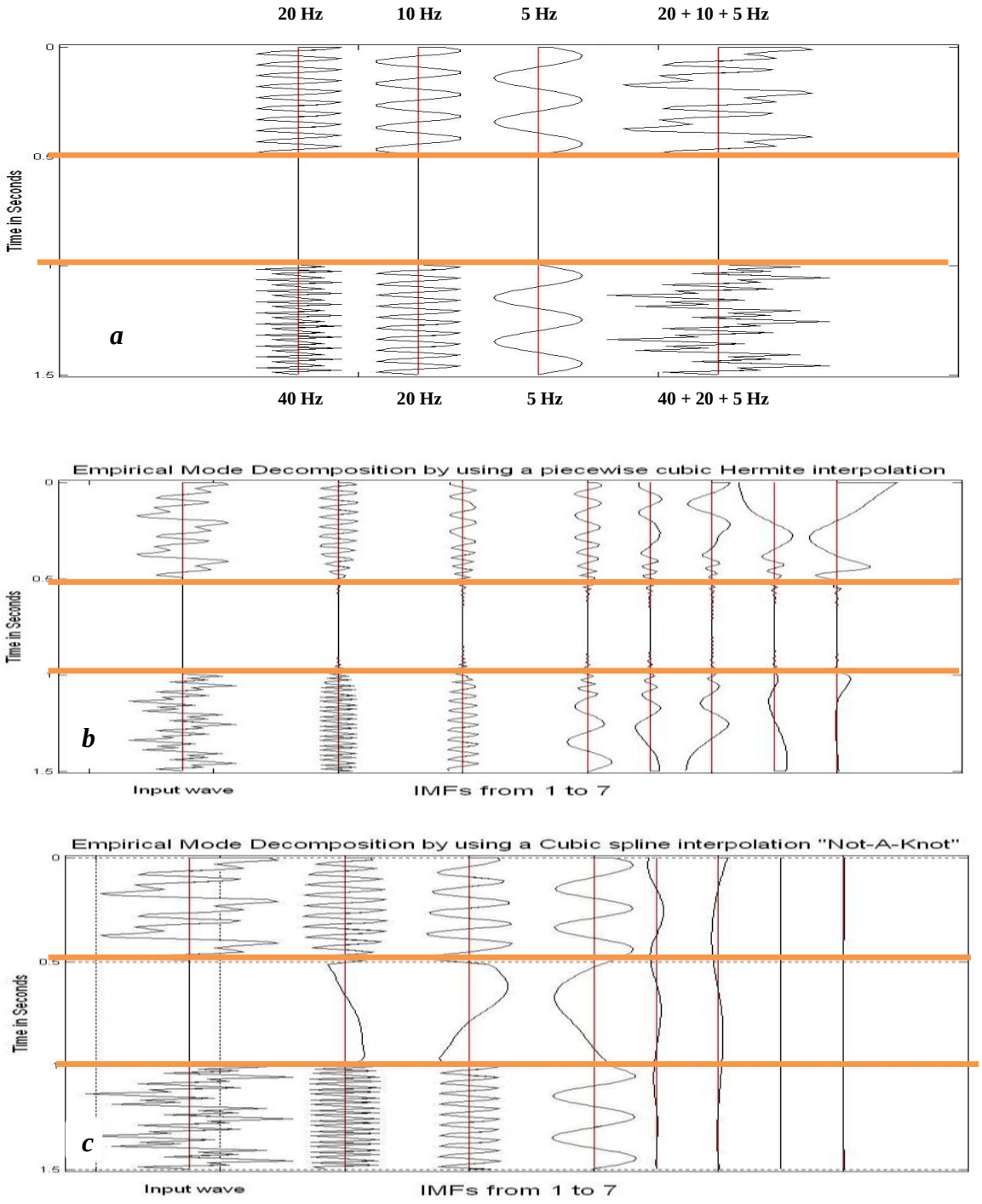

Figure 4.11: *EMD by using different interpolation methods:* ***(a)*** *Input signal.* ***(b)*** *The IMFs resulted from using a piecewise cubic Hermite Interpolation.* ***(c)*** *The IMFs resulted from using a piecewise cubic spline Interpolation.*

The individual IMFs are, of course, very noisy but the ensemble mean of a number of corresponding IMFs will leave only the signal, as a collection of white noise cancels each other out in a time space ensemble mean (Wu and Huang, 2004). However, adding more noise to already contaminated signals will not produce cleaner results. The realization of the original contaminated noise remains the same over all trials and therefore cannot be eliminated through averaging. For this reason, in my EEMD implementation I used noise with standard deviation of 30%.

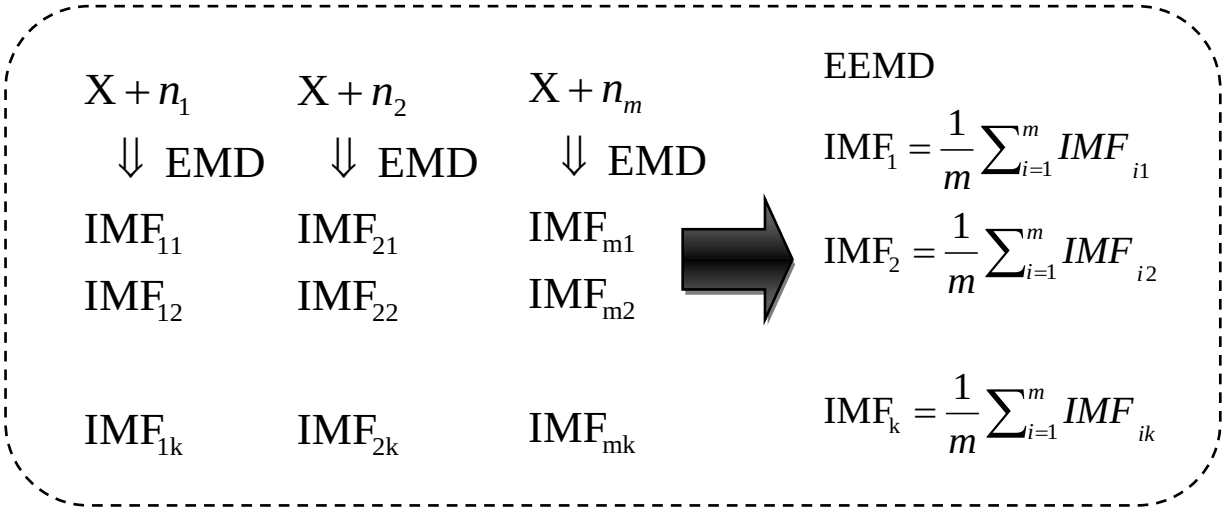

Figure 4.12: *Flow of EEMD.*

As the number of ensemble members, ***N***, increases, the effect of the noise decreases as governed by the well established rule:

$$\boldsymbol{\varepsilon_n = \frac{\varepsilon}{\sqrt{N}}} \qquad \textbf{(4.13)}$$

where ε is the amplitude of the added noise and ε_n is the standard deviation of the original data and the summation of the IMFs. Figure 4.13 gives an example of mode mixing employing a data set consisting of a low frequency wave and two high frequency bursts. Fig. 4.13 Left: (b)-(e) depicts the IMFs extracted from data which have no guarantee of being globally orthogonal, although have been shown to be locally orthogonal (Huang et al., 1998, and Rilling et al., 2003).

Fig. 4.13 Right: (f)-(h) shows the IMF results obtained by applying the EEMD method to the same signal. In the EEMD computation random noise with a standard deviation of 25% and 30 iterations are used as the parameter setting. The two high-frequency components now appear in a single IMF opposite to the EMD result. This example is similar to a single-channel seismic reflection containing strong low frequency cable strum noise as discussed in Chapter 6.

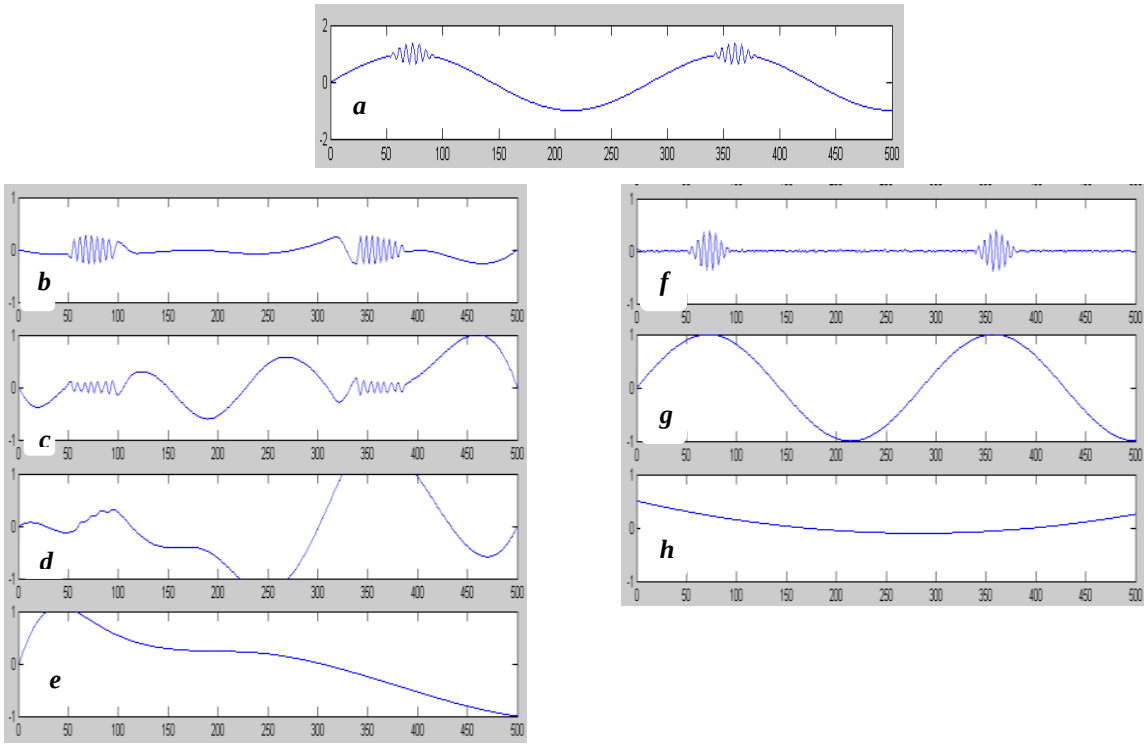

Left ***Right***

Figure 4.13: (a) *Input signal.* ***Left:*** *the IMFs by using EMD:* ***(b)*** *IMF 1.* ***(c)*** *IMF 2.* ***(d)*** *IMF 3.* ***(e)*** *IMF 4.* ***Right:*** *IMFs by using EEMD:* ***(f)*** *IMF 1.* ***(g)*** *IMF 2.* ***(h)*** *IMF 3.*

4.5 Test examples of EMD

This section will demonstrate basic features of EMD starting with simple stationary signals and moving to more complicated cases involving non-stationarity (Huang et al., 2009 and Linderhed, 2004).

4.5.1 Stationary signals

In the first example assume that the input signal *x(t)* is stationary containing three frequencies 10 , 20, and 40 Hz respectively , and with corresponding amplitudes of 1, 1.5, and 2:

$$x(t) = \sin(2*10\pi t) + 1.5*\sin(2*20\pi t) + 2*\sin(2*40\pi t)$$

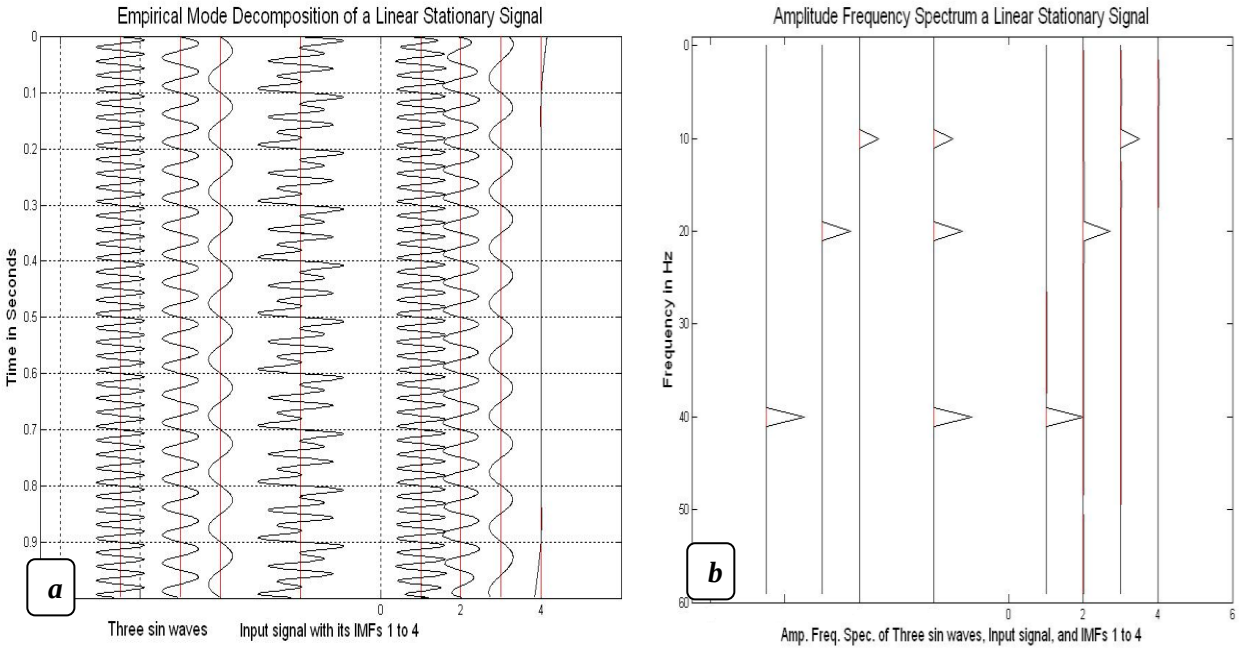

Figure 4.14: (a) *EMD of a stationary signal containing frequencies 10, 20, 40 Hz, together with its first four IMFs.* ***(b)*** *The amplitude spectrum of the different contributions in the left figure.*

Fig. 4.14 shows how the first IMF captures the highest frequency of the signal (40 Hz), the second IMF the second highest frequency (20 Hz), and the third IMF the lowest frequency (10 Hz). In this example all three frequencies were well separated apart and the EMD works well with few iterations. In the next example a signal consisting of three closer frequencies (10, 12 and 15Hz) is considered:

$$x(t) = \sin(2*10\pi t) + 1.5*\sin(2*12\pi t) + 2*\sin(2*15\pi t)$$

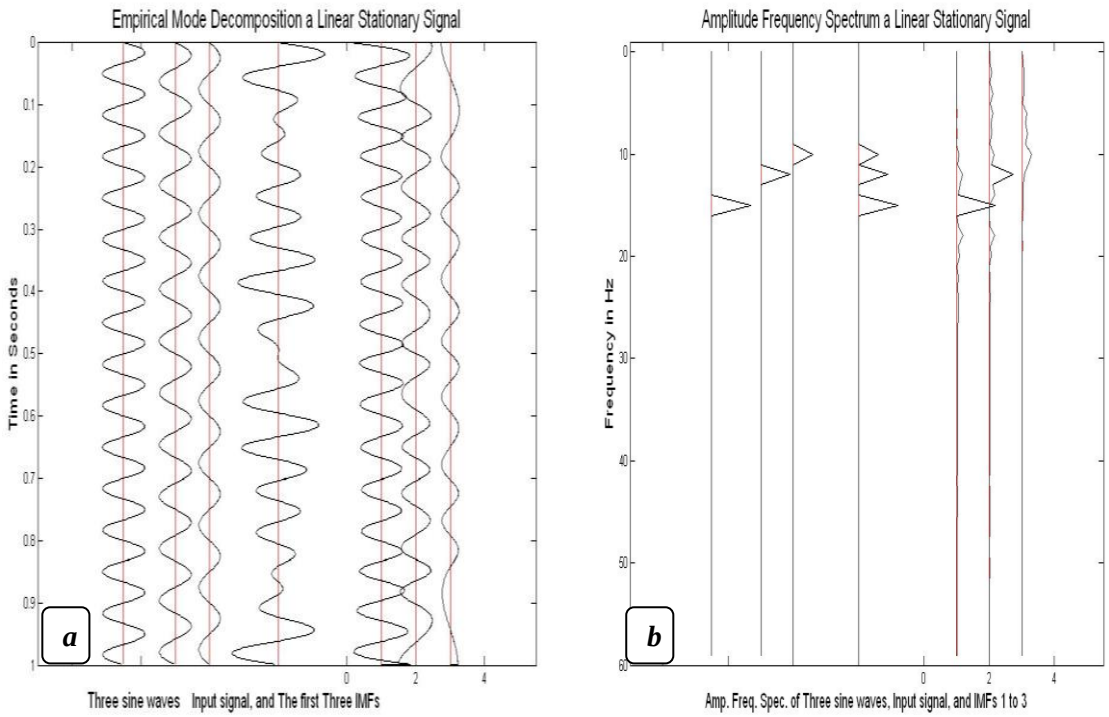

Figure 4.15: (a) *EMD of a stationary signal consisting of frequencies 10, 12 and 15 Hz, together with its first four IMFs.* ***(b)*** *The amplitude spectrum of each signal from the left panel.*

In this case, EMD needs more iterations (i.e. 60) for IMF 1 to capture the highest frequency of the signal compared to 8 iterations in the previous example. This example illustrates that the IMF modes start to mix frequencies since they are now closer in value (cf. Fig. 4.15). The EMD needs over-sampled data so that instantaneous frequencies can be determined. This example illustrates a real problem that frequencies too close to each other cannot be separated quite well. Also, the correspondence between IMFs and physical components is not guaranteed (Huang et al., 1998 and 2003).

4.5.2 Non-stationary signals

Consider now the following non-stationary signal ***x(t)***:

$$x(t) = \begin{cases} sin(2 * 20\pi t) + sin(2 * 40\pi t) + sin(2 * 80\pi t), & 0 < t \leq 0.25 \\ sin(2 * 20\pi t) + sin(2 * 80\pi t), & 0.25 < t \leq 0.50 \\ sin(2 * 20\pi t) + sin(2 * 80\pi t) + sin(2 * 160\pi t), & 0.5 < t \leq 0.75 \end{cases}$$

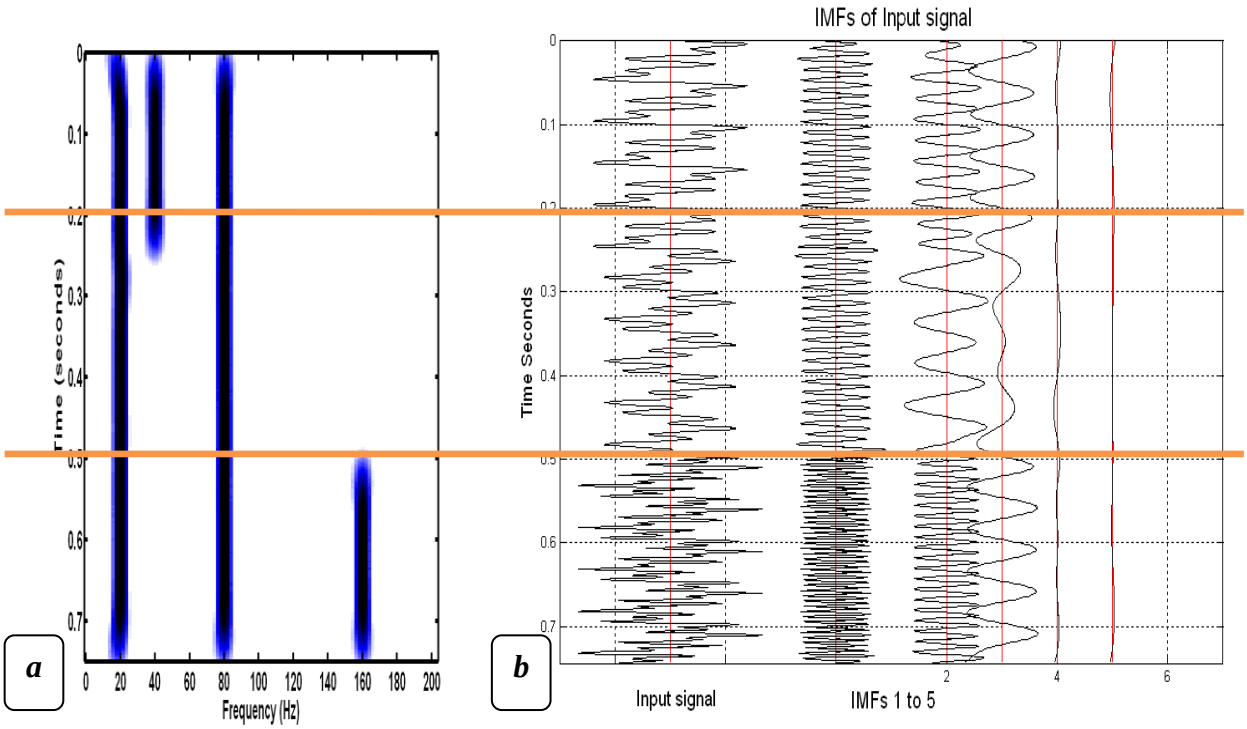

Figure 4.16: (a) *STFT amplitude spectrum of the input signal.* ***(b)*** *IMFs of the non-stationary signal.*

The frequency content of the signal is now changing with time (cf. Fig. 4.16). The highest frequency of the first two third of the signal is 80 Hz, while the last third of the signal has the highest frequency of 160 Hz. As shown in Fig 4.16a, the short time Fourier transform (STFT) gives a clear idea of how the signal frequencies change with time. Ideally, the first IMF should then capture the following signal:

$$\boldsymbol{IMF\ 1} = \begin{cases} \boldsymbol{sin(2 * 80\pi t),} & \boldsymbol{0 < t \leq 0.50} \\ \boldsymbol{sin(2 * 160\pi t),} & \boldsymbol{0.50 < t \leq 0.75} \end{cases}$$

It follows from Fig.4.16b that the first IMF has been able to capture the highest frequency in each part of the signal. Fig. 4.17 shows the 9 iterations needed to extract the first IMF of the signal (see also its amplitude spectrum in Fig. 4.18). However, there are some distortions present around the times where frequencies suddenly change.

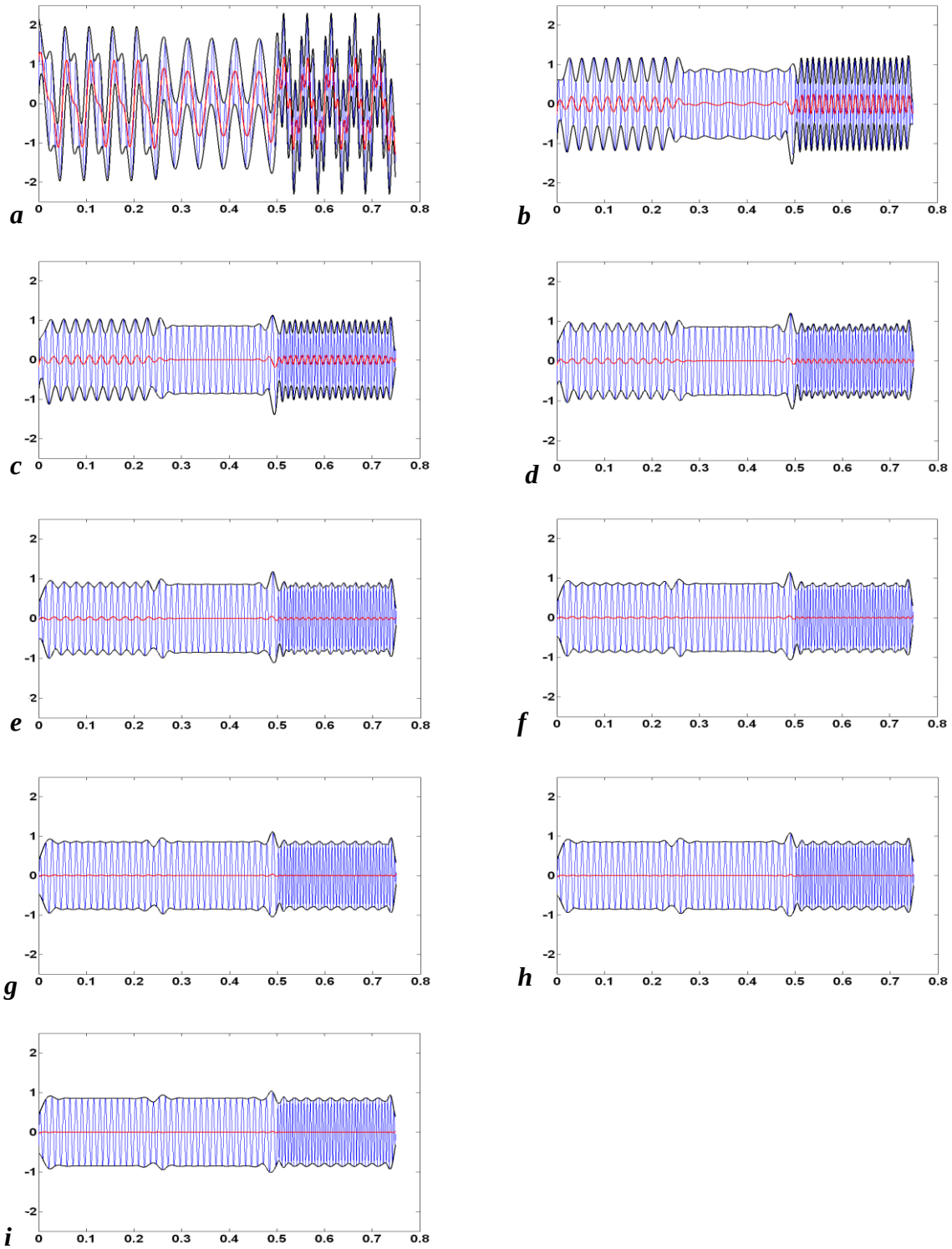

Figure 4.17: (a to i) *extracting the first IMF by using 9 iterations.*

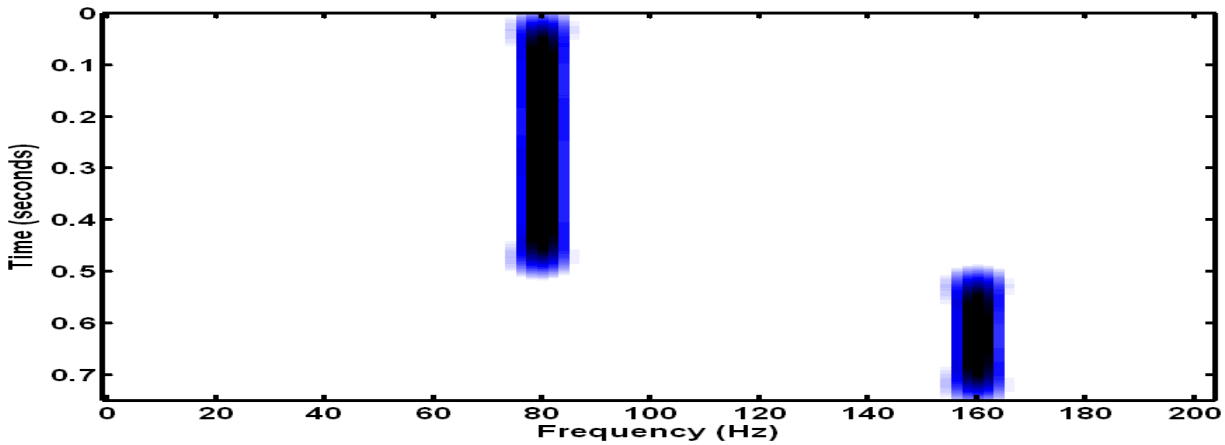

Fig. 4.18: *STFT amplitude spectrum of the first IMF.*

Ideally, the second IMF should represent the following sub-signal (cf. Fig. 4.19):

$$IMF\ 2 = \begin{cases} sin(2 * 40\pi t), & 0 < t \leq 0.25 \\ sin(2 * 20\pi t), & 0.25 < t \leq 0.50 \\ sin(2 * 80\pi t), & 0.50 < t \leq 0.75 \end{cases}$$

We see in Fig.4.16b that the second IMF has captured the middle frequencies of each part of the input signal. Again distortions are observed where frequencies change. Figure 4.20 shows the corresponding iterations of the second IMF.

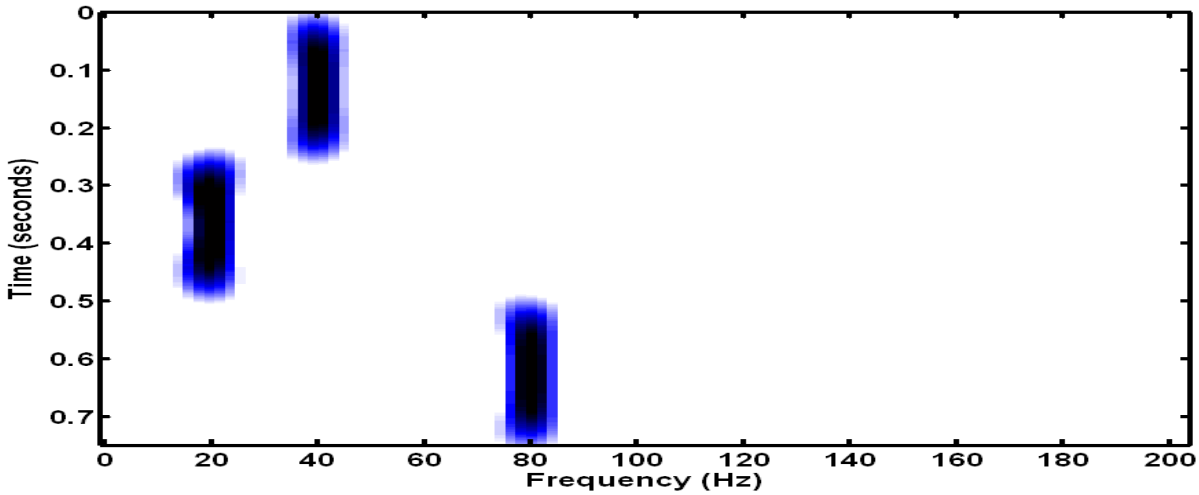

Figure 4.19: *STFT amplitude spectrum of the second IMF.*

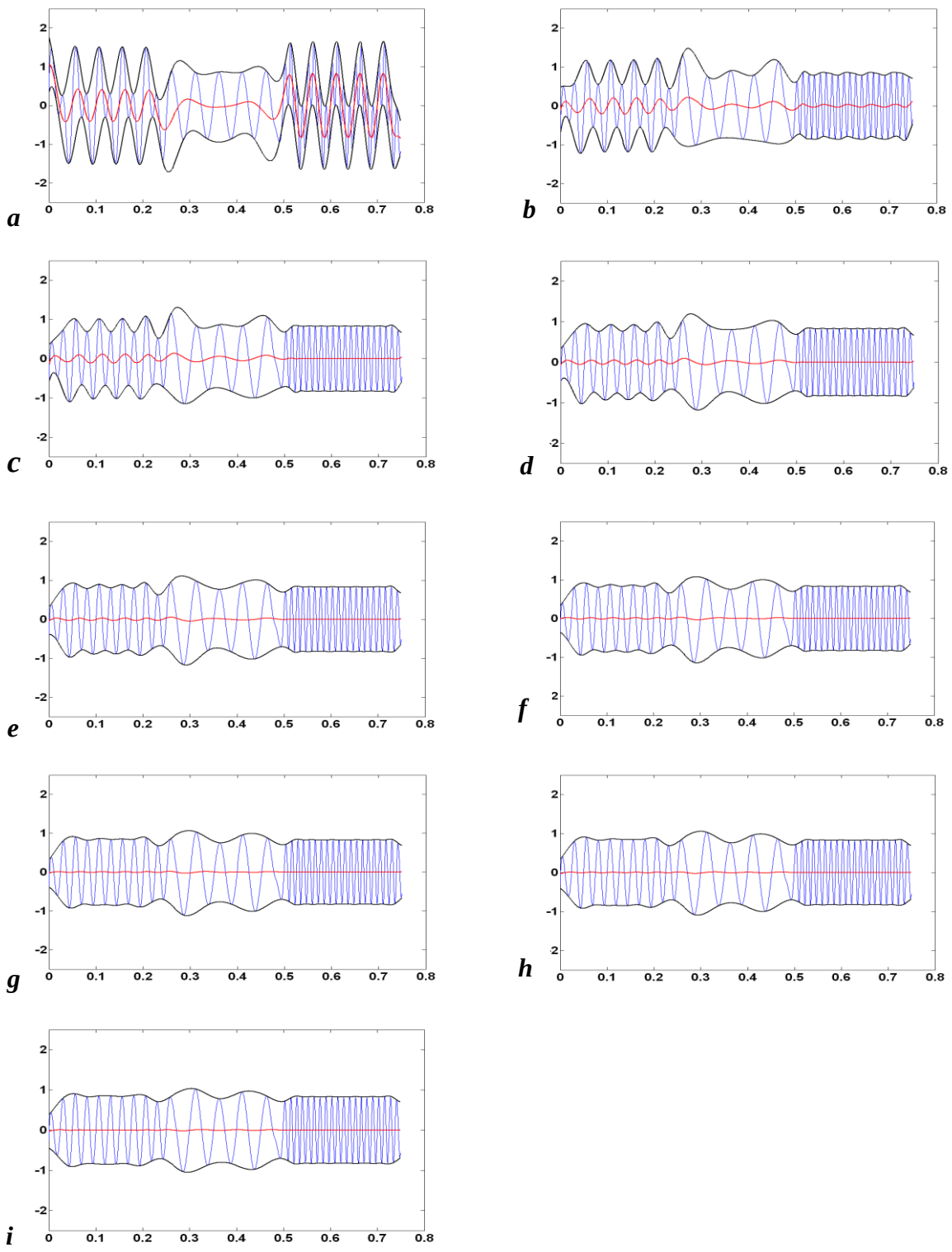

Figure 4.20: ***(a to i)*** extraction of the second IMF after 9 iterations.

Finally the third IMF component should ideally capture the lowest frequencies in the input signal (cf. Fig. 4.21) and Fig. 4.22 shows the three iterations needed for IMF 3:

$$IMF\ 3 = \begin{cases} sin(2 * 20\pi t), & 0 < t \leq 0.25 \\ 0, & 0.25 < t \leq 0.50 \\ sin(2 * 20\pi t), & 0.50 < t \leq 0.75 \end{cases}$$

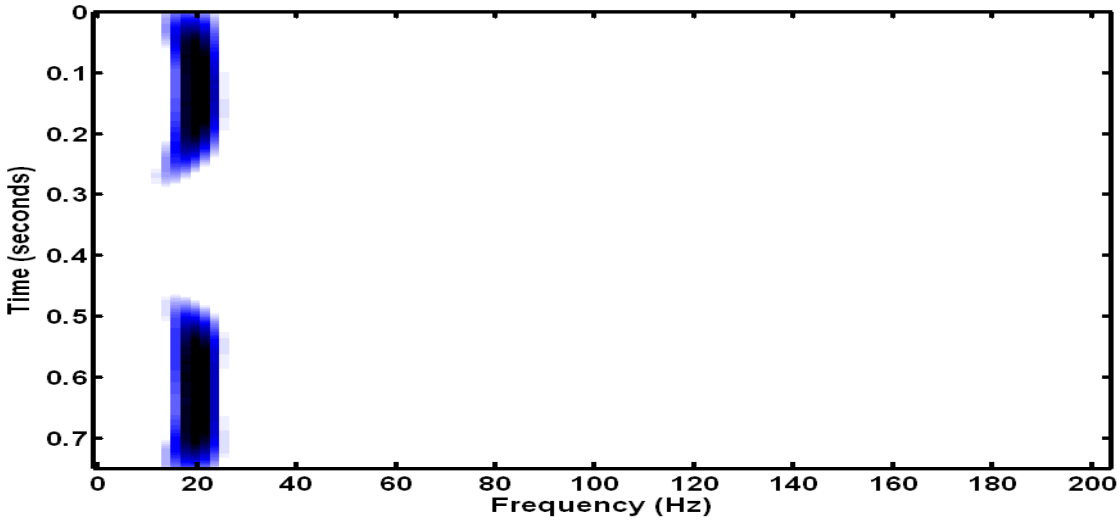

Figure 4.21: *STFT amplitude spectrum of the third IMF.*

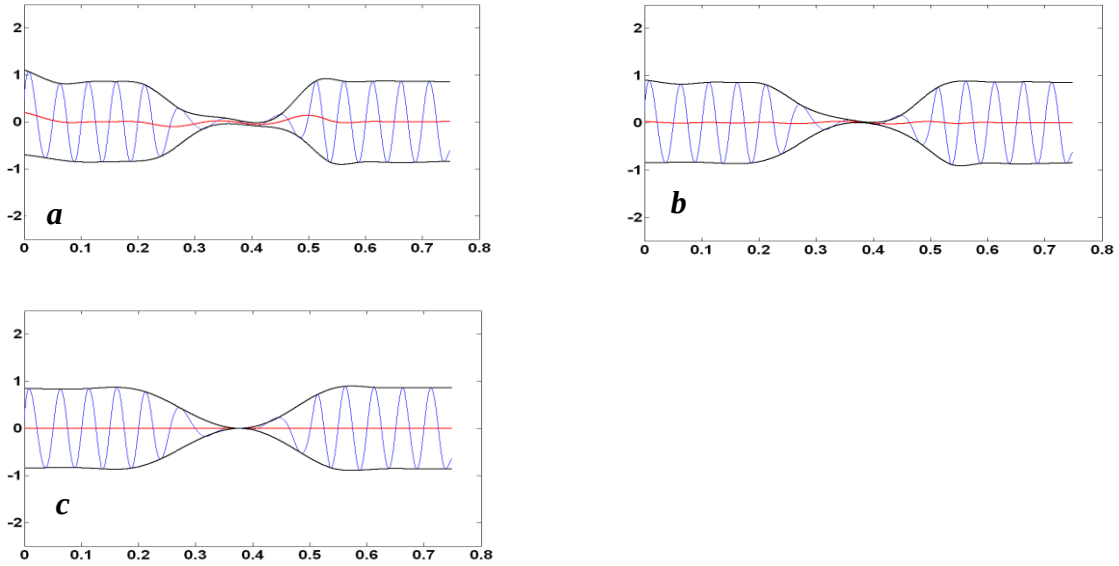

Figure 4.22: (a to c) *extraction of the third IMF after 3 iterations.*

This is also the case as can be seen from Fig 4.16b (again with distortion introduced at each frequency stepping). Fig. 4.23 shows the remaining part of the signal after extracting the first three IMFs.

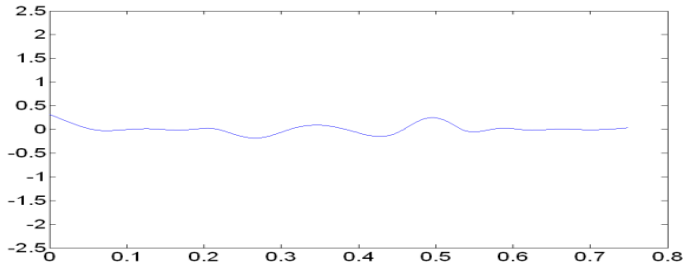

Figure 4.23: *The residual after extracting the first three IMFs.*

4.5.3 Non-stationary sweep signal

Consider a non-stationary signal constructed as the sum of a sweep and linear trend where the frequency is changing linearly with time as shown by its amplitude spectrum (cf. Fig. 4.24). The short time Fourier transform highlights both the trend as a DC component, and the sweep.

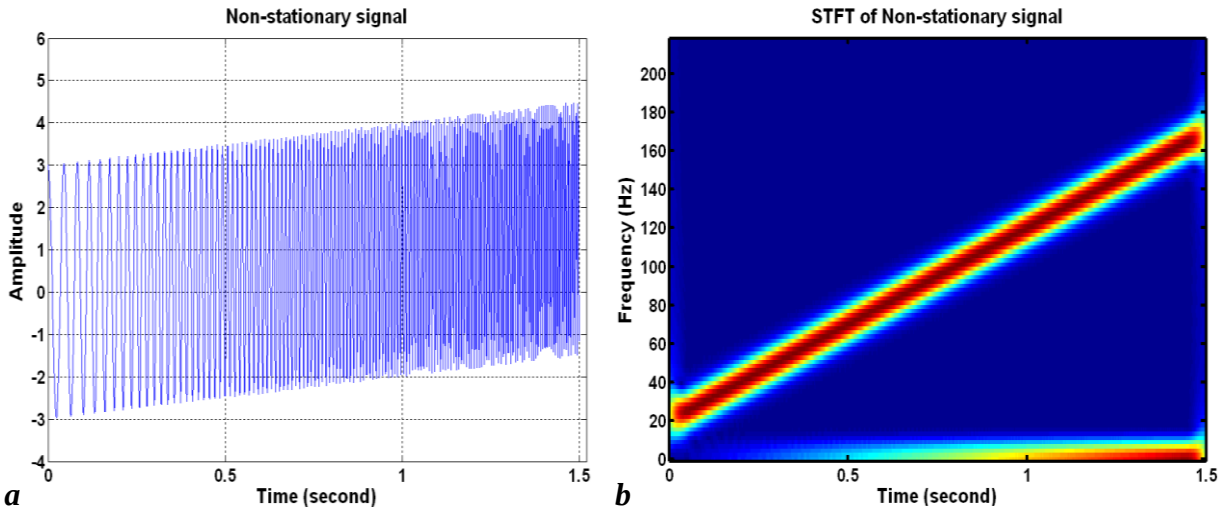

Figure 4.24: (a) *Non-stationary signal constructed as the sum of a sweep and linear trend.* ***(b)*** *Amplitude spectrum (STFT) of the signal.*

The first IMF output from EMD is essentially the same as the sweep signal since it is continuously frequency modulated, and therefore, EMD cannot decompose it into separate IMFs (cf. Fig. 4.25a). The second IMF represents the linear trend added to the sweep signal (cf. Fig. 4.25b). This example of a synthetic signal application demonstrates the potential of EMD for extracting the trend of a signal. I shall return to this in Chapter 8.

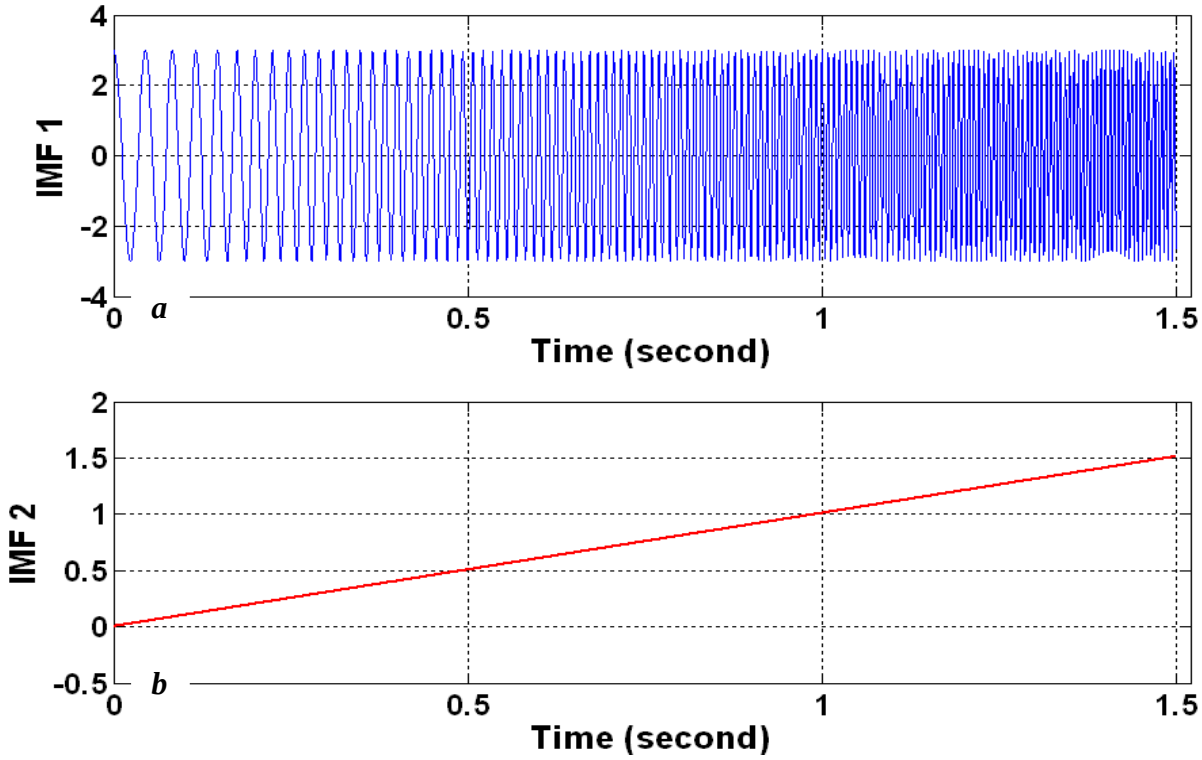

Figure 4.25: *EMD results of the sweep signal.* ***(a)*** *IMF 1 is a sweep signal.* ***(b)*** *IMF 2 is a linear trend.*

4.6 EMD of Gaussian white noise

In digital signal processing a low pass filter can be used to attenuate the high frequencies in the signal. Flandrin et al. (2004) have described the characteristics of EMD in case of a stochastic signal defined by broadband noise as a dyadic filter bank and similar to wavelet decomposition.

Fig. 4.26 shows an example of EMD applied to Gaussian white noise. It is clear that the first IMF has captured the highest frequencies and the last IMF has captured the lowest frequency of the signal. Treating these IMFs as a dyadic filter bank, one notices that the first IMF reflects the filtering characteristic of a high-pass filter, while the middle IMFs act similar to a band-pass filter, where as the last IMF has low-pass filter characteristics. It is interesting to notice that the center frequency of the first IMF is almost double that of the second IMF, and furthermore, the cutoff frequencies of these filters are decreased based on the power of two, and therefore the EMD can be treated as a dyadic filter bank.

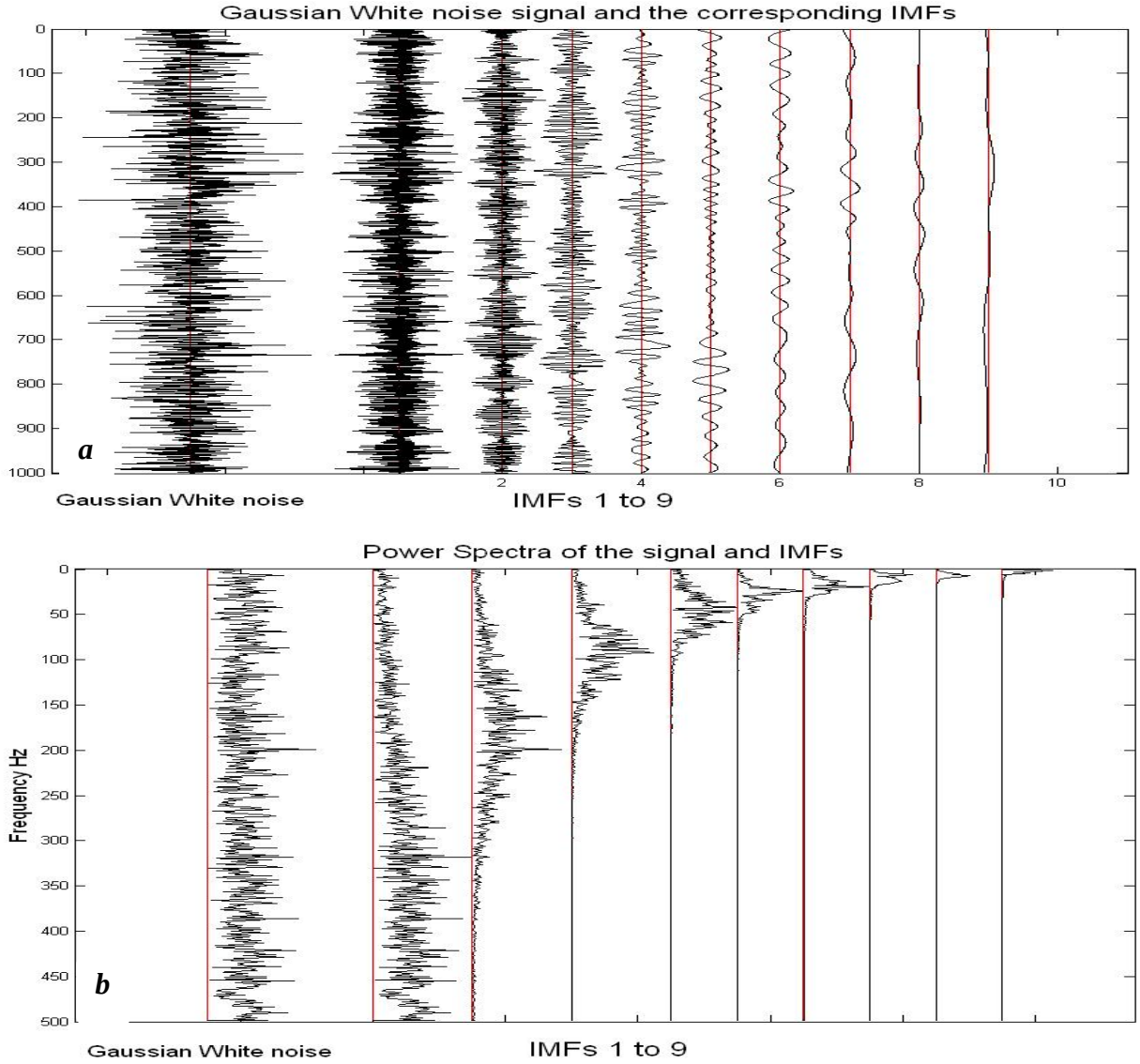

Figure 4.26: *EMD of Gaussian white noise* ***(a)*** *Gaussian white noise with EMD results.* ***(b)*** *Amplitude spectra of the Gaussian white noise, and its IMFs.*

4.7 Improving IMFs by using EEMD

Removing a certain IMF from the signal corresponds to passing the signal through a filter. Since the first IMFs capture the highest frequencies in the signal, removing them can be considered as passing the signal through a low-pass filter, where only the high frequencies are attenuated. The most critical point is to decide which IMFs to be keep, and which IMFs to remove from the signal. It is clear from the Gaussian noise example in the previous section that the white noise appears in all IMFs, and that it is hard to remove it by removing just one specific IMF.

Consider a signal consisting of three sine waves:

$$x(t) = \sin(2*10\pi t) + 1.5* \sin(2*20\pi t) + 2* \sin(2*40\pi t)$$

Gaussian noise is now added to this signal, and EMD applied to it. The calculated IMFs are shown in Fig. 4.27a and it is clear that the first two IMFs capture most of the Gaussian noise while following three IMFs (i.e. 3, 4 and 5) capture most of the 40, 20, and 10 Hz sine waves in order with smaller amounts of Gaussian noise (cf. Fig. 4.27b). By comparing IMF 3, 4 and 5 to the noise-free IMFs shown in Fig. 4.14, the Gaussian noise has caused some mode mixing and EMD was not able to extract the exact frequencies of the sine waves. However, removing the first two IMFs will attenuate most of the Gaussian noise in this signal.

To further improve the decomposition of the same input signal, EEMD was implemented by using a SD of 30% and 10 ensembles (cf. Fig. 4.27c). Indeed, EEMD has generated several narrow band IMFs compared to EMD and has also led to better discrimination between frequencies (cf. Fig. 4.27d).

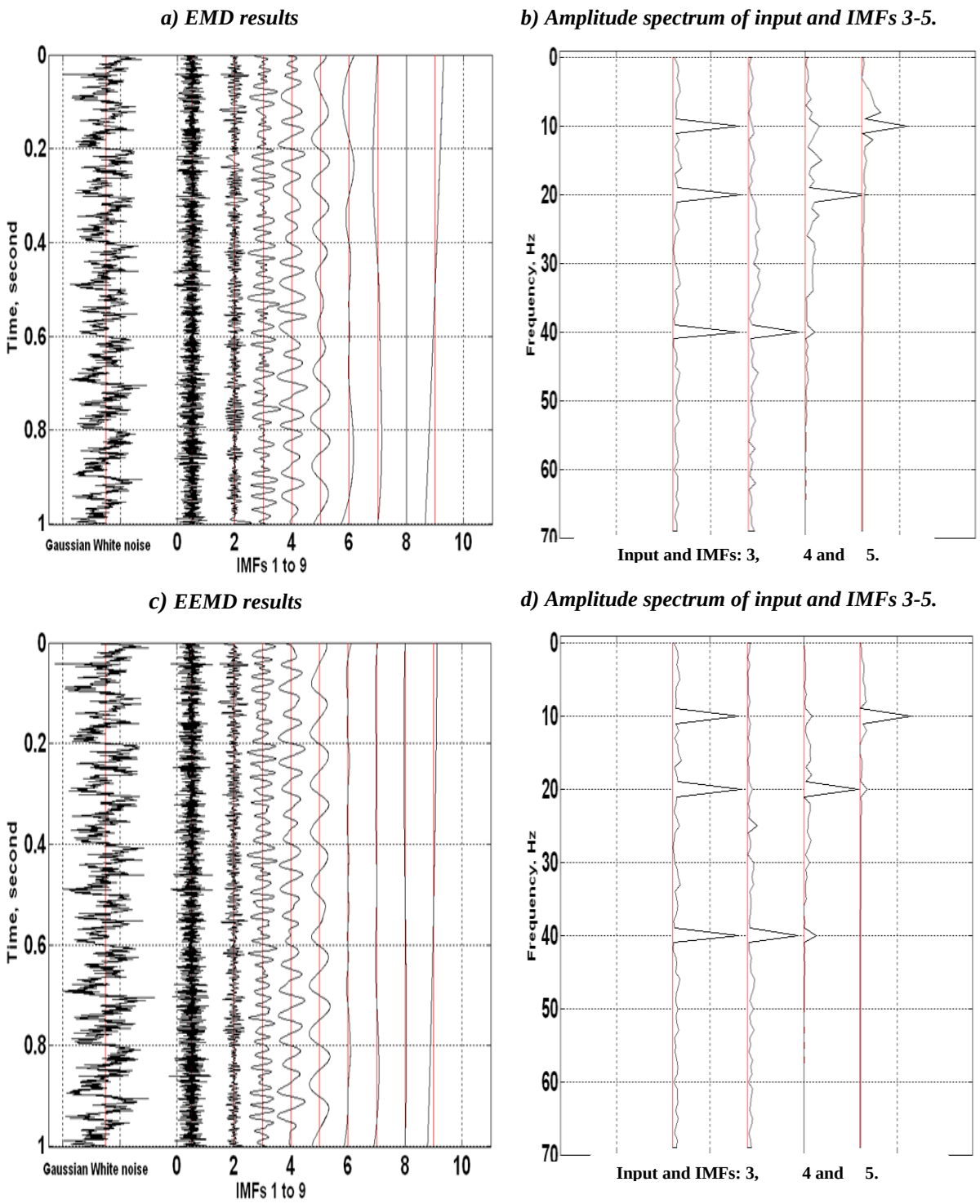

Figure 4.27: *Signal with Gaussian noise and computed IMFs by EMD and EEMD.*

5. EMD SOFTWARE DEVELOPMENT AND IMPLEMENTATION

5.1 Introduction

The EMD technique has been presented in Chapter 4. The process suggested for extracting IMFs is a unique one as introduced by Huang et al. (1998). However, the challenge comes from solving the practical problems associated with a numerical implementation. Chapter 4 discussed some of these problems such as handling end effects, stabilizing the spline fitting of the extrema, and avoiding mode mixing.

Many attempts to improve EMD can be found in the literature. However, one main challenge is that EMD is an empirical method by nature. Chen et al. (2006) introduced an innovative method using B-splines avoiding the use of upper and lower envelopes. Frei and Osorio (2006) also introduced a new method of non-linear and non-stationary time series analysis that finds the mean of the signal without use of extrema envelopes. It generates basis functions similar to the IMF, but without iteration. Battista et al. (2007) introduced a method of solving the mixing mode problem associated with seismic data decomposition in the time-offset domain (cf. Chapter 6).

Several codes exist to perform EMD. Examples are the ones of Rilling et al. (2002), and Wu (2010) with the latter providing both EEMD and 2-D EMD Matlab codes. Battista et al. (2007) have modified the code of Rilling's and used it as a starting point for their work within seismic de-noising in the $f-x$ domain. Bekara et al. (2009) give no details about their EMD code, or how it is applied for de-noising seismic data in the $f-x$ domain.

In this thesis, Wu's EMD code (2010) has been modified to handle seismic data decomposition in both $t-x$ and $f-x$ domains.

5.2 Review of Wu's code

The starting point of this work is the code of Wu (2010). The algorithm makes use of two while loops as described in Chapter 4. The actual Matlab code can be written as:

```
Max_imf_numbers = log2(length (x(t))) -1;
xend = input_signal
current _imf  = 1
while current_imf  < =  Max_imf_numbers
        xstart = xend
        current_iteration =  1
        while current_iteration  < =  Max_iterations
                [location_maxima, value_maxima] = find_local_ maxima ( xstart)
                [location_ minima, value_ minima] = find_local_ minima ( xstart)
                maxima_envelope = spline (location_maxima, value_maxima)
                minima _envelope = spline (location_ minima, value_ minima)
                mean_envelope  = (maxima_envelope + minima _envelope) / 2
                xstart =  xstart – mean_envelope
               current_iteration = current_iteration + 1
        end while   % end iteration loop
 save imfs = xstart
 xend = xend – xstart                % xstart is an IMF, and xend is a residual
current_imf = current_imf  + 1
end while % end IMFs loop
EMD_IMFS = [imfs, xend]
```

The overall effect of the decomposition is to extract the highest frequencies from the input signal. As the number of produced IMFs must be an integer, therefore the program relates has related the number of IMFs to the length of the input signal ***x(t)*** as follows:

$$\textbf{IMF numbers} = log_2\big(length(X((t))\big) - 1 \qquad \textbf{(5.1)}$$

On the other hand, relating IMFs to the length of the signal is advantageous when handling 2-D data such as seismic. This ensures that the same number of IMFs is obtained for all input traces.

Some disadvantages exist associated with this algorithm:

- It does not check whether the input signal is monotonic or not.
- No clear stopping criterion has been specified.
- It does not check for IMF conditions.
- A fixed number of iterations (i.e. 10) is used for maximum iterations.

Kizhner et al. (2004) and Magrin-Chagnolleau (2002) have modified the EMD algorithm by suggesting a combined condition where the iteration is stopped either when the IMF is found, or when the maximum number of iterations is being reached as specified by the user.

By following this idea, the inner while loop in the algorithm is modified as follows:

```
while current_iteration  < =  Max_iterations
      [location_maxima, value_maxima] = find_local_ maxima ( xstart)
      [location_ minima, value_ minima] = find_local_ minima ( xstart)
      maxima_envelope = spline (location_maxima, value_maxima)
      minima _envelope = spline (location_ minima, value_ minima)
      mean_envelope  = (maxima_envelope + minima _envelope) / 2
      xstart =  xstart – mean_envelope
      if  xstart is an IMF
         exit from inner while loop
      else
        current_iteration = current_iteration + 1
      end if
end while   % end iteration loop
```

5.3 EMD implementation used in this thesis

5.3.1 Modified EMD Algorithm

I modified Wu's code to meet the IMF conditions before the program exit from the inner loop. Three stopping criteria have been combined to ensure the efficiency of the IMF output:

- Check for the two IMF conditions (cf. Chapter 4).
- Check that the normalized squared difference between two successive iterations must be smaller than a predetermined value such as 0.2 (cf. Chapter 4) (small value of 0.0000001 is added to the denominator to avoid zero division).
- Allow a high number of maximum iterations (i.e. 1000), as suggested by Battista in his code (2007) (1000 instead of 10).
- Check whether the input signal is monotonic or not, to save decomposition time.

The first criterion must be true in combination with one of the two that follows. This ensures that an IMF has the same numbers of zero-crossing and extrema, and if the squared difference condition is not met after max number of iterations, the algorithm will save the current IMF and move to the next (see Appendix A).

Also, the following ideas have been included when writing the EMD Matlab code (cf. Chapter 4):

- The not-a-knot spline has been used (Matlab function *"spline"*).
- To find the local extrema and numbers of zero crossing, I use the same approach as in the Rilling (2003), and Battista (2007) codes based on the first derivative of the signal.
- Handling end effects of upper and lower envelopes has been done using the Wu (2010) approach (a combination of linear extension based on the two neighboring extrema was used in conjunction of the end point value).

Taking into account this set of stopping criteria, the inner while loop will now look like:

```
        SD =  1 ,  Max_iterations = 1000
while     (xstart is not IMF)    AND
                    [ ( SD > 0.2 )  OR (current_iteration  < =  Max_iterations)]
      [location_maxima, value_maxima] = find_local_ maxima ( xstart)
      [location_ minima, value_ minima] = find_local_ minima ( xstart)
      maxima_envelope = spline (location_maxima, value_maxima)
      minima _envelope = spline (location_ minima, value_ minima)
      mean_envelope  = (maxima_envelope + minima _envelope) / 2
      xprev = xstart
      xstart =  xstart – mean_envelope
      SD =  sum (xperv - xstart)^2 / (sum{(xprev)^2})
        current_iteration = current_iteration + 1
end while   % end iteration loop
```

In addition to the Matlab code, I implemented the EMD technique as a module within CGGVeritas' GeoCluster software. The programming language was Fortran 90 (see Appendix B). This implementation followed closely the Matlab algorithm but a periodic cubic spline was used since the GeoCluster library did not provide a not-a-knot spline function (this is left for a future upgrade of the code). As discussed in Chapter 4, a periodic cubic spline is not the ideal choice.

5.3.2 EEMD

To implement the EEMD another loop is added to iterate over the number of ensembles (Wu 2010). The main computational steps are as follows:

- Add white noise to target data.
- Decompose the data with added white noise into IMFs.
- Repeat the previous two steps for the chosen number of ensemble iterations.
- For a given IMF, compute the ensemble mean as the final result.

The EMD algorithm is modified as follows to include ensemble averaging (EEMD):

```
Max_imf_numbers = log2(length (X(t))) -1;
max_ensemble_numbers = 10
for ensemble_number = 1 to  max_ensemble_numbers
      input_signal = input_signal + random white noise
      xend = input_signal
      current _imf  = 1
  while  current_imf  < =  Max_imf_numbers
        xstart = xend
        current_iteration =  1
                SD =  1
                Max_iterations = 1000
        while      (xstart is not IMF)    AND
                              [ ( SD > 0.2 )  OR (current_iteration  < =  Max_iterations)]
              [location_maxima, value_maxima] = find_local_ maxima ( xstart)
              [location_ minima, value_ minima] = find_local_ minima ( xstart)
              maxima_envelope = spline (location_maxima, value_maxima)
              minima _envelope = spline (location_ minima, value_ minima)
              mean_envelope  = (maxima_envelope + minima _envelope) / 2
             xprev = xstart
              xstart =  xstart – mean_envelope
             SD =  sum (xperv - xstart)^2 / (sum{(xprev)^2})
             current_iteration = current_iteration + 1
        end  while                    % end iteration loop
  save imfs = xstart
  xend = xend – xstart              % xstart is an IMF, and xend is a residual
  current_imf = current_imf  + 1
  end while                         % end IMFs loop
  EMD_IMFS = [imfs, xend]
  ENDFOR                            % end ensemble numbers loop
  EEMD = EMD_IMFS / max_ensemble_numbers
```

6. APPLICATION OF EMD IN DE-NOISING SEISMIC DATA IN THE TIME-SPACE ($t - x$) DOMAIN

6.1 Introduction

In general, any energy interfering with the desired signal can be considered as noise. Separating signal from noise based on temporal and spatial analyses is an important step in seismic data processing. The frequency content of seismic traces varies with time due to the fact that the earth is a non-stationary medium causing attenuation of the seismic waves as they propagate through the medium. It is therefore important to apply techniques which can handle the non-stationarity and non-linear effects in the seismic data.

Several methods already exist to improve the temporal and spectral resolution, such as windowed Fourier transform, wavelet transform, and Matching Pursuit Decomposition. Empirical Mode Decomposition (EMD) is an alternative de-noise technique that can handle non-stationarity.

Flandrin et al. (2004) have shown that EMD acts essentially as a dyadic filter bank resembling those involved in wavelet decomposition by using a numerical experiment based on fractional Gaussian noise (cf. Chapter 4).

Jeng et al. (2007) applied EMD to reduce noise observed in electro-magnetic (EM) data. Bekara and van der Baan (2009) used EMD to reduce the random and coherent noise on seismic data in the frequency-space domain by eliminating the fastest oscillations. Further general improvements of the method have also been reported during recent years (Wu and Huang, 2009).

This chapter discusses the application of EMD to de-noise seismic data in the time-space domain based on the idea proposed by Battista et al. (2007). The main type of noise addressed is cable strum and swell noise. To investigate the technique a synthetic shot gather was generated including real swell noise and a real seismic trace example is then also considered.

6.2 EMD/EEMD de-noising in the $t - x$ domain

Margin-Chagnolleau and Baraniuk (1999) were among the first to apply the EMD method trace by trace in the time-space domain and demonstrating its potential in de-noising of seismic data.

Battista et al. (2007) have applied and shown that EMD can be used to remove cable strum noise from marine seismic data, and they compared their results with frequency filtering techniques in the Fourier domain. I apply my EMD code to the same marine seismic data and this produces the IMFs shown in Fig. 6.1.

Battista et al. (2007) found that the EMD clearly exhibits some weakness in separating weak trends from strong trends, and mixing modes between the noise and signal were present in some IMFs as shown in Fig. 6.1. This particularly occurs when the signal contains strong, low frequency components with weak, higher frequency components riding along.

They also showed that this problem is caused by spline fitting between two extrema separated by a large distance, as a result the missing points lead to artificial extrema (cf. Fig 6.2). As a consequence a weaker signal riding on the trend cannot see any change in the slope (i.e. peaks and troughs are lost in the trend) and the local extrema on the trend are then lost.

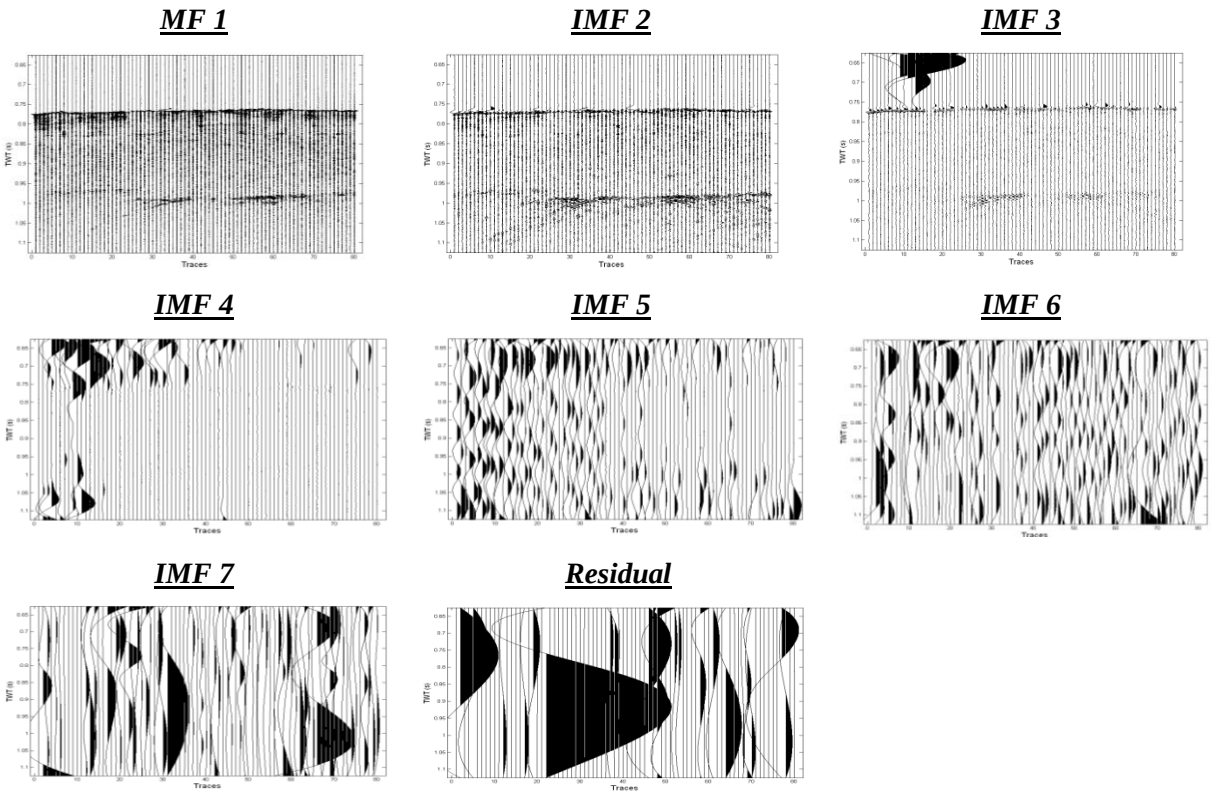

Figure 6.1: *IMFs obtained for a seismic reflection data containing strong, low frequency cable strum.* ***(The IMFs were reproduced with my code from the data provided by Battista et. al. 2007).***

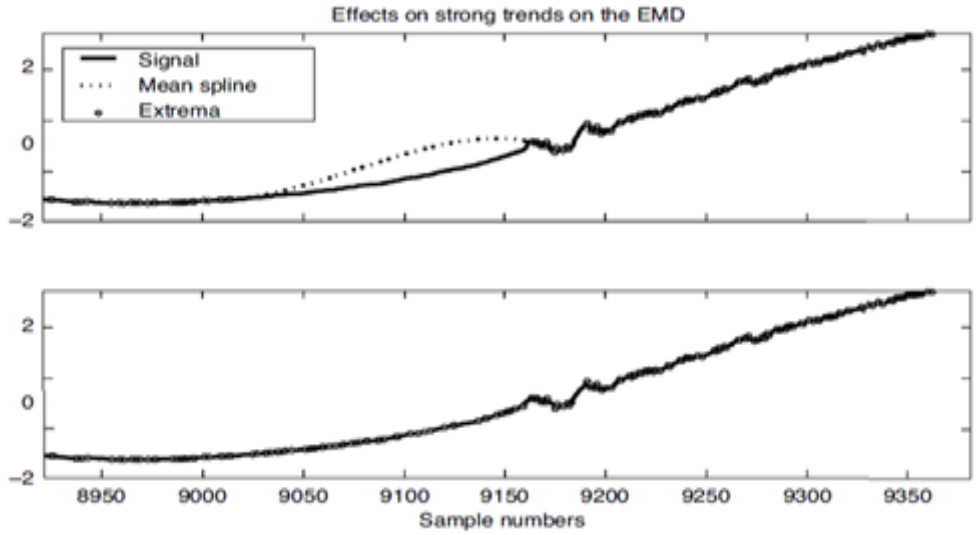

Figure 6.2: *Effects of strong trends on the EMD as function of sample numbers.* ***(Top)*** *Example of how the mean spline can stray from a signal in the presence of a strong trend caused by lack of extrema.* ***(Bottom)*** *Results of Battista's routine that finds the missing extrema to properly constrain the mean spline* ***(Adapted from Battista et. al., 2007).***

The problem is caused by spline fitting between two extrema separated by a large distance, since the missing points lead to artificial extrema as a result (cf. Fig 6.2). As a consequence a weaker signal riding on the trend cannot see any change in the slope which again can lead to loosing the local extrema on the trend.

They suggested a solution by fitting the portion suffering of this problem with a third order polynomial that is subtracted before locating the extrema. In addition, the effect of an artificial false trend is minimized by using well-constrained mean splines. This solution leads to IMFs with narrower bandwidths than before and consequently to better filtered results, as can be seen from Fig. 6.3. This figure shows the filtering results before (cf. Fig. 6.3b), and after (cf. Fig. 6.3c) correction; we see that after correcting for strong trends EMD, decomposition is able to remove all cable strum noise efficiently.

a) Original data

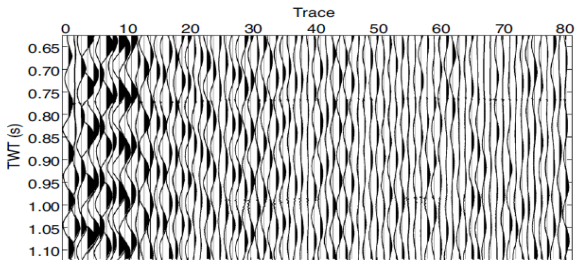

b)Output <u>before</u> solving the effects of strong trends

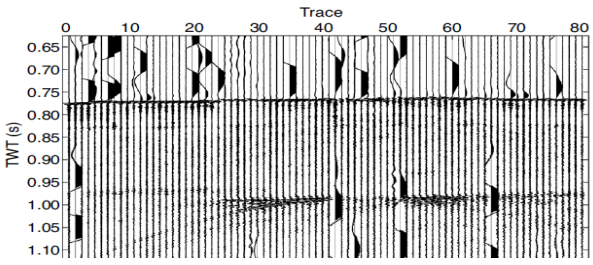

c) Output <u>after</u> solving the effects of strong trends

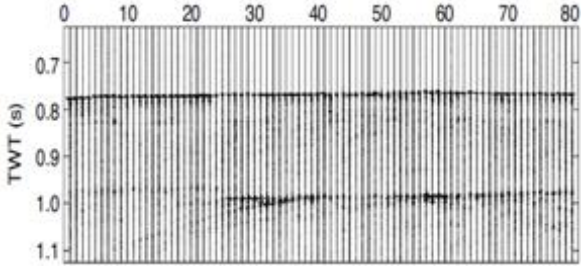

d) Attenuated noise after solving the effects of strong trends

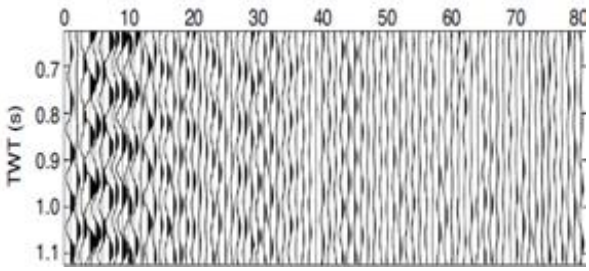

Figure 6.3: *Single-channel seismic reflection data containing strong, low frequency cable strum and EMD filtered result before/after solving the effects of strong trends.* ***(Adapted from Battista et. al., 2007).***

Huang and Wu (2009) addressed a better solution for the mixing mode problem and introduced the Ensemble Empirical Mode decomposition EEMD that reduces spectral leakage. EEMD cleverly uses noise perturbations to force the EMD algorithm to explore all the frequencies while not adding too much noise so as to push the EMD algorithm into the spectral leak. Spectral and temporal pre-whitening techniques are commonly used in deconvolution. Pre-whitening methods effectively control the spectral content of the trace. For this reason pre-whitening techniques can be considered as a possible tool for solving the mixing mode problem exhibited in EMD, and be used to decompose the data into IMFs with narrower bandwidths than EMD itself (cf. Section 4.4.3).

I have applied the EEMD decomposition to the same data as above (as used by Battista et al., 2007) by using 10 ensembles and white noise with a standard deviation of 30%. I obtain the set of IMFs shown in Fig. 6.4.

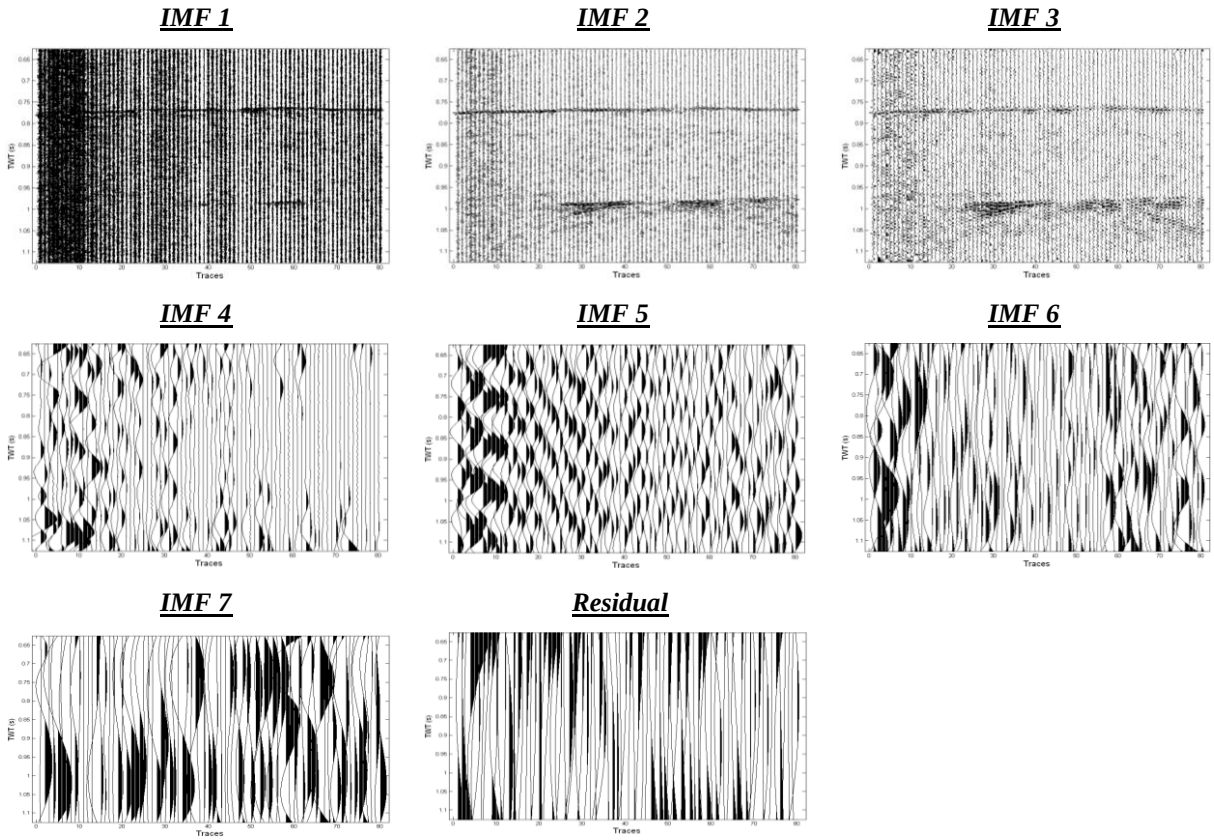

Figure 6.4: *EEMD decomposition results of seismic reflection data containing strong, low frequency cable strum.* ***(The data for these tests is provided by Battista et. al., 2007).***

Visually, the last four IMFs, together with the residual carry all the cable strum noise. Fig. 6.5 shows the filtering result of EEMD after removing the last four IMFs and the residual from the original noisy data. By comparing the EEMD filtering results with those of Battista (cf. Fig. 6.3c, and d) clearly EEMD is able to give a good decomposition of the data, and achieves a good cable strum noise filtering compared to that found by Battista et al. (2007).

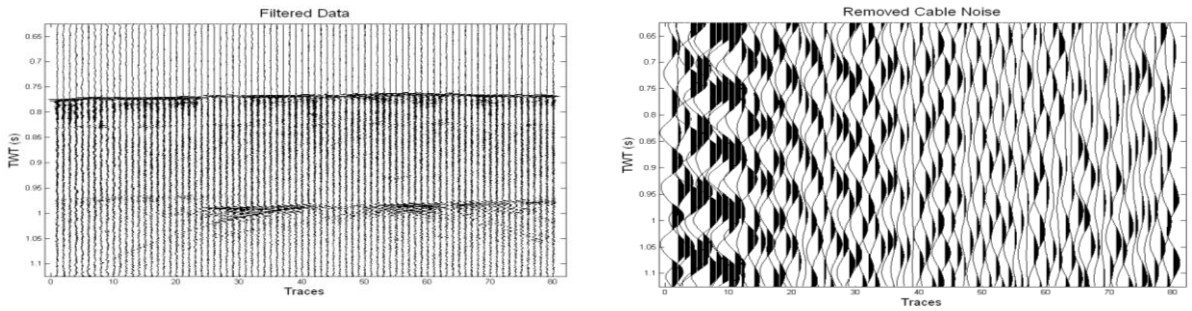

Figure 6.5: (Left) *EEMD filtered data.* ***(Right)*** *Difference data, cable strum noise.* ***(The data for these tests is provided by Battista et. al., 2007).***

6.2.1. Synthetic dataset with swell noise

Swell noise normally falls within the frequency band between 0 and 15 Hz and I will apply EMD and EEMD filtering techniques to data with swell noise in the time-space domain. Figure 6.6, shows real swell noise together with its amplitude spectrum. This swell noise has been removed from actual field data. This allows me to add the noise to a synthetic reflection model (cf. Fig. 6.7), for a controlled test, where the signal-to-noise-ratio is known.

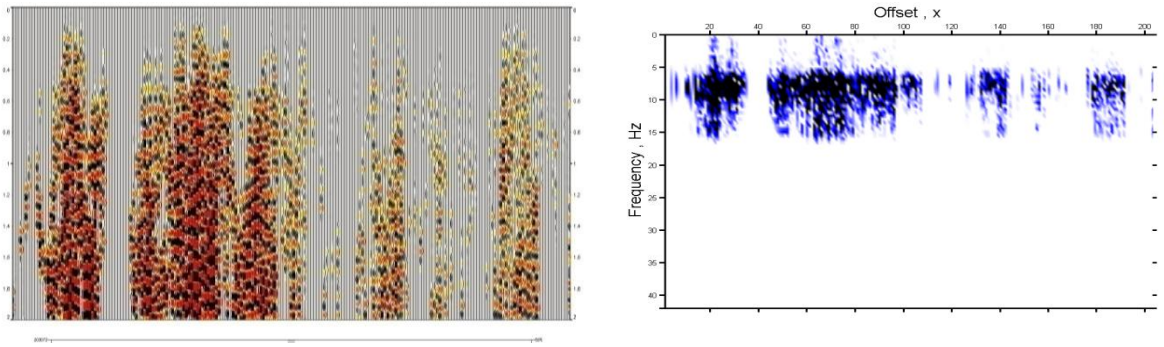

Figure 6.6: (Left) *Real swell noise.* ***(Right)*** *Amplitude spectrum of the swell noise.*

The synthetic reflection model consists of five constant amplitude events corresponding to interval velocities of 1500, 2000, 2500, 3000, and 3500 m/s (cf. Fig. 6.7). A total of 200 traces were generated with a sampling interval of 1 msec and a total time recording of 2 second; offsets range from 1 to 200 meter. The pulse was a Ricker wavelet with a center frequency of 50 Hz. Fig. 6.7 also shows the amplitude spectrum of this synthetic data.

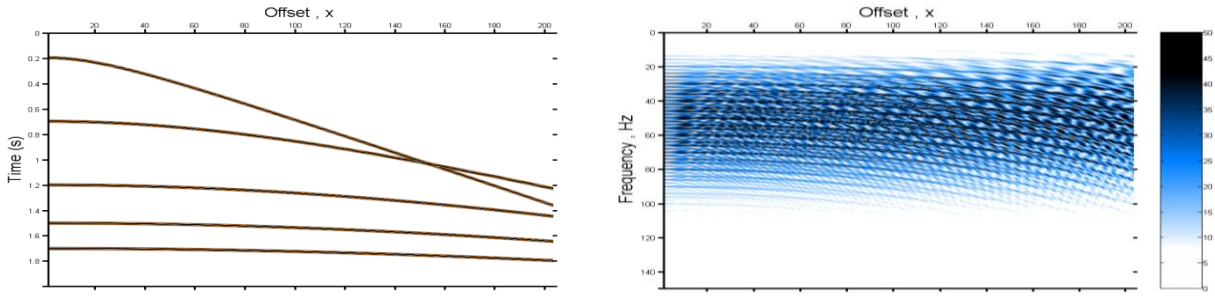

Figure 6.7: (Left) *Synthetic reflection model in $t-x$ domain.* ***(Right)*** *Amplitude spectrum of the synthetic data.*

Synthetic test data were now generated (cf. Fig. 6.8) by adding the synthetic reflection data in Fig. 6.7 to the swell noise in Fig. 6.6. The overall goal of this test was to investigate the ability of EMD and EEMD to separate swell noise from primaries. The result of the EMD applied on the dataset in the $t-x$ domain is shown in Fig. 6.8. A total of 9 IMFs plus residual have been computed. The spectral leaking of the noise is observed in all the lower IMFs and causes all generated IMFs to be noisy. Therefore EMD is not able to give a good signal and noise separation. In particular, mixing between signal and noise can be seen in the first three IMFs.

To further investigate the mixing mode problem, I now use EEMD to decompose the same data; by applying random noise with standard deviation of 30% and running it 10 iterations on the original dataset.

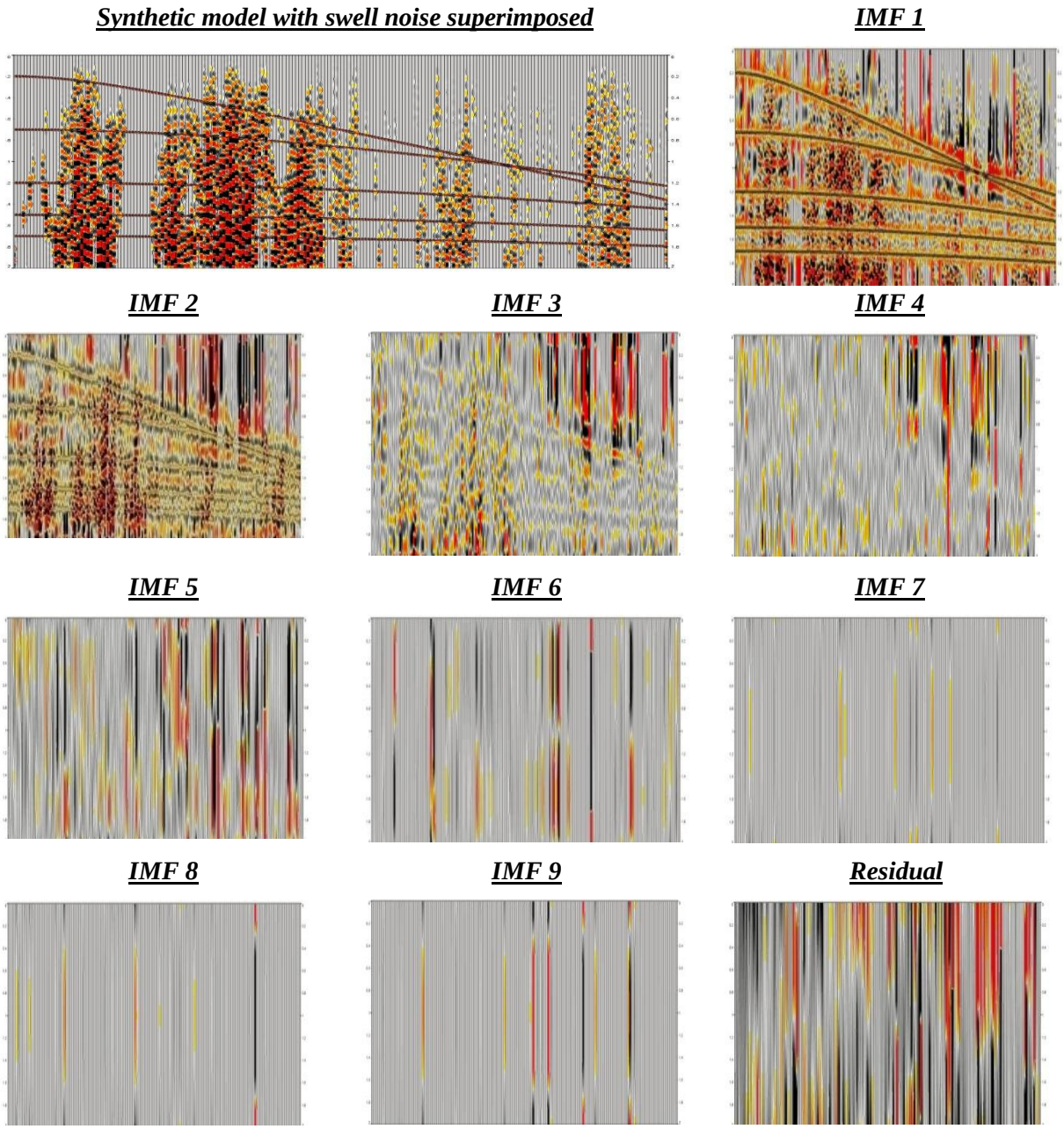

Figure 6.8: *IMFs output from* ***EMD*** *when applied to synthetic model*

Figure 6.9 shows that the IMFs of the EEMD have a much narrower frequency bandwidth compared to EMD. The EEMD also gives a better discrimination between signal and noise. Visually, IMF 1 carries a small portion of primaries with some noise as an artificial effect of using EEMD, IMFs 2-3 carry only primaries, and mixing modes mostly appear in IMF 4 and IMF 5 and also with a small amount in IMF 6. EEMD has performed a better decomposition of the signal and noise than EMD.

However, mixing modes are still present in some IMFs, although the first IMFs carry mostly signal in addition to some artificial EEMD noise.

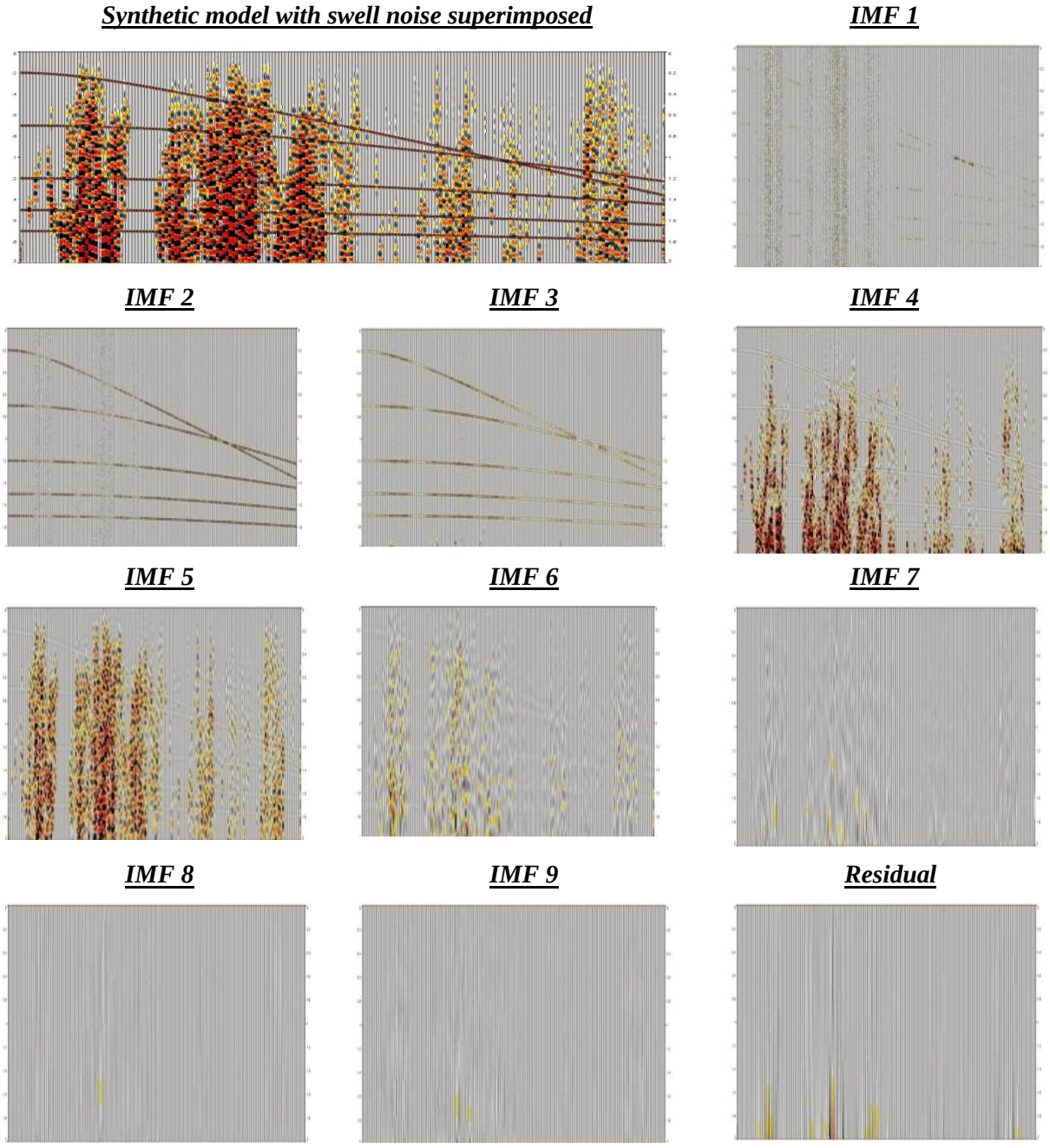

Figure 6.9: *IMFs output from* ***EEMD*** *when applied to synthetic model*

Inspection of the calculated IMFs in Fig. 6.9 shows that they can be classified into three kinds:

1) Signal: IMFs 1-3 that carry most of the reflection events, and their RMS amplitude are shown in Fig.6.10 compared to the signal. The RMS power shows that IMF 1 has some remaining high frequency components as an artificial effect of EEMD that makes it less suitable to recover the signal.

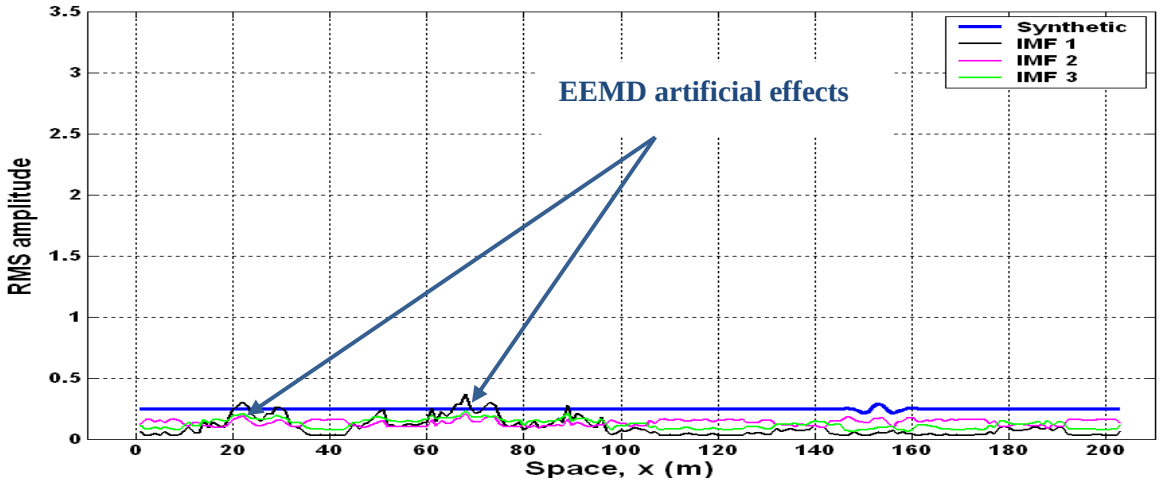

Figure 6.10: *The RMS amplitude of the synthetic reflection and IMFs 1-3.*

2) Transition: IMFs 4-6 carry residual signal and noise, while IMF 7 carries only some swell noise. Figure 6.11 shows their RMS amplitude compared to superimposed noise.

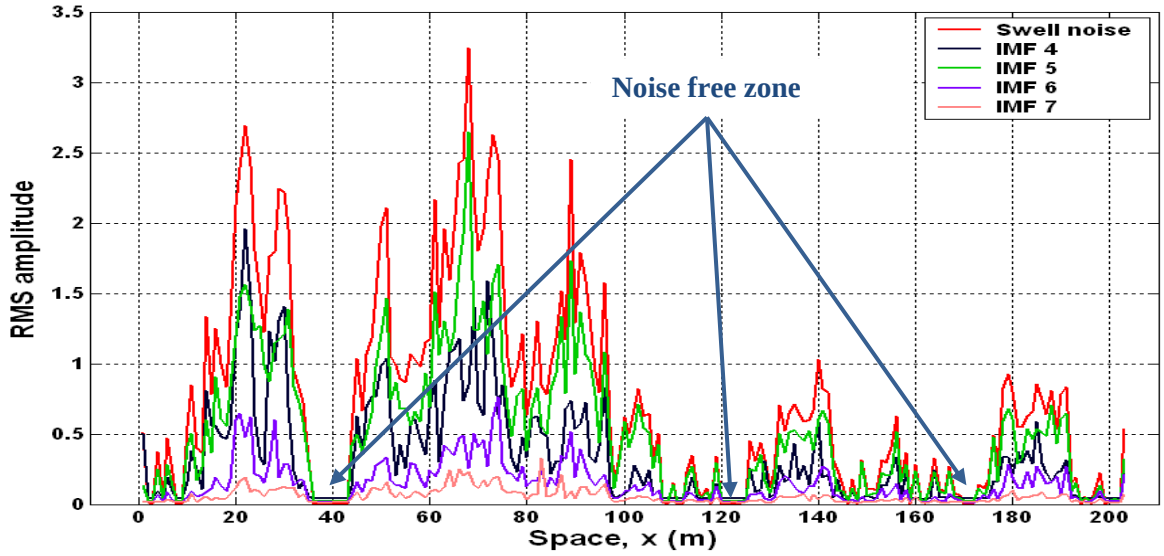

Figure 6.11: *The RMS amplitude of the superimposed swell noise and IMFs 4-7.*

3) Monochromatic: IMFs 8-10 are nearly monochromatic. Figure 6.12 shows their RMS amplitude compared to the signal.

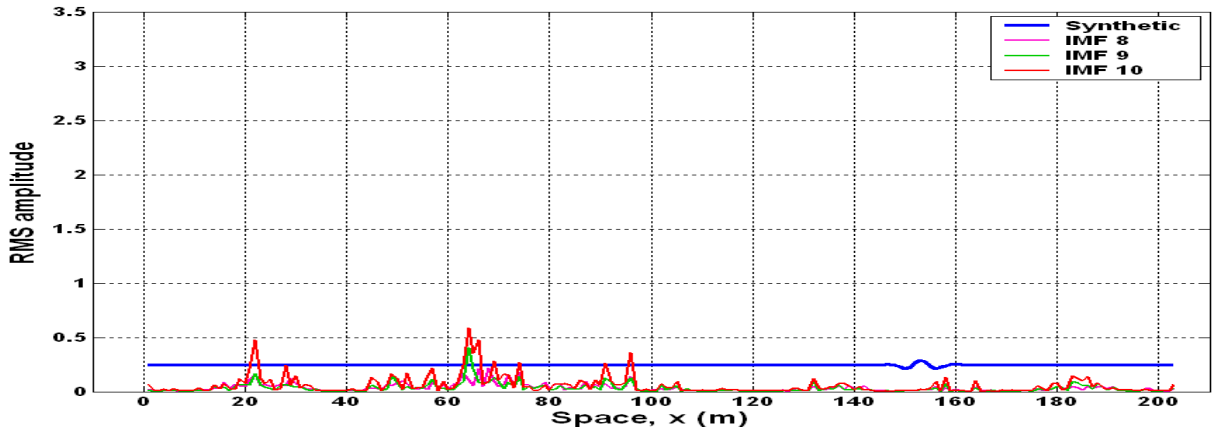

Figure 6.12: *The RMS amplitude of the synthetic and IMFs 1-3.*

The filtered data can be obtained by removing IMFs 4-10 from the noisy dataset. Clearly some leakage is present in the filtered noise section. The amount of leakage is shown in Fig. 6.13 based on the RMS amplitude of the filtered data. The attenuated noise section also shows some leakage of the signal especially in areas where no noise was present in the original dataset.

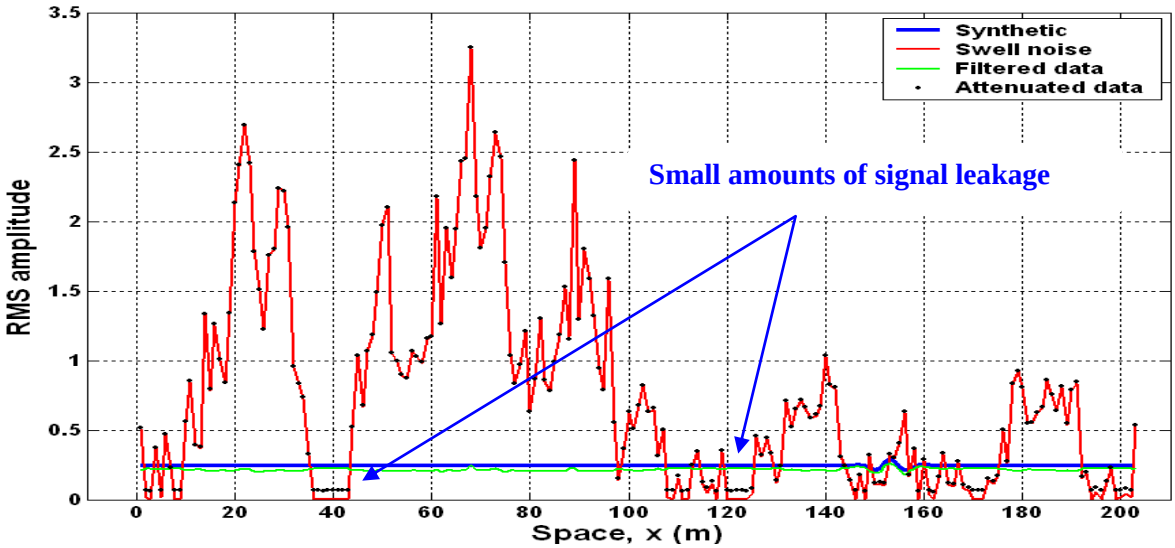

Figure 6.13: *The RMS amplitude of the synthetic, swell noise, filtered dataset and attenuated noise.*

6.2.2 EEMD of real seismic trace with swell noise

The seismic trace employed is shown in Fig 6.14 and consists of 2000 samples (sampling interval of 1 msec). It contains low frequency; high amplitude swell noise associated with higher frequency components which makes the noise complicated to deal with. As before I now also test EEMD using noise with standard deviation of 30% and 10 ensembles. A total of 9 IMFs plus residual have been computed and based on these (cf. Fig. 6.14), four categories of IMFs can be identified:

1) Signal: IMFs 1-3 contain most of the signal.
2) Transition: IMFs 4-5 contain both signal and swell noise. This IMF captured the "transition" from the signal in IMFs 1-3 and the swell noise in IMFs 6-7.
3) Noisy: IMF 1 contains some residual noise as an artificial effect of EEMD and IMFs 6-7 contain swell noise with signal.
4) Monochromatic: IMFs 8-9 plus residual are nearly monochromatic.

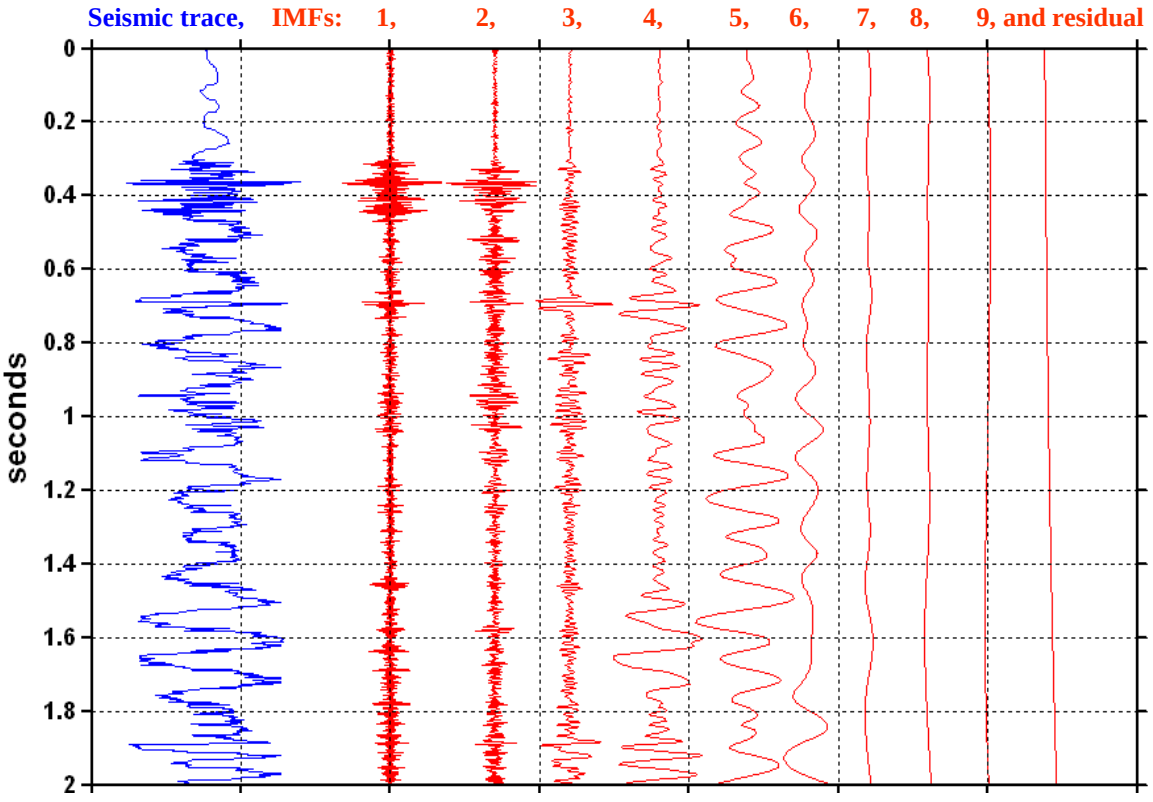

Figure 6.14: *The seismic trace and its corresponding IMFs plus residual.*

Figure 6.15 shows the amplitude spectrum of this seismic trace, which is heavily contaminated with swell noise, and its corresponding IMFs generated by the EEMD.

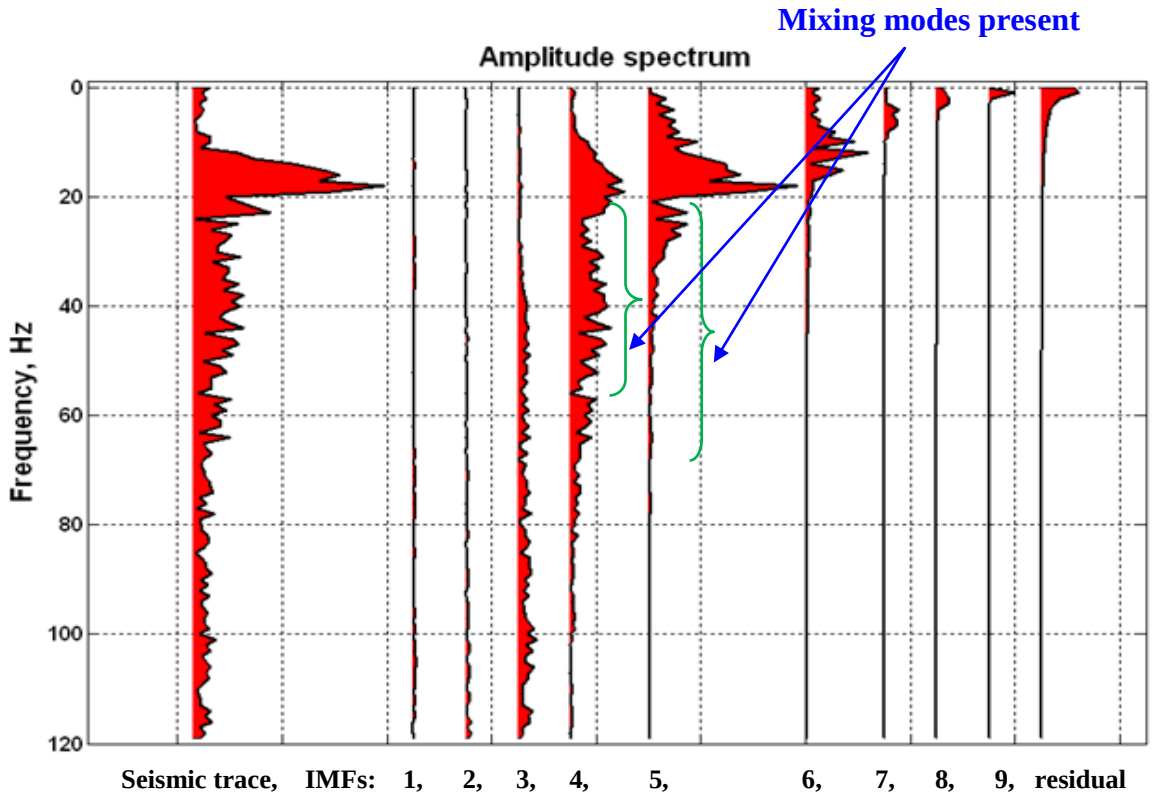

Figure 6.15: *Amplitude spectrum of the seismic trace and its corresponding IMFs plus residual.*

Clearly, the amplitude spectra of the IMFs reflect the EEMD filter bank behavior. In case of IMFs 4-5, the signal frequency is low enough to be included in the same IMF as most of swell noise. EEMD extracts both the signal and noise as it cannot distinguish between them. Because of the variation in the boundaries of the identified frequency bands, EEMD will encounter such a band even when decomposing a noisy non-stationary signal; therefore, this is the general process that leads to the creation of a transition IMF (Kaslovsky and Meyer, 2010).

6.3 Discussion

The seismic signal is clearly non-stationary; therefore transition IMFs were formed due to spectra leakage. More precisely, application of EMD/EEMD to synthetic and real data produces noisy IMFs, which represent neither pure target reflections nor noise.

By comparing the EMD and EEMD decomposition, transition IMFs were reduced from three to only one in case of the latter. With an understanding of how transition IMFs are generated, we can address the more fundamental question of why transition IMFs are produced when EEMD operates on a noisy dataset. As a start we note the work of Flandrin and Goncalves (2004) showing that EMD behaves as a filter bank when decomposing pure Gaussian noise (also boundaries of the frequency bands vary with time) (cf. Chapter 4). Two mechanisms have been described by Kaslovsky and Meyer (2010) that lead to the creation of transition IMFs:

- Spectral leak between frequency bands: frequency content of the underlying signal falls within a band treated as noise. Spectral leak is mostly a non-stationary condition.
- Phase alignment: the alignment of the signal with the lowest level of noise presented in the band is controlled by the phase of the signal. Phase alignment is seen mostly within a stationary setting. As a result, when the energy of noise is high, the energy of the signal cannot be sensed by the algorithm, because the noise is preventing the signal from being extracted. However, if the energy of the noise is small, EMD may include part of the underlying signal in the current IMF as well.

Kijewski-Correa and Kareem (2007) attributed the poor quality of IMFs in case of the presence of noise to the empirical nature of the EMD algorithm, leading to a basis derived from the noise. EMD results show a wide distribution of the target reflections over many IMFs, making it difficult to isolate them from the associated noise, because the EMD extracts the noise in a nearly dyadic fashion that makes the frequency bands vary with time.

EEMD cleverly uses noise perturbation to force the EMD algorithm to explore all the frequencies while not adding too much noise so as to push the algorithm into the spectral leak regime. EEMD represents an effective way of eliminating mode mixing but we saw that for swell noise, spectral leakage between IMFs is still a challenge.

7. DE-NOISING OF SEISMIC DATA IN THE FREQUENCY-SPACE ($f-x$) DOMAIN BY USING EMD

7.1 Introduction

Spatial prediction filtering techniques in the frequency-space $(f-x)$ domain have been developed to attenuate random noise that remains after stacking. The main advantage of the spatial prediction method is the preservation of relative amplitudes and signal character. For more details about $f-x$ deconvolution, the reader is referred to Chapter 3.

Noise free linear events in the $t-x$ domain are mapped into a superposition of harmonics in the $f-x$ domain. The $f-x$ deconvolution filtering can be used to predict these harmonics. However, a short spatial window has to be used in $f-x$ deconvolution to handle the non-stationary and nonlinear events. Linear events in the $f-x$ domain are periodic along x direction which allows the prediction technique to be performed on individual frequencies (Gulunay, 1986). Figure 7.1 shows how the superposition of harmonics changes in the $f-x$ domain as a function of the dip of a linear event in the $t-x$ domain.

Equation (3.5) in Chapter 3 predicts the behavior of a linear dipping event in the $f-x$ domain. For a linear event with a known dip in the $t-x$ domain a periodicity exists along the spatial axis for a fixed frequency. In the special case of a horizontal event the periodicity goes to zero (dc). Since EMD has the capability of separating frequencies, it should have the ability of dip filtering in the $f-x$ domain (cf. Fig. 7.1). Figure 7.2 shows how the real parts of the Fourier transform of a 40 Hz signal vary in space as a function of dip or apparent velocity (cf. slices in Fig. 7.1). The periodicity increases with increasing dip in the $t-x$ domain.

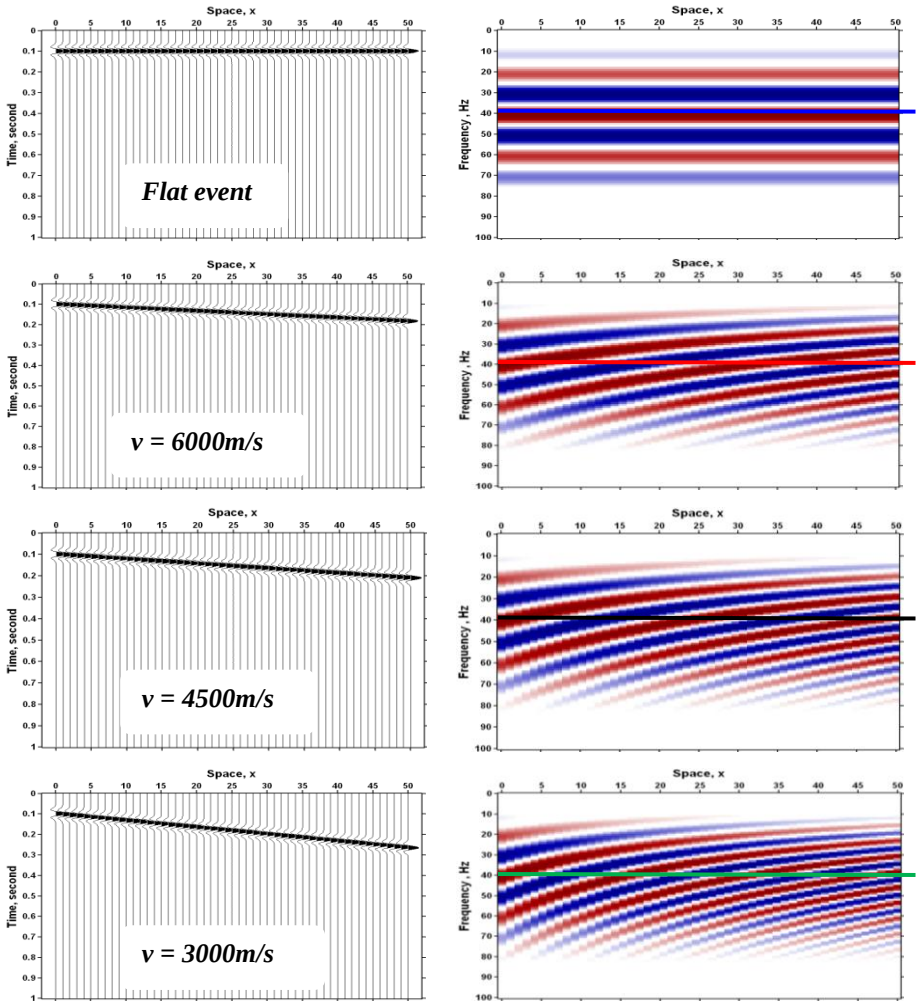

Figure 7.1: *Various linear coherent events: (left) in the $t-x$ domain; (right) the real part of the Fourier transformed events in the $f-x$ domain.*

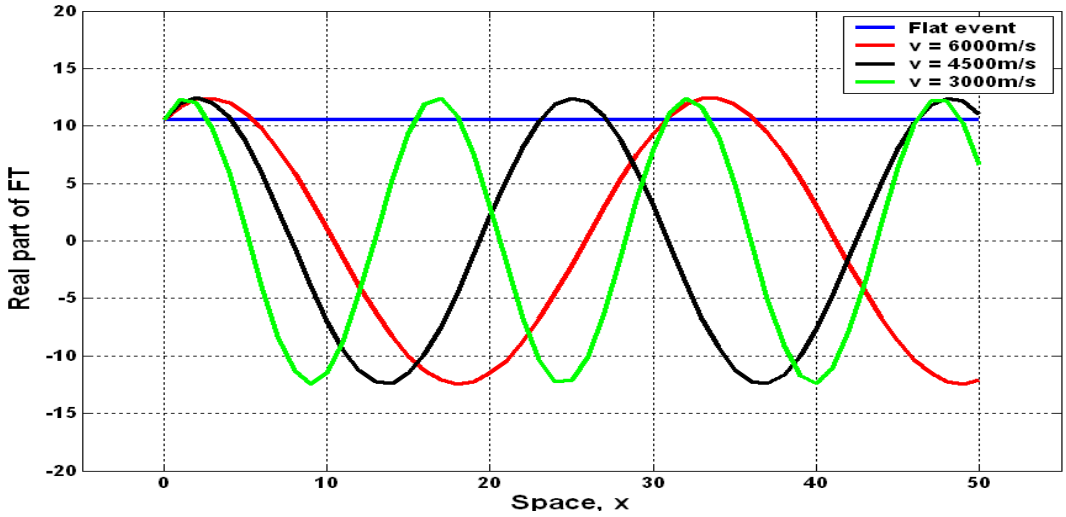

Figure 7.2: *The real part FT of a 40 Hz signal vs. space various dips or apparent velocities.*

7.2 EMD de-noising technique in the $f-x$ domain

Chapter 4 discussed how EMD can be used to decompose a signal into different modes of oscillation. IMF 1 always captures the fastest oscillating mode in the signal. Subtracting IMF 1 from the input signal will therefore eliminate the fastest oscillations of the signal (Bekara and van der Baan, 2009). For seismic data in the $f-x$ domain, random noise and steeply dipping coherent noise such as refracted waves, ground roll, and interference noise are mapped into higher oscillating harmonics while the desired signal mostly contributes to the lower oscillating harmonics. Decomposing the data into IMFs along a constant frequency slice in the $f-x$ domain and removing IMF 1 or IMF 1 and 2 from the original data will enhance the SNR since random and linear coherent noise will be attenuated.

The process of obtaining the IMFs from the seismic data in the $f-x$ domain can be implemented as follows:

a) Apply 1-D Fourier transforms to each trace to transfer data from time to frequency domain.
b) For every frequency:
    1. Separate the real and imaginary parts of the spatial sequence.
    2. Apply EMD to the real part to decompose into IMF_{real}.
    3. Apply EMD to the imaginary part to decompose into IMF_{imag}.
    4. Construct IMFs as follows: $= IMF_{real} + i\, IMF_{imag}$.
c) Transfer the IMFs back to the $t-x$ domain by applying an 1-D inverse Fourier transform to each trace.

The $f-x$ EMD filtering technique subtracts unwanted IMF(s) from the input data. IMF 1 and sometimes in combination with IMF 2 capture random noise and steeply dipping coherent noise present in the data. The process of $f-x$ EMD filtering depends on the frequency content of each trace (cf. Fig. 7.3). Consequently, bad traces should be edited before decomposing the data in the $f-x$ domain to avoid any unwanted distortions in the IMFs.

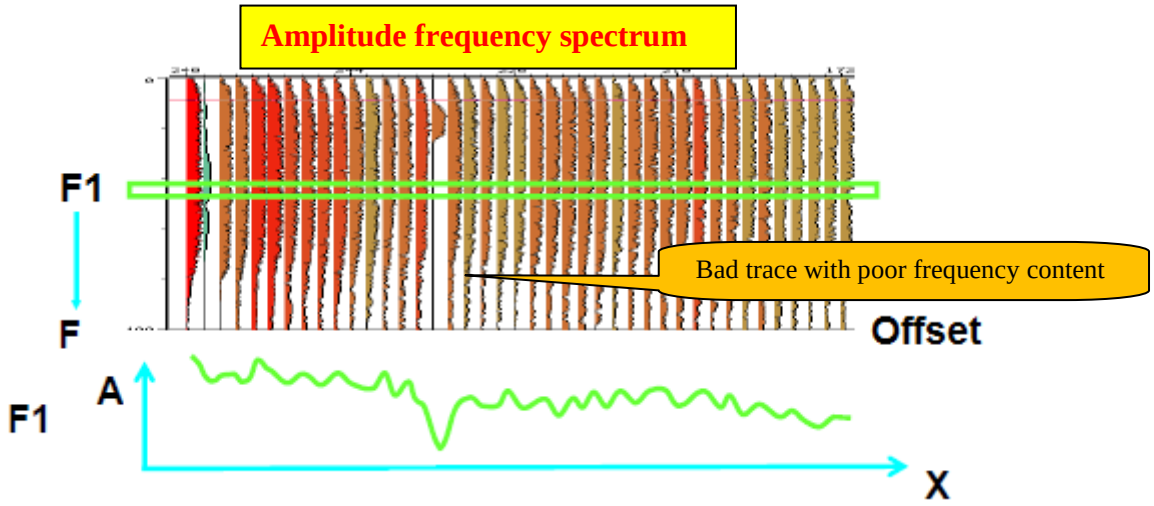

Figure 7.3: *Seismic traces in the $f-x$ domain including a bad trace (after CGGVeritas).*

7.2.1 Synthetic dataset

Figure 7.4 shows a synthetic model that contains one horizontal and three linear dipping events with constant amplitudes. The dipping events are characterized by apparent velocities of 1000, 2000 and 4500m/s. A total of 101 traces were generated, with a sampling interval of 1 msec, a total recording time of 2.5 seconds, and offset was ranging from 0 to 1000m. A Ricker wavelet was used as a pulse with a center frequency of 50 Hz. A small amount of random noise has been added to the synthetic model to stabilize the $f-x$ EMD process (cf. Figs. 7.4). The EMD $f-x$ decomposition generated a total of three IMFs plus a residual. The first contains only the steepest dipping coherent event (i.e. 1000m/s) the second contains the middle steepest dipping event (corresponding to 2000m/s) and the third return the lowest steepest event (i.e. 4500m/s), while the residual contains the flat event. Hence, $f-x$ EMD can mimic the effect of apparent velocity filtering.

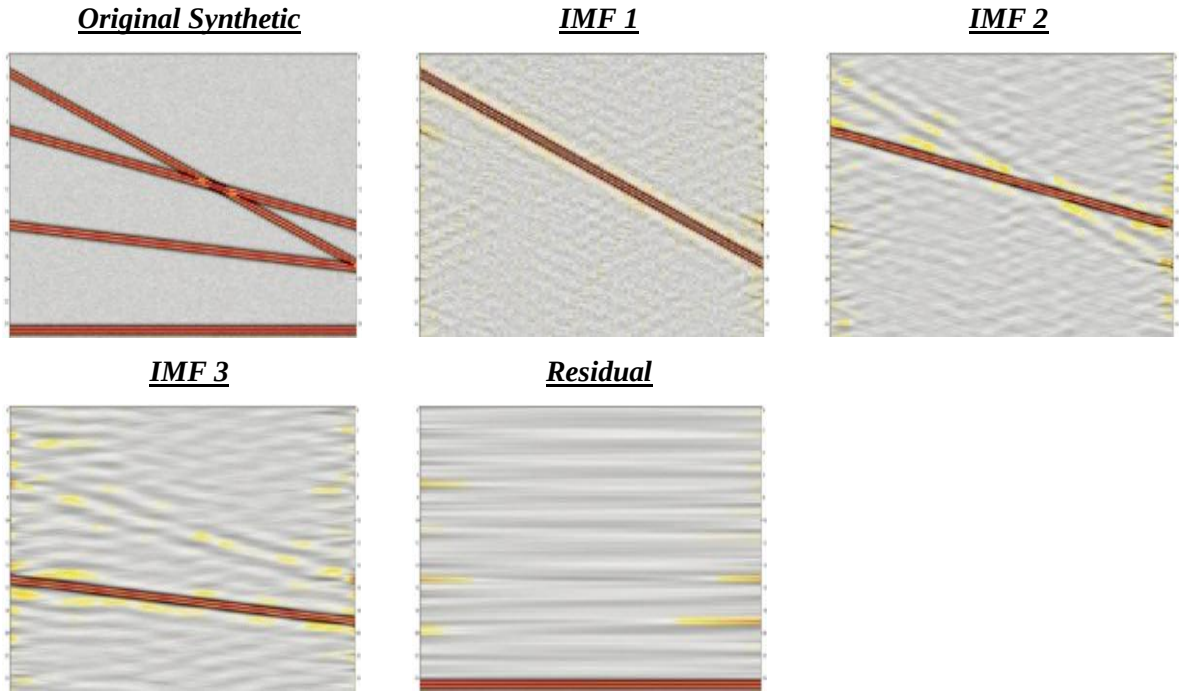

Figure 7.4: *IMFs output from $f-x$ EMD in case of linear coherent events.*

To further investigate this ability a new synthetic example was considered. It consists of a gather with five reflected events (cf. Fig 7.5). The total number of traces is 328, each trace with a maximum recording time of 2 seconds, and sampling interval of 1 msec. A Ricker wavelet is used with a center frequency of 50 Hz. I superimpose real ground roll on the synthetic data to generate the test data set shown in Fig. 7.5. This figure also shows the corresponding results after Fourier transformation (real part only).

I now apply the $f-x$ EMD technique to the test dataset in Fig. 7.5. A total of 7 IMFs plus the residual were obtained (cf. Fig. 7.6). The first IMF includes the high frequency noise, some ground roll noise and the steepest dipping parts of the reflected coherent events. The second IMF includes also parts of reflections and most of the remaining part of the ground roll noise. The remaining IMFs include the residual of the events as well as the low frequency components of the dataset.

Synthetic model

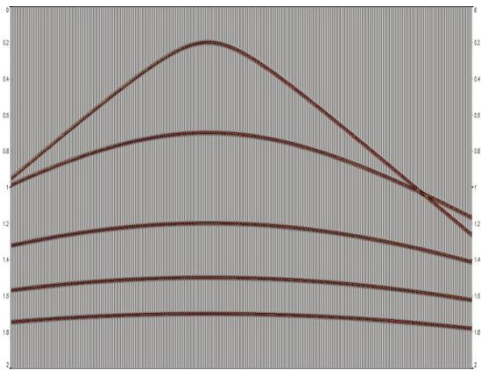

Real part spectrum in the $f-x$ domain

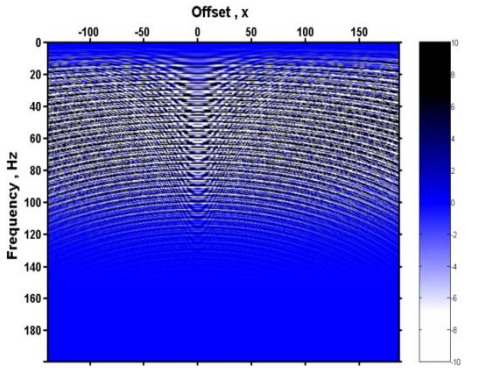

Real ground roll noise

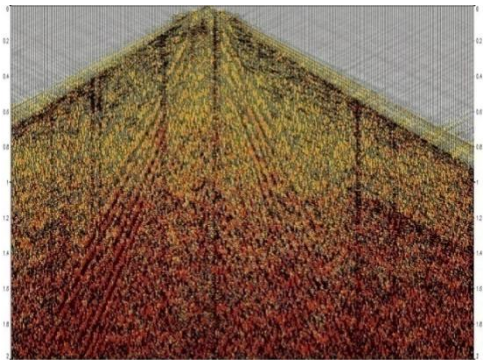

Real part spectrum in the $f-x$ domain

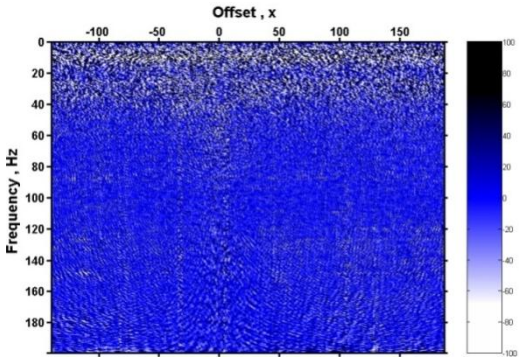

Test dataset

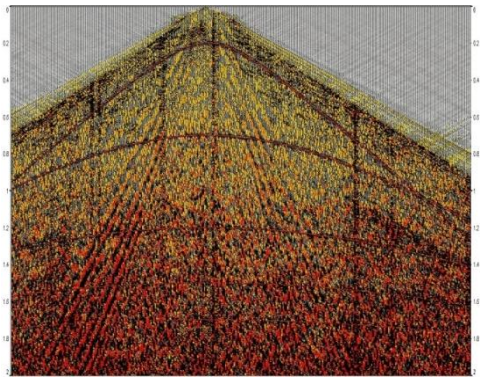

Real part spectrum in the $f-x$ domain

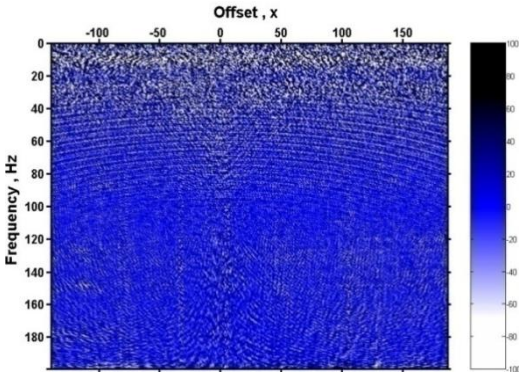

Figure 7.5: *The synthetic dataset with real ground roll noise superimposed.*

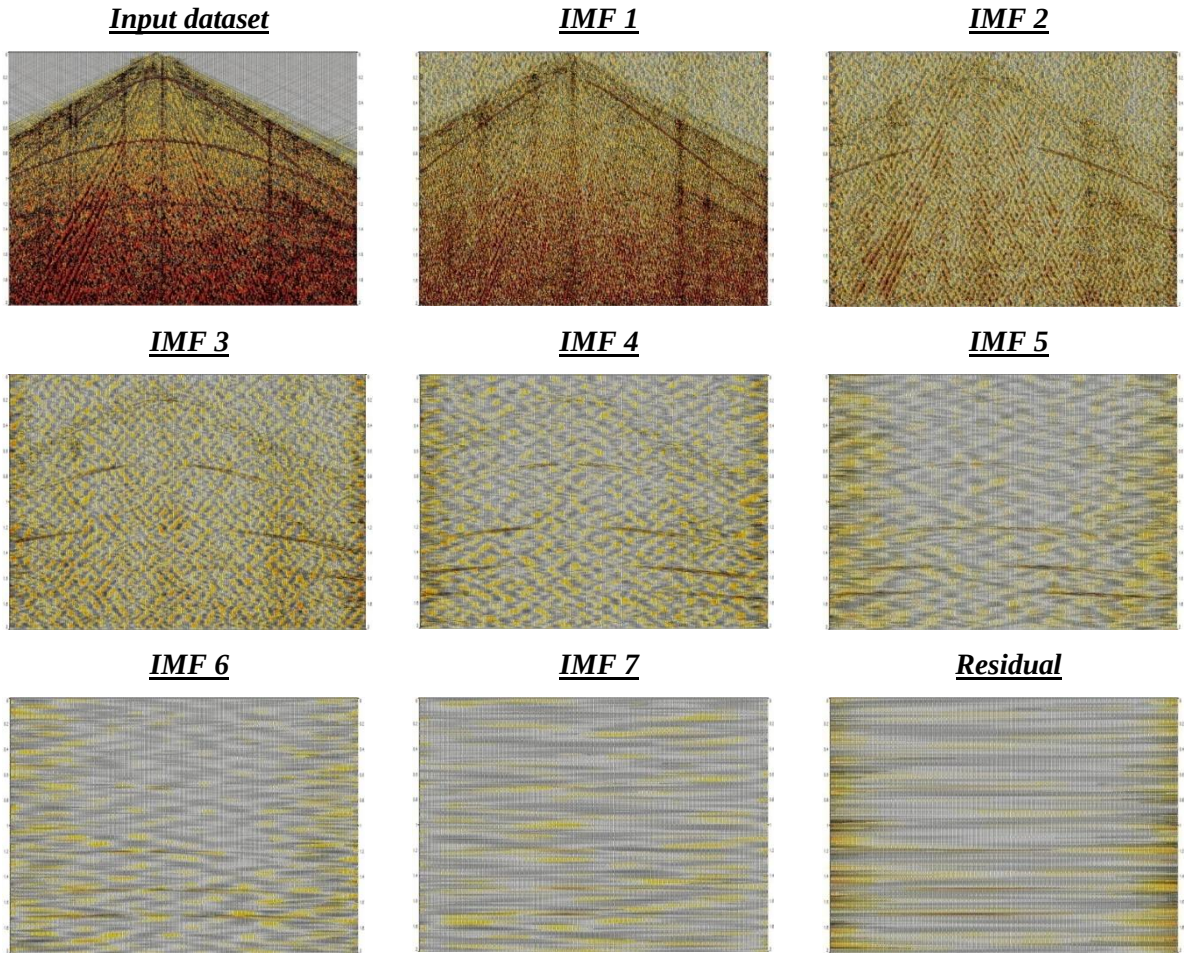

Figure 7.6: *IMFs resulting from $f-x$ EMD of the synthetic refection model with ground roll.*

The RMS power of the signal, ground roll noise, and resulting IMFs are shown in Fig. 7.7. IMF 1 carries the highest level of RMS amplitude present in the dataset and with the residual carrying the lowest. The sum of the RMS amplitude of the IMFs equals the RMS amplitude of the input dataset. The EMD process caused some overshooting in the RMS amplitude caused by using the cubic spline to extract the IMFs from the dataset. The best $f-x$ EMD filtered result is obtained by subtracting IMFs 1 and 2 from the original dataset, because they carry most of the ground roll noise present in the dataset (cf. Fig. 7.8). The filtered section shows that the $f-x$ EMD technique performs quite well and is able to attenuate most of the ground roll noise present in the dataset. However, inspection of the difference section shows that the steepest parts of the reflected events have been removed as well (cf. Fig 7.8). This cannot be avoided if both noise and signal have similar dips.

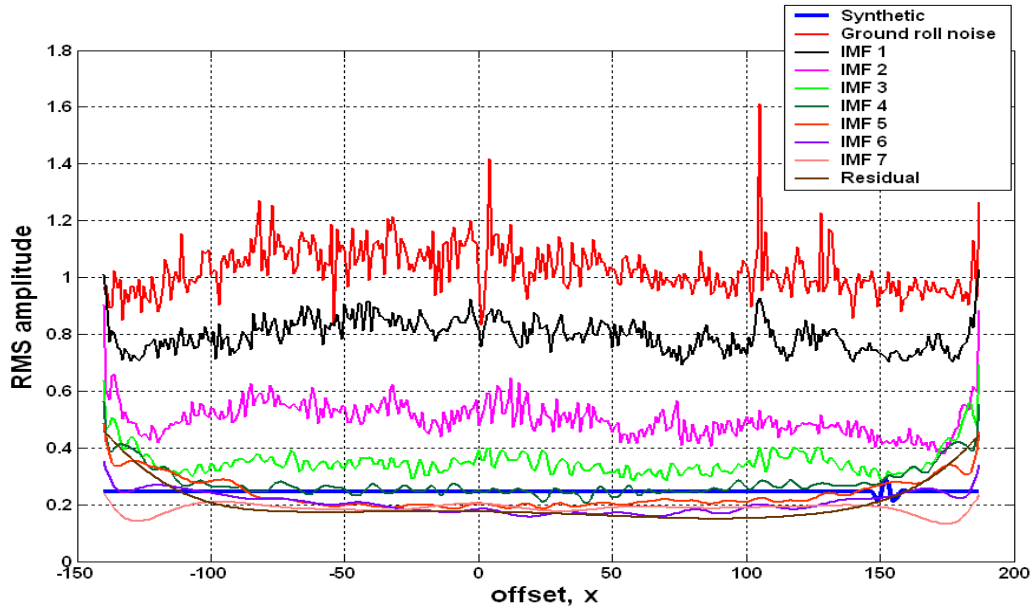

Figure 7.7: *RMS amplitude of the synthetic dataset, ground roll noise, and resulting IMFs.*

Input dataset

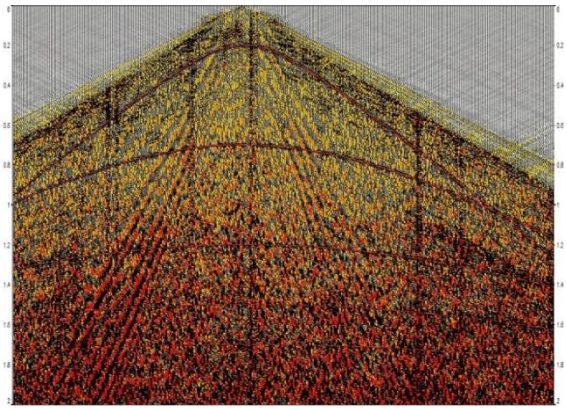

Output from $f-x$ EMD filtering technique

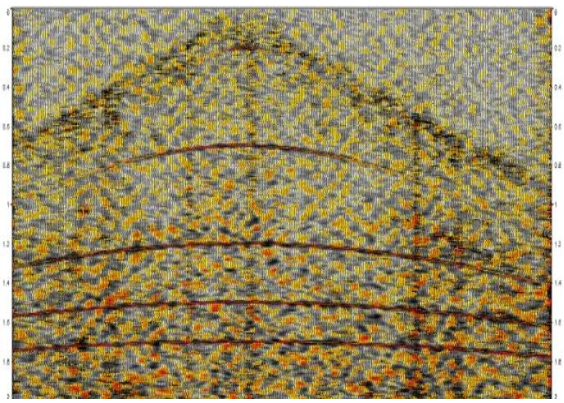

Difference (i.e. IMF 1 and 2)

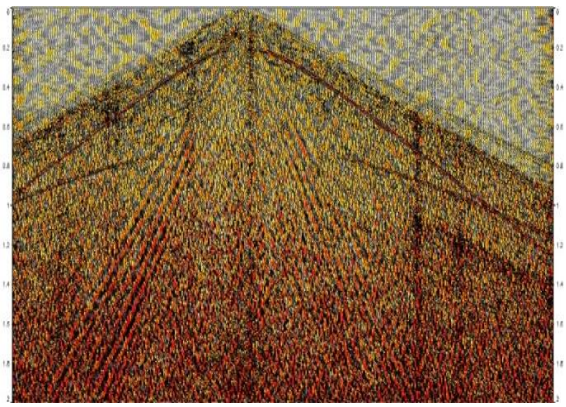

Figure 7.8: *Output and difference data obtained using $f-x$ EMD filtering.*

The filtered section output from the $f-x$ EMD technique shows that some low and high frequency noise have survived in the later IMFs (3-7). To further improve this result, I apply a $t-x$ trace-by-trace EEMD technique using noise with standard deviation of 30% and 10 ensembles. The corresponding ensemble IMFs obtained are shown in Fig. 7.9. It now appears that the new IMF 1 contains all high frequency noise present in the $f-x$ EMD filtered section.

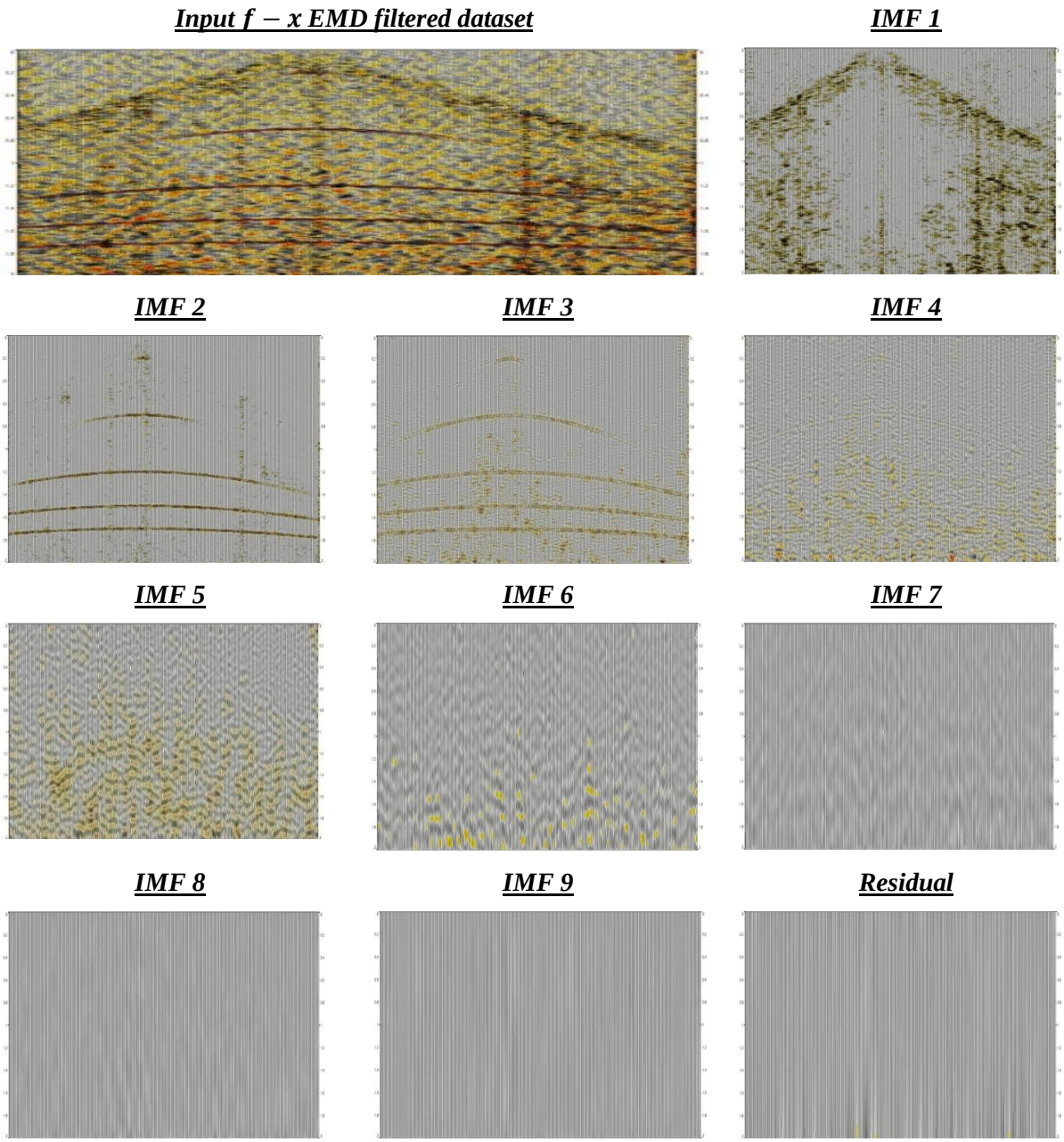

Figure 7.9: *IMFs obtained after $t-x$ trace-by-trace EEMD applied to filtered data.*

Only in IMF 4 a small mix between signal and noise can be observed. The final filtered result was obtained by subtracting the noisy IMFs (1, 5-9) plus the residual from the $f-x$ EMD filtered result (cf. Fig. 7.10).

$f-x$ EMD filtered result

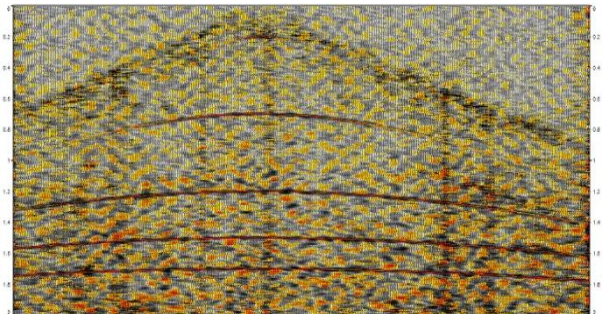

Final filtered section

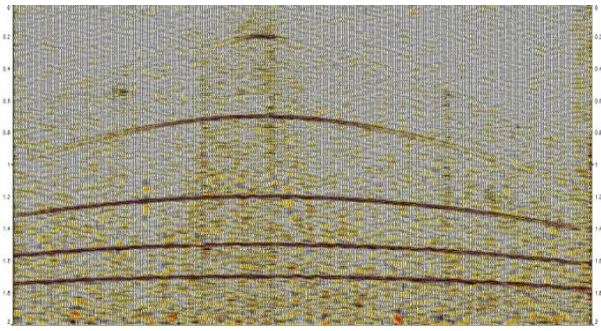

Residual

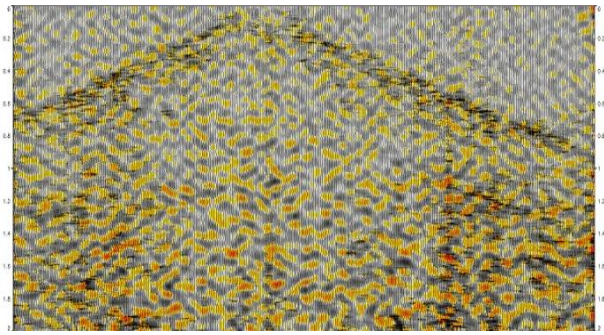

Figure 7.10: *Input, output and difference data obtained using $t-x$ EEMD (trace-by-trace).*

Figure 7.11 shows RMS amplitude of the noise-free synthetic, ground roll noise and both of the filtered sections ($f-x$ EMD alone or in combination with $t-x$ EEMD).

Clearly, using a combination of EMD filtering techniques leads to better noise attenuation than using each of them separately. Some artificial end effects caused by spline interpolation as described in Chapter 4 are present in the filtered section. Therefore, tapering of each side of the input dataset is considered an effective solution for reducing the EMD end effects.

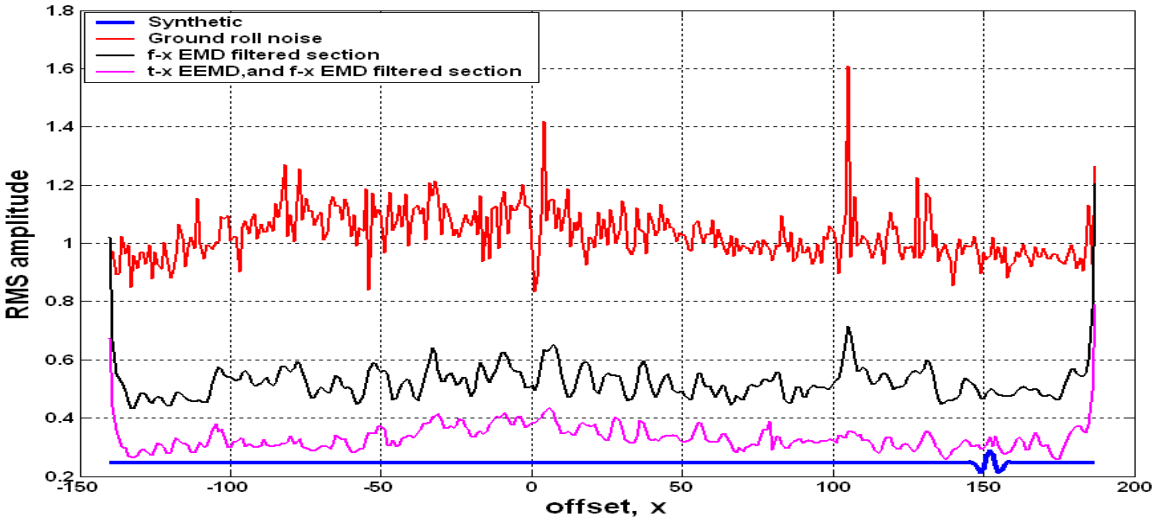

Figure 7.11: *The RMS amplitude of the synthetic model, ground roll noise, $f-x$ EMD filtered section, and $t-x$ EEMD (trace-by-trace) filtered section.*

7.2.2 Real dataset with linear interference noise

I now consider three marine shot records containing some swell noise and linear interference noise. The swell noise was attenuated using the SPARC module to improve the frequency content of each trace. I applied NMO correction to make the reflected events flat. Muting was also applied to remove the NMO stretch and improve the frequency content of each trace (cf. Fig. 7.12). The frequency-space EEMD technique was applied to this dataset using noise with standard deviation of 30% and 10 ensembles. A total of 8 IMFs plus residual were generated (cf. Fig. 7.13). IMF 1 captures most of the linear dipping events and high frequency noise while IMF 2 reveals some opposite dipping events that were not visible in the input data. IMFs 3-5 carry residual amounts of the dipping events and the remaining IMFs 6-8 carry small amounts of the flat reflected events. Most of the flat reflected events are present in the residual since they map to constant harmonics in the $f-x$ domain, where EEMD sees them as DC values.

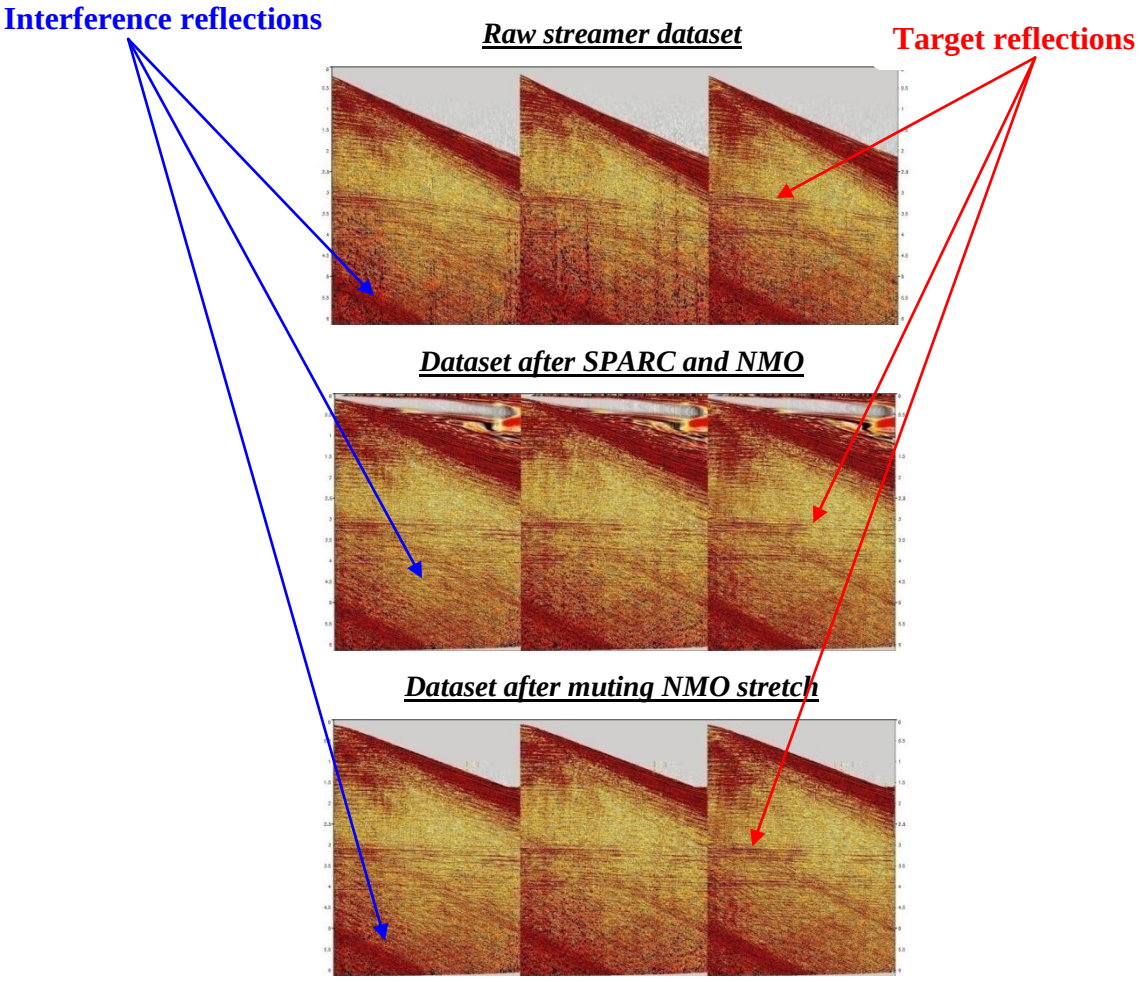

Figure 7.12: *Real dataset with linear interference noise.*

The produced IMFs can be classified in two categories:

- IMFs 1-5 carry the linear interference noise.
- IMFs 6-8 and residual carry the target reflections with small amounts of the remaining linear refracted events.

The improvement of the $f-x$ EEMD over the $t-x$ (trace-by-trace) EEMD is due to the decomposition of a superposition of harmonics as a function of space. Thus the EEMD decomposes the superposition of harmonics in a dyadic fashion that can lead to improvements in the transition IMFs when the IMFs transfer back to the $t-x$ domain.

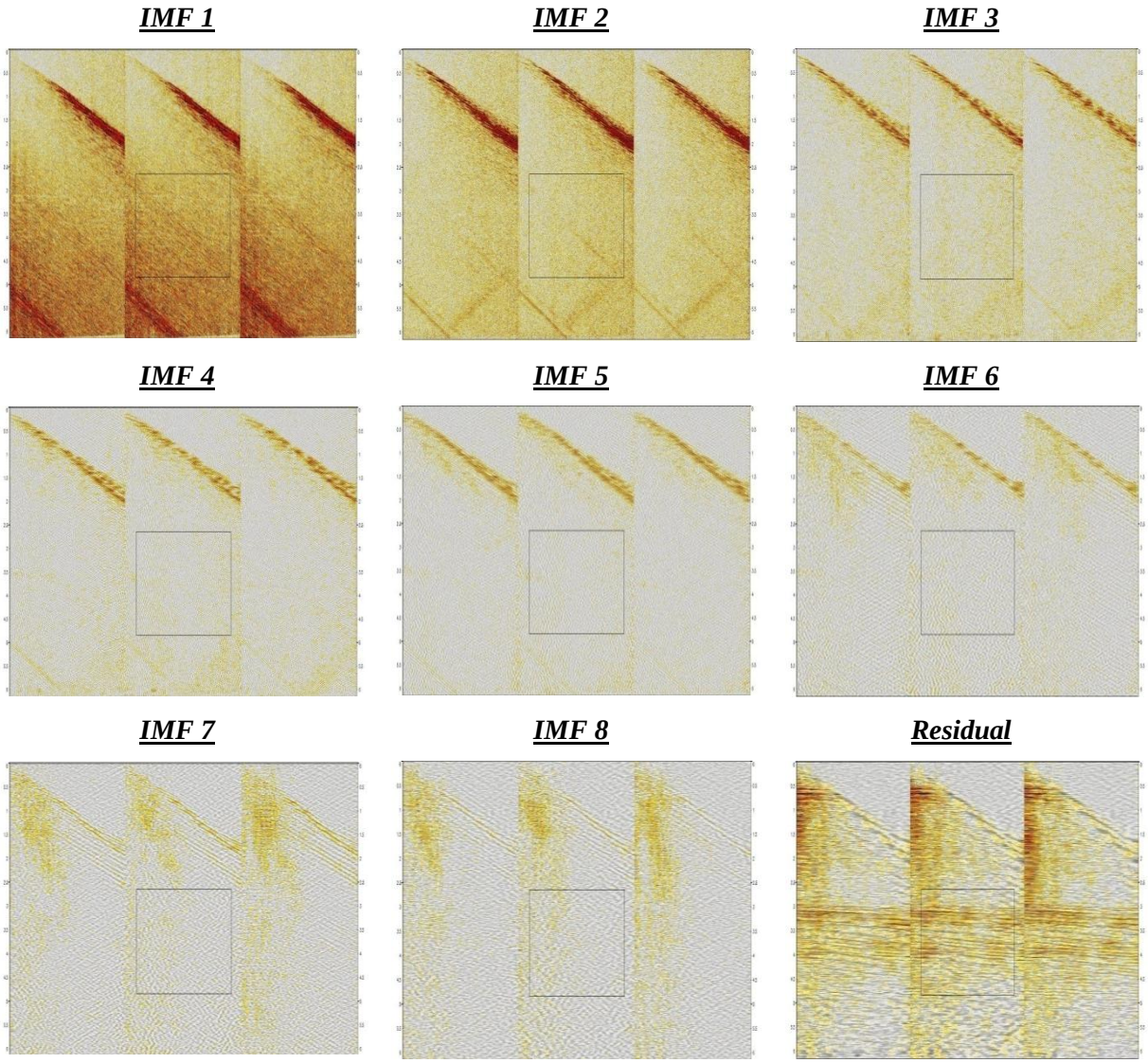

Figure 7.13: *IMFs resulting from $f-x$ EEMD.*

Figure 7.14 shows the amplitude spectrum in dB of each IMF within selected windows in Fig. 7.13. The behavior as a dyadic filter bank with overlapping frequency spectra is not clearly visible in the IMFs because the nature of $f-x$ EEMD depends on the variation from trace to trace in the space domain. IMFs 1-3 mimic a high pass filter pattern and carry most of the random and steeply dipping coherent noise that map into the fastest oscillating harmonics in the $f-x$ domain while the last IMFs and residual carry the slowest oscillating and flat harmonics produced by target reflections.

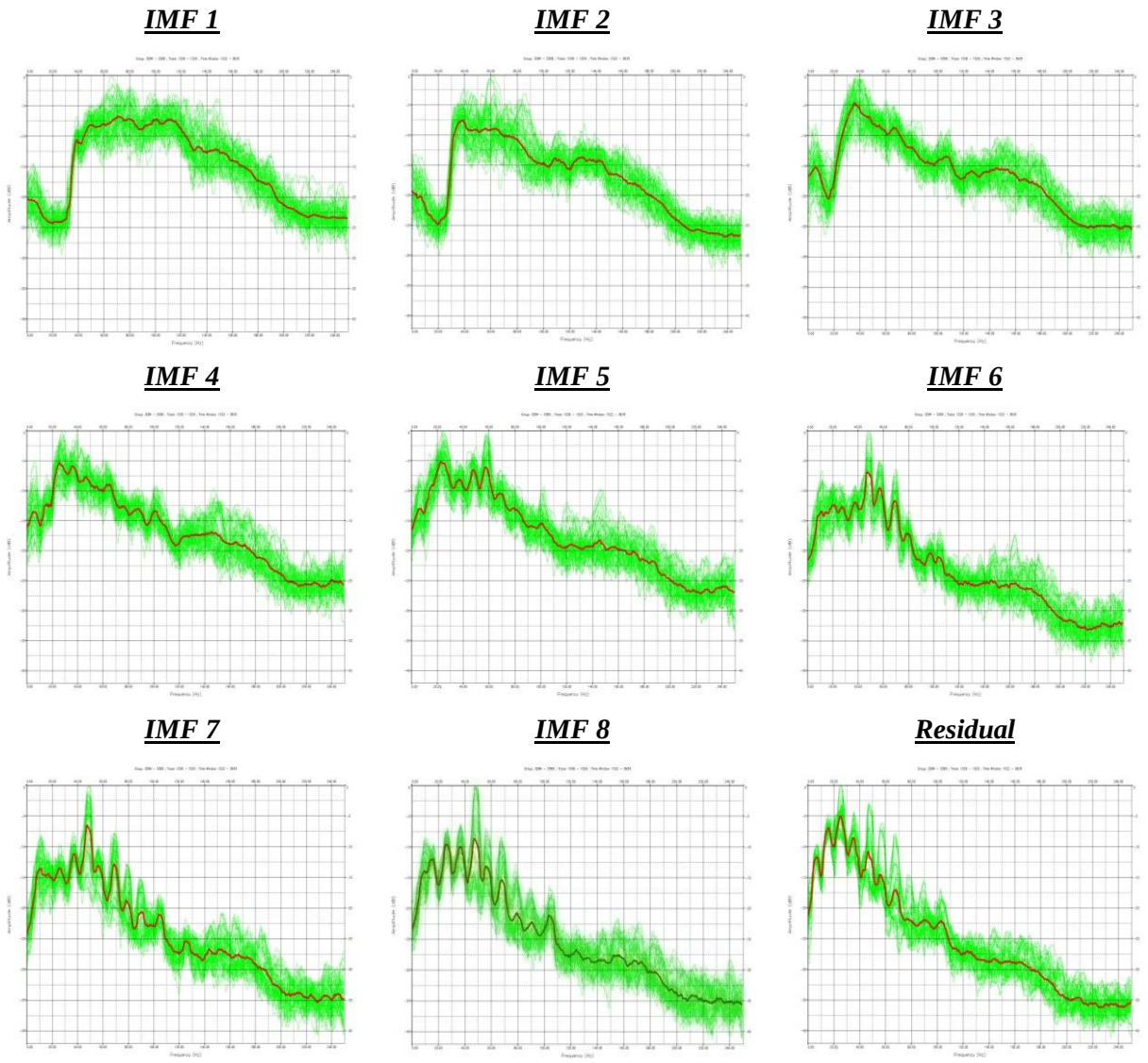

Figure 7.14: *Amplitude spectrum within a selected window in Fig. 7.13 (same scale has been used for all plots).*

Figure 7.15 shows signal and noise RMS amplitude (red line corresponds to signal and blue line corresponds to noise) for the computed IMFs within a selected window (cf. Fig. 7.13). The noise power is the highest in IMFs 1-3 and decreases in IMFs 4-6; it is very low in IMFs 7-8 plus residual. The signal RMS amplitude increases from IMF 1 to the residual that carries most of the flat target reflections. Thus the signal-to-noise ratio improves from IMF 1 to IMF 8 and the residual has the highest SNR.

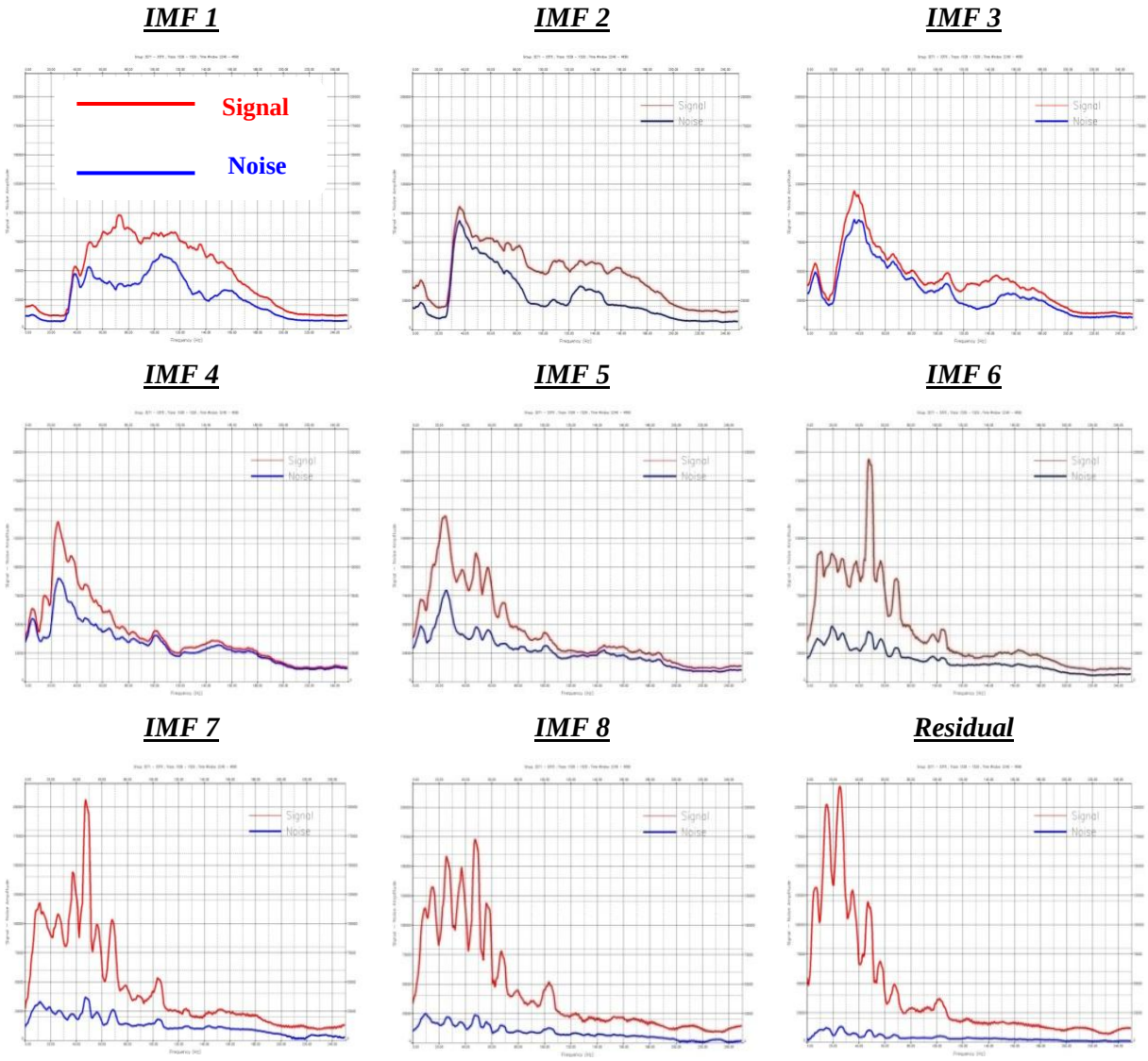

Figure 7.15: *Signal and noise RMS amplitude within a selected window in Fig. 7.13 (same scale has been used for all plots).*

The linear dipping events can now be removed based on the SNR ratio and visible inspection of each IMF. I suggest two filtered results: the first one is to sum the last four IMFs and residual (cf. Fig. 7.16), and the second one is to sum the last three IMFs and residual. From comparison of their difference sections both approaches seem to give similar results when it comes to improvement in SNR (cf. Fig. 7.16).

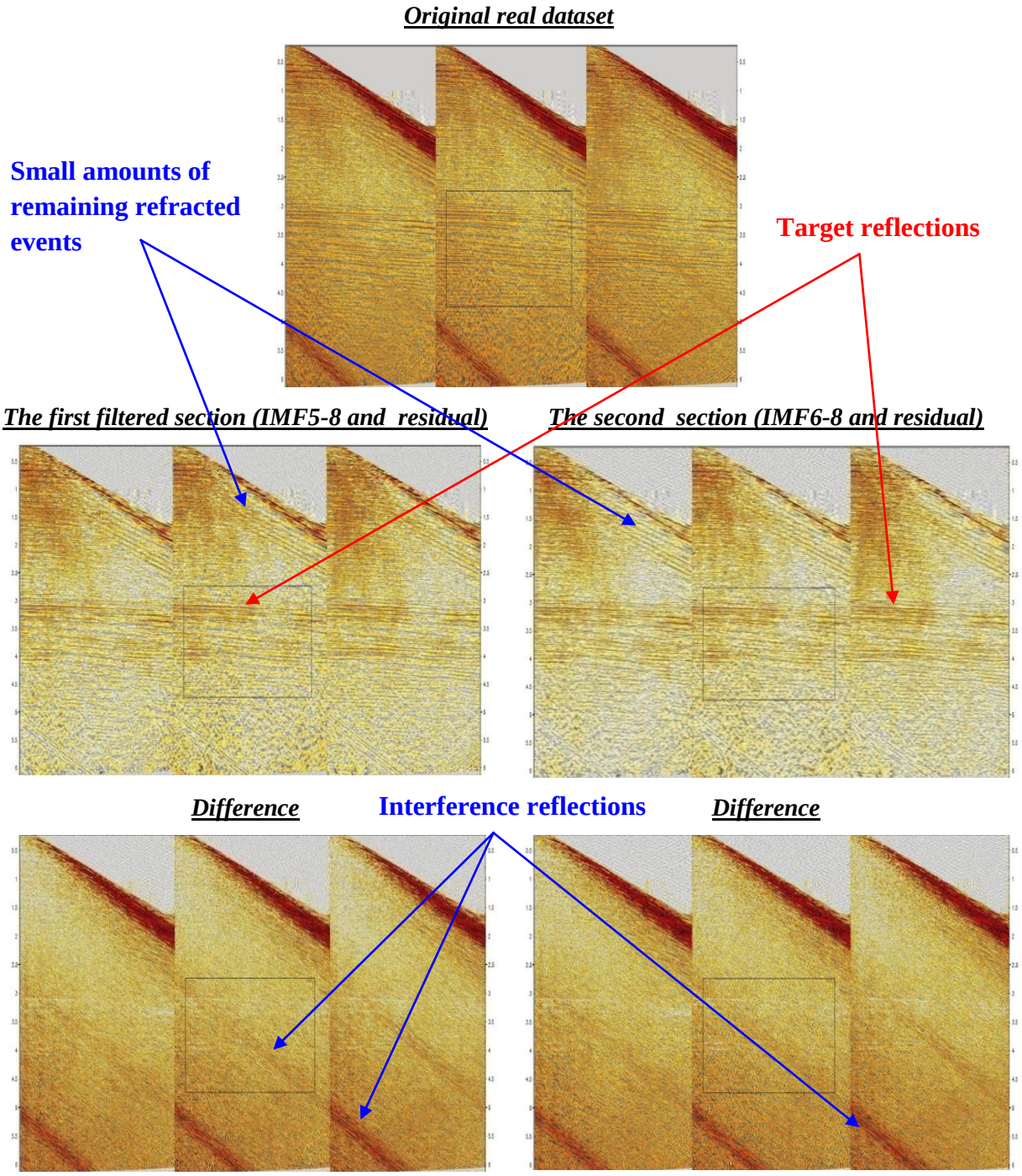

Figure 7.16: *$f-x$ EEMD filtered results of raw streamer dataset.*

Closer inspection of the difference sections shows no sign of signal leakage in the attenuated part of the dataset (cf. Fig. 7.16). Figure 7.17 shows the signal and noise RMS amplitude for each input dataset, the two filtered data results, and the difference data.

It is important to realize that the signal RMS amplitude in the filtered results show the same shape as for the input signal, where as the noise RMS amplitude in the removed parts has a similar shape as in the input noise. This indicates that $f - x$ EEMD filtering captures most of the noise present in the input dataset, and increases the signal to noise ratio correspondingly.

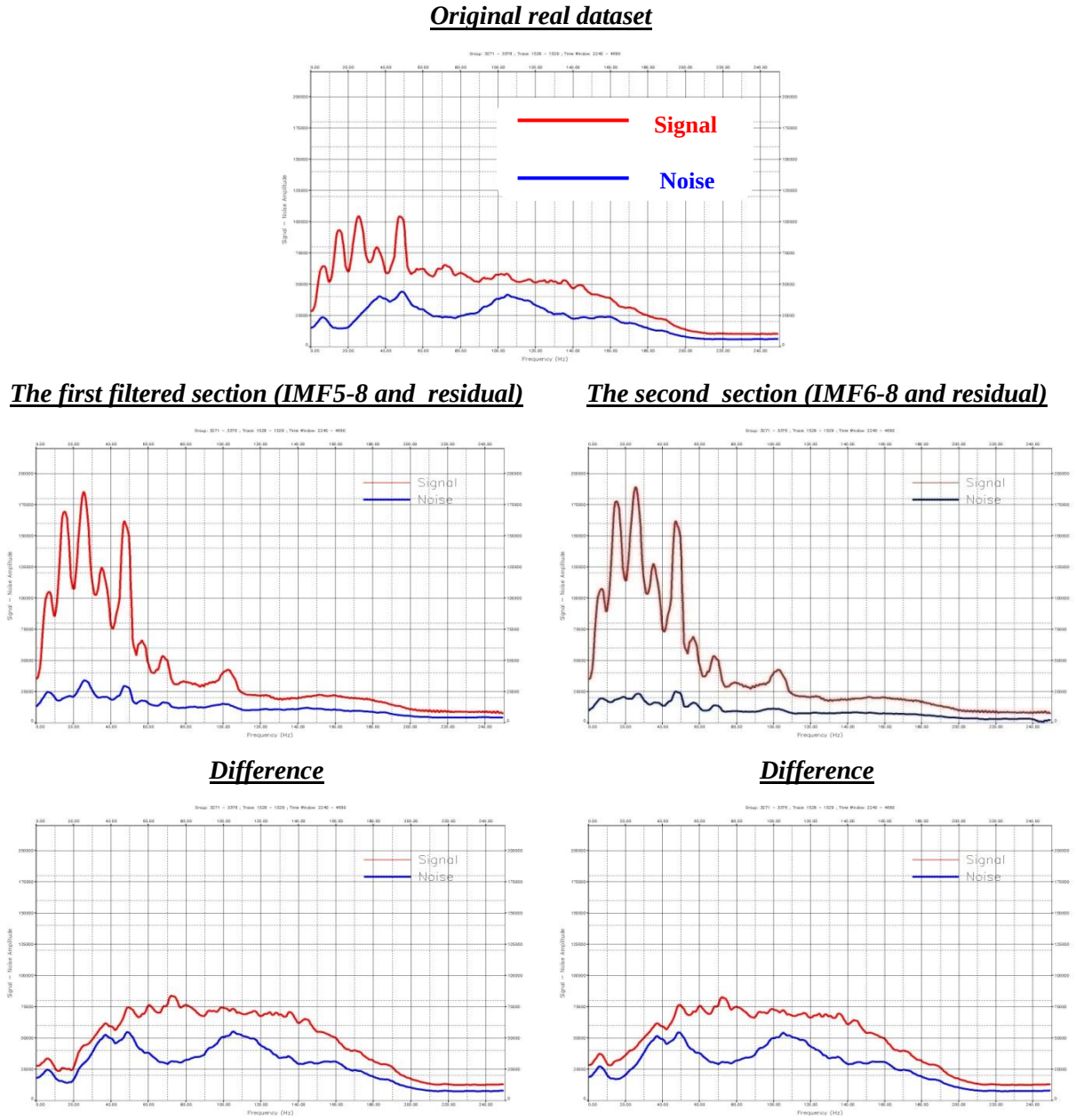

Figure 7.17: *SNR within a selected window in Fig. 7.16.*

7.2.3 Real dataset associated with Ground Roll and refracted events

In this section I consider a real dataset originating from an Ocean Bottom Cable (OBC) acquisition. It consisted of three common-receiver gathers and contains some interesting noise features such as linear coherent dipping events, shallow backscattering, ground roll, some shear events and high-frequency random noise (cf. Fig. 7.18) (no NMO has been applied).

I apply the frequency-space EEMD technique to the data to attenuate the noise and enhance the target reflections. A total of 10 IMFs plus residual were generated and noise with a standard deviation of 30% and 10 ensembles were employed (cf. Fig. 7.18).

Inspection of the first IMF shows that it carries the high frequency noise, most of the refracted events and the reflected interference noise as well.

The second and third IMFs carry the remaining parts of the ground rolls as well as some interference noise and refracted events. The fourth IMF carries very small parts of the target reflections besides smaller amount of ground roll. IMFs 5-9 and residual carry the target reflections with some remaining of refracted events. The $f-x$ EEMD has reduced the transition IMFs that was a major problem in $t-x$ (trace-by-trace) EMD/EEMD because the superposition of harmonics does not vary strongly with space.

Figure 7.19 shows the amplitude spectra of the original data and the computed IMFs for selected traces within a window (cf. Fig. 7.18); again we notice that the dyadic filter bank behavior observed in $t-x$ methods is no longer an issue with $f-x$ methods. This minimizes transition IMFs commonly present in $t-x$ (trace-by-trace) EMD and reflects the advantages of using $f-x$ EEMD for de-noising seismic data.

Figure 7.20 shows the SNR, as expected the first IMFs have low SNR compared to the last IMFs, therefore, removing the first three to four IMFS will attenuate most of the random and steeply dipping coherent noise such as reflected interference, ground roll and refracted events.

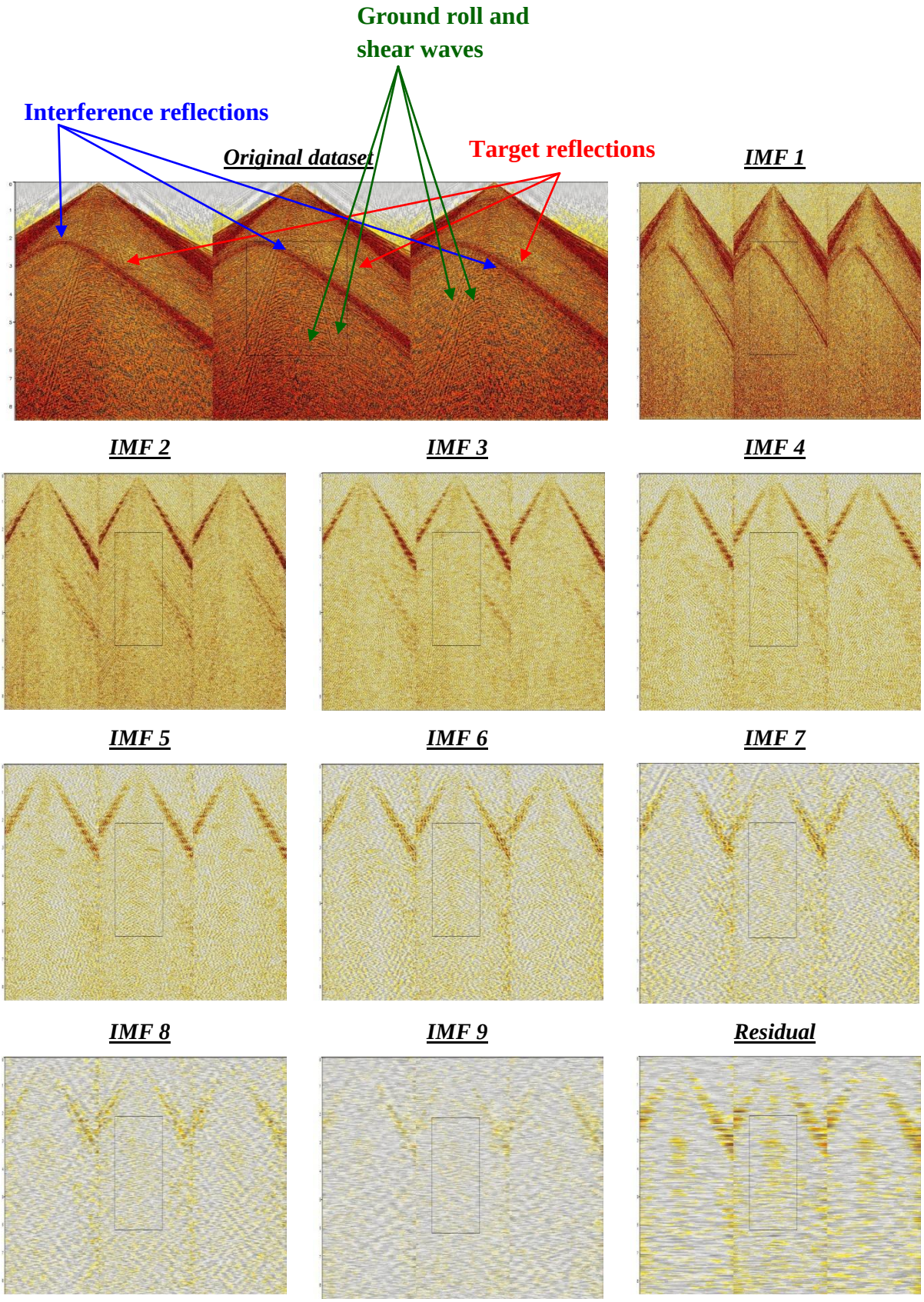

Figure 7.18: *IMFs resulting from $f - x$ EEMD.*

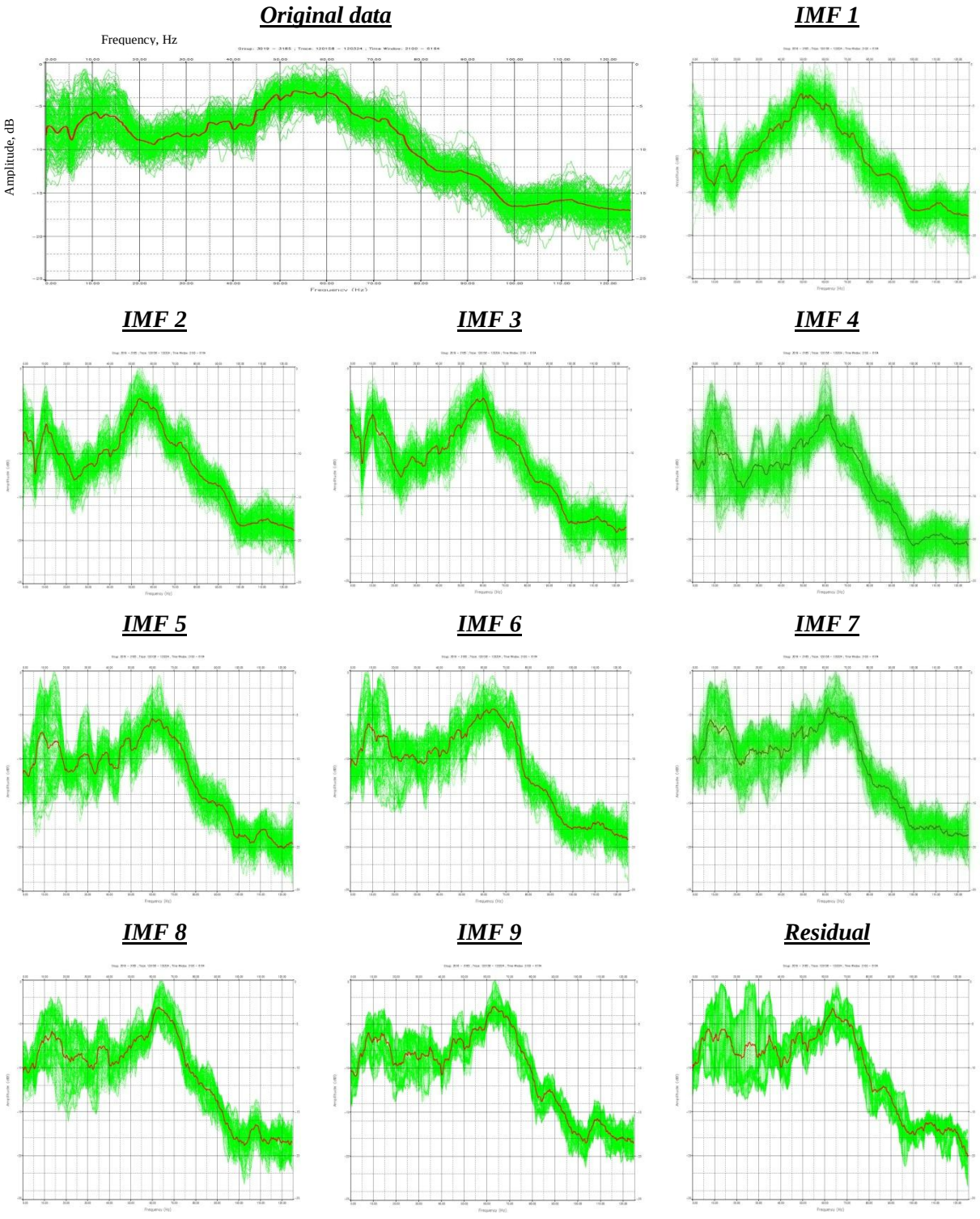

Figure 7.19: *Amplitude spectra within a selected window in Fig. 7.18 (same scale has been used for all plots).*

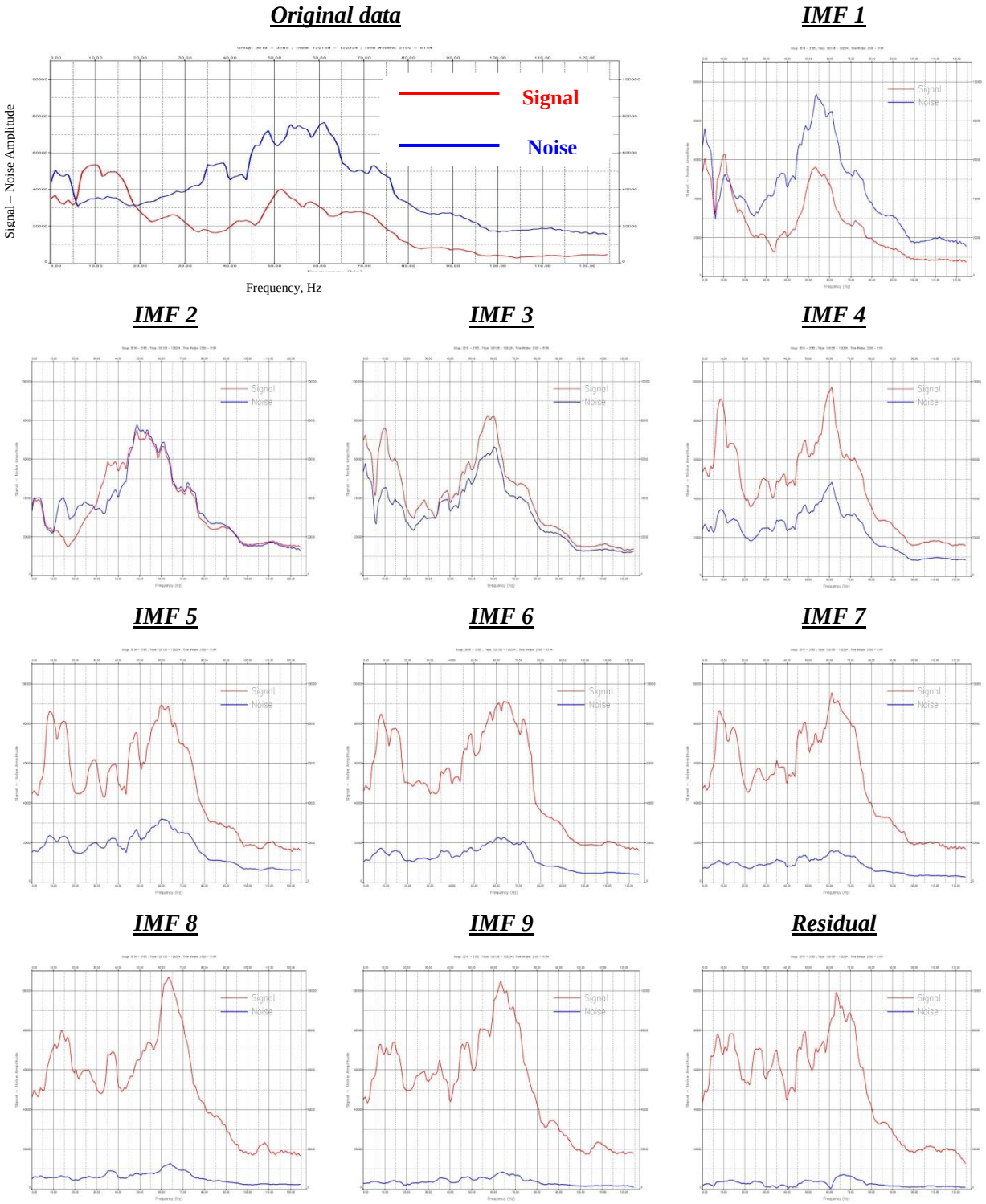

Figure 7.20: *Signal and noise RMS amplitude within a selected window in Fig. 7.18 (same scale has been used for all plots).*

A filtered section is now obtained by removing the first three IMFs that do not carry any part of the target reflections from the dataset. This section enhances the target reflections but still shows small remaining amounts of linear interference noise and ground roll (cf. Fig. 7.21).

I compute a second filtered section by also removing the first four IMFs. This attenuates more linear noise, but also smaller parts of the target reflections. Inspection of both $f-x$ EEMD filtered sections show that the target reflectors have been enhanced and the SNR of the dataset has been increased (cf. Fig. 7.21).

For comparison I filtered the dataset with CGGVeritas' Radon domain module RAMUR to attenuate interference noise. Inspection of the filtered sections show that most of the interference noise has been removed, while some of the linear coherent energy such as ground rolls, and refracted events have been left in the filtered section (cf. Fig. 7.21).

Comparison between the filtered results with the RAMUR result, demonstrate that $f-x$ EEMD leads to better attenuation of the linear interference noise and enhances target reflections. However, residual amounts of interference noise and more complicated shear waves are still present.

A key problem I noticed in handling the interference noise present in this particular dataset was that the EEMD filter passed the top of the interference noise since it is a flat event in the $t-x$ domain.

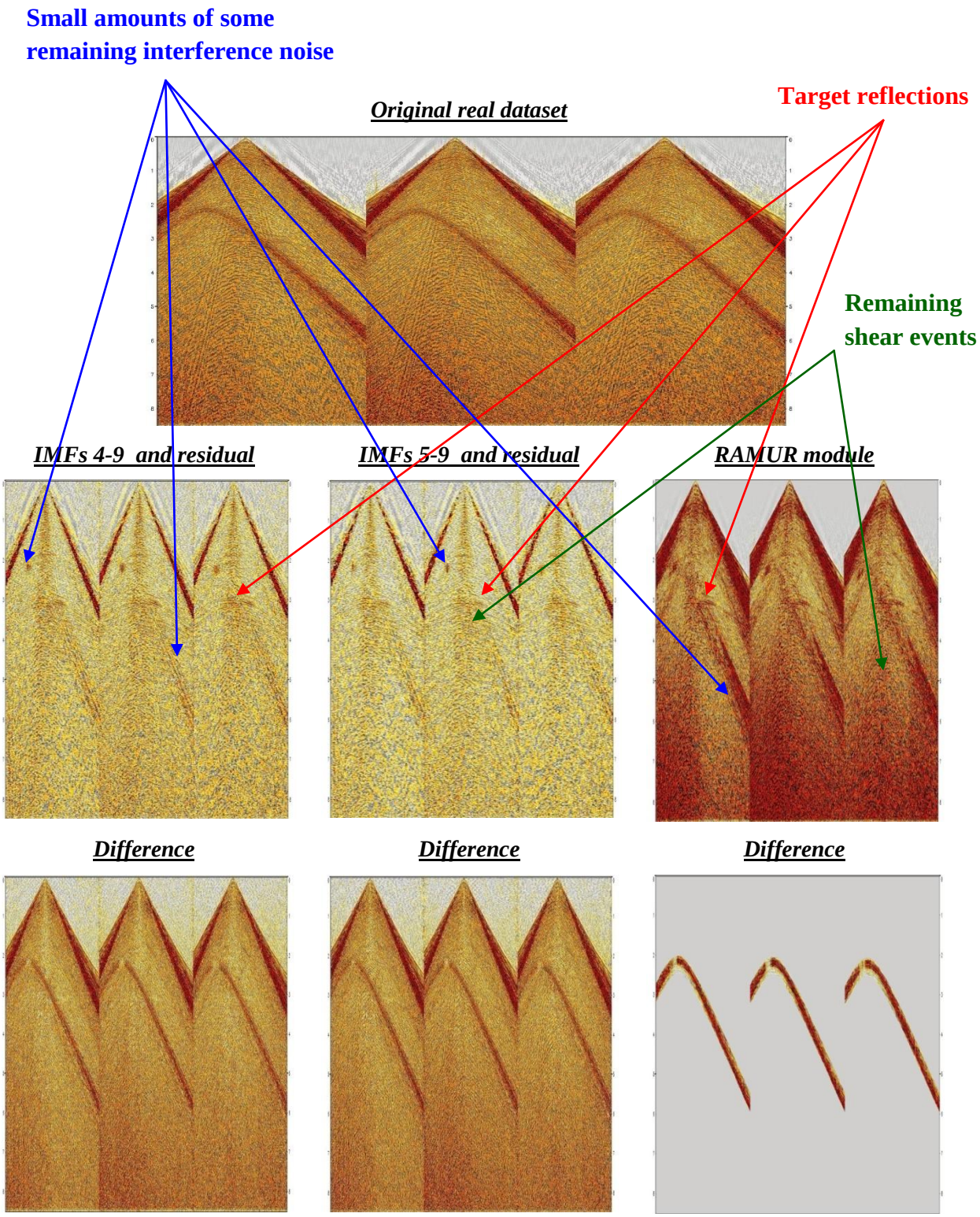

Figure 7.21: *$f-x$ EEMD and RAMUR filtered results*

7.3 Discussion

I have demonstrated that if gather data are NMO corrected before applying the $f-x$ EEMD technique, a better result can be obtained when it comes to separation between signal and noise. The reason is that the signal part will be close to a DC contribution and correspondingly be decomposed as the residual.

The major advantage of using the $f-x$ decomposition over the $t-x$ decomposition is that the transition IMFs and spectral leaks are drastically reduced because the dyadic filter bank behavior is not present in each trace of the generated IMFs. Thus, $f-x$ EEMD leads to a better separation between the signal and noise in the seismic data.

However, there are some disadvantages when working in the $f-x$ domain:

- The computational time is not so efficient in the $f-x$ domain compared to the $t-x$ domain, because the composition has to be carried out twice (i.e. real and imaginary components).
- The EMD/EEMD $f-x$ filtering techniques are sensitive to the frequency content of each trace which could result in some low frequency/high amplitude artificial noise in the filtered section. These artificial effects can be removed by either editing the bad traces before using the EEMD $f-x$ technique or by using the trace by trace EEMD $t-x$ filtering technique (cf. Chapter 6). Probably for this reason Bekara and van der Baan (2009) did not address the swell noise in their publication.
- Not all unwanted linear dipping events have been attenuated because some of these events will mix with the target reflections in the same IMF.
- The EEMD $f-x$ filtering technique is sensitive to the trace spacing (spatial sampling) which is determined by the spline interpolation. This can lead to some problems in the computed IMFs since the interpolation greatly reduces the need for regular sample intervals (Bekara and van der Baan, 2009). Further investigation is needed and is beyond the scope of this thesis.

8. DE-NOISING OF SEISMIC DATA BY USING EMD ON CONSTANT TIME SLICES

8.1 Introduction

Some of the disadvantages of using both Battista's (2007) and Bekara's (2009) techniques have been addressed in Chapters 6 and 7.

It is difficult for EMD to identify the seismic energy by decomposing trace-by-trace in the $t-x$ domain especially when the signal and noise bandwidths overlap because the EMD acts like a filter bank and corresponds to signal-dependent, time-variant filtering. The computed IMFs will suffer from the mixing mode problem between the seismic signal and the seismic noise (cf. Chapter 6).

Most of the available filtering techniques, such as the Radon transform and the $f-x$ deconvolution make use of coherency present in the seismic events either in the $t-x$ or $f-x$ domain. Developing a new filtering approach based on $t-x$ EMD which target the reflected events based on their coherent properties is challenging. One possibility is to use the potential of EMD to extracting the trend of the input signal (cf. Chapter 4).

Only few references address applications of EMD to extract the signal trend (Suling et al. (2009), Zhou et al. (2008) and Flandrin et al. (2004)). However, no consensus exists about how to define trend, since trend definitions are related to the data peculiarities and fields of application. Flandrin et al. (2004) have investigated the potential and limitations of EMD based methods in de-trending, relating the trend to the statistical properties of the IMFs. Here trend is defined as the sum of the IMFs having non-zero mean. Application to heart-rate data illustrates the potential usefulness of de-trending, while Zhou et al. (2008) have proposed an

algorithm for removing trends from power-system oscillation data based on a slightly modified EMD.

The computed IMFs using Battista et al. (2007) methodology suffer most of the time from mixing modes, while computed IMFs using Bekara and van der Baan (2009) methodology always depend on the frequency content of each trace and takes longer processing time.

I suggest a new approach by combining the two ideas introduced by Battista et al. (2007) and Bekara and van der Bann (2009). A key to such a strategy is that the reflections have been NMO corrected so that they appear fully flat. In our case, trends definitions are therefore represented by the flat seismic. Extracting the trend is implemented in the $t - x$ domain using two steps:

- Applying EEMD to constant-time slices of the dataset
- Applying EEMD on the traces (i.e. trace by trace).

The first step is necessary to remove the high oscillation modes representing various types of noise. In this step, the unwanted noise occupies the first IMF(s) while the target reflections occupy the last IMF(s) and the residual. The first filtered section can be obtained by subtracting the first noisy IMF(s) from the original dataset.

The second step is needed only to remove any artificial low frequency/ high amplitude noise that have been carried by the last IMFs from the first step. The second filtered section can be obtained by removing the last IMF(s) and the residual from the first filtered section. The final filtered section will represent major noise attenuation and a significant reduction in the mixing mode problem.

As already stated, NMO correction should be carried out to flatten the target reflections to avoid any distortion of reflector amplitudes that can be caused by using the EMD.

Consider a flat seismic event in the $t - x$ domain (cf. Fig. 8.1a) with a constant amplitude value of 2 superimposed random low and high frequency noise (cf. Fig. 8.1b).

The cross-section plot in Fig 8.1c shows how the amplitude level varies along the horizontal slice indicated in Fig. 8.1b. It is obvious that the noise level has been shifted according to the mean amplitude level of the signal (here taken to be constant).

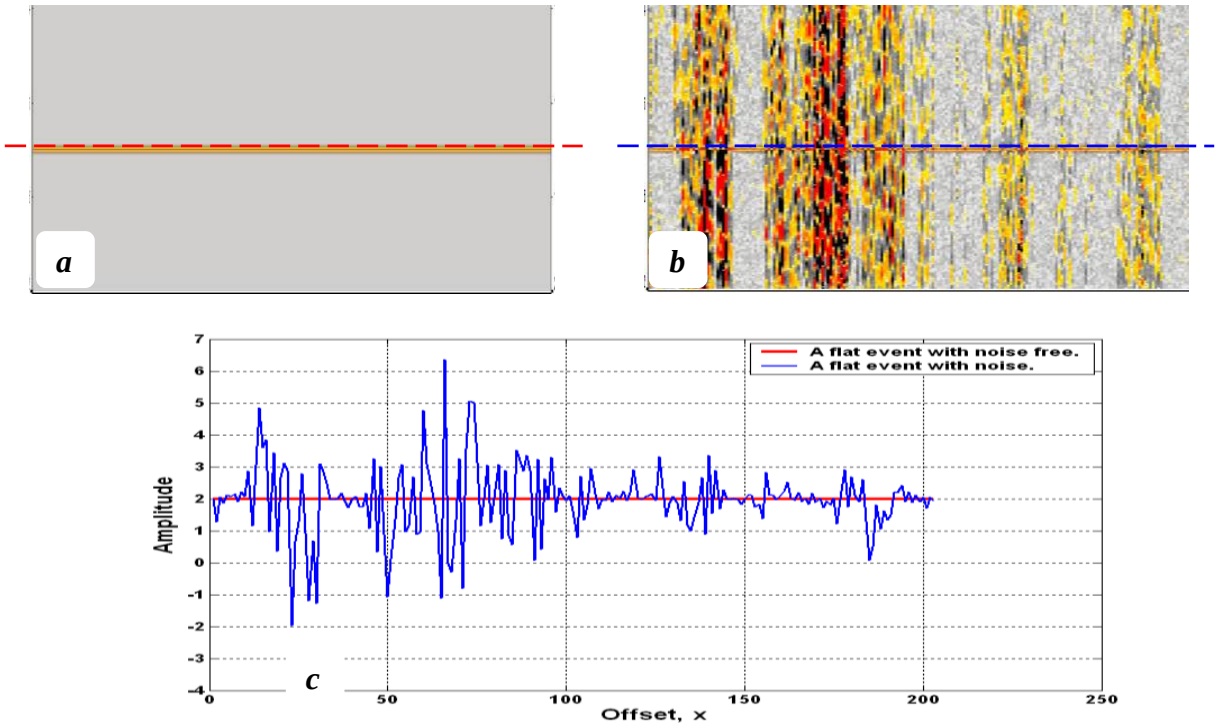

Figure 8.1: (a) *A flat noise free seismic event.* ***(b)*** *A flat seismic event with noise superimposed.* ***(c)*** *A cross-section plot.*

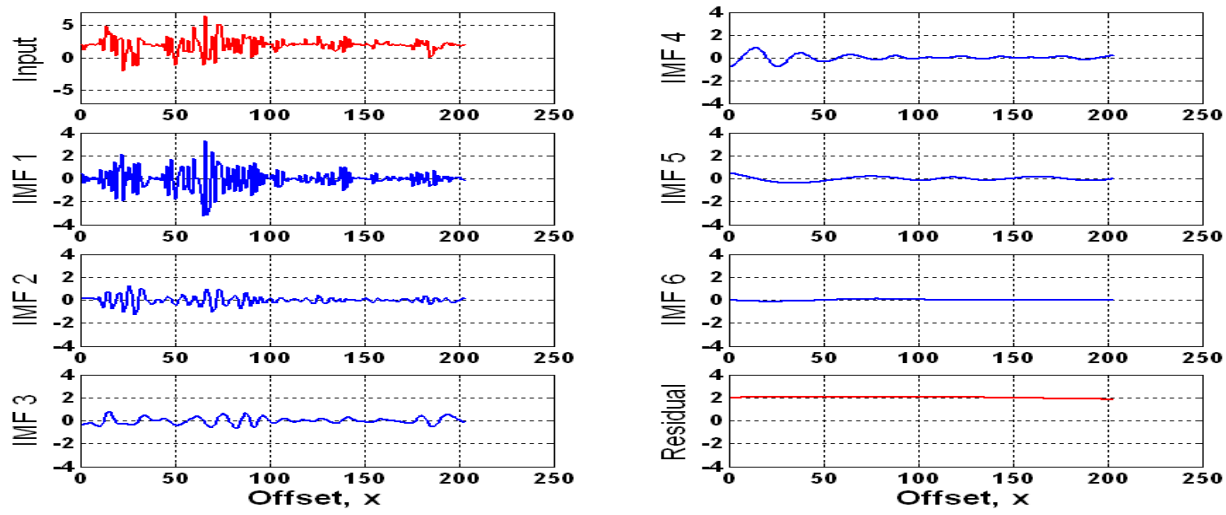

Figure 8.2: *Input signal, computing IMF(s) and residual.*

EEMD can be used to extract the dc values which represent the target seismic event (cf. Fig. 8.2). Clearly, the first four IMFs carry most of the noise while the sum of the residual and the last IMF(s) will give an accurate estimate of the mean amplitude level of the flat event.

8.2 Application to attenuate seismic noise

8.2.1 Synthetic data with swell noise

Real wide band noise including swell noise as shown in Figure 6.15b (Chapter 6) is added to the synthetic reflection model in Fig 6.7a that has the following interval velocities: 1500, 2000, 2500, 3000 and 3500 m/s. NMO corrections were carried out using the following velocity model simulating a small percentage of velocity errors (i.e. 1400, 1800, 2600, 1850 and 3700 m/s). After muting the stretch, I obtain the shot gather shown in Fig. 8.3b.

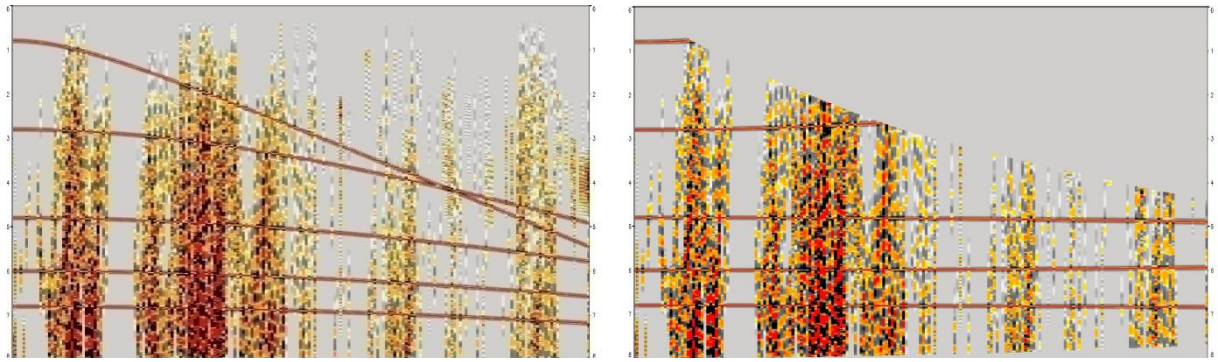

Figure 8.3: (a) *Synthetic shot gather with swell noise.* ***(b)*** *Shot gather after NMO correction and muting.*

To attenuate the noise, I apply EEMD to constant-time slices using a SD of 30% and 10 iterations. The output from EEMD is shown in Fig. 8.4. IMF 1 carries no reflected events but most of the noise present in the dataset.

IMF 2 carries the remaining noise plus parts of the first reflection. This is due to the fact that the first reflection is short of length due to muting and with virtually no noise in its vicinity.

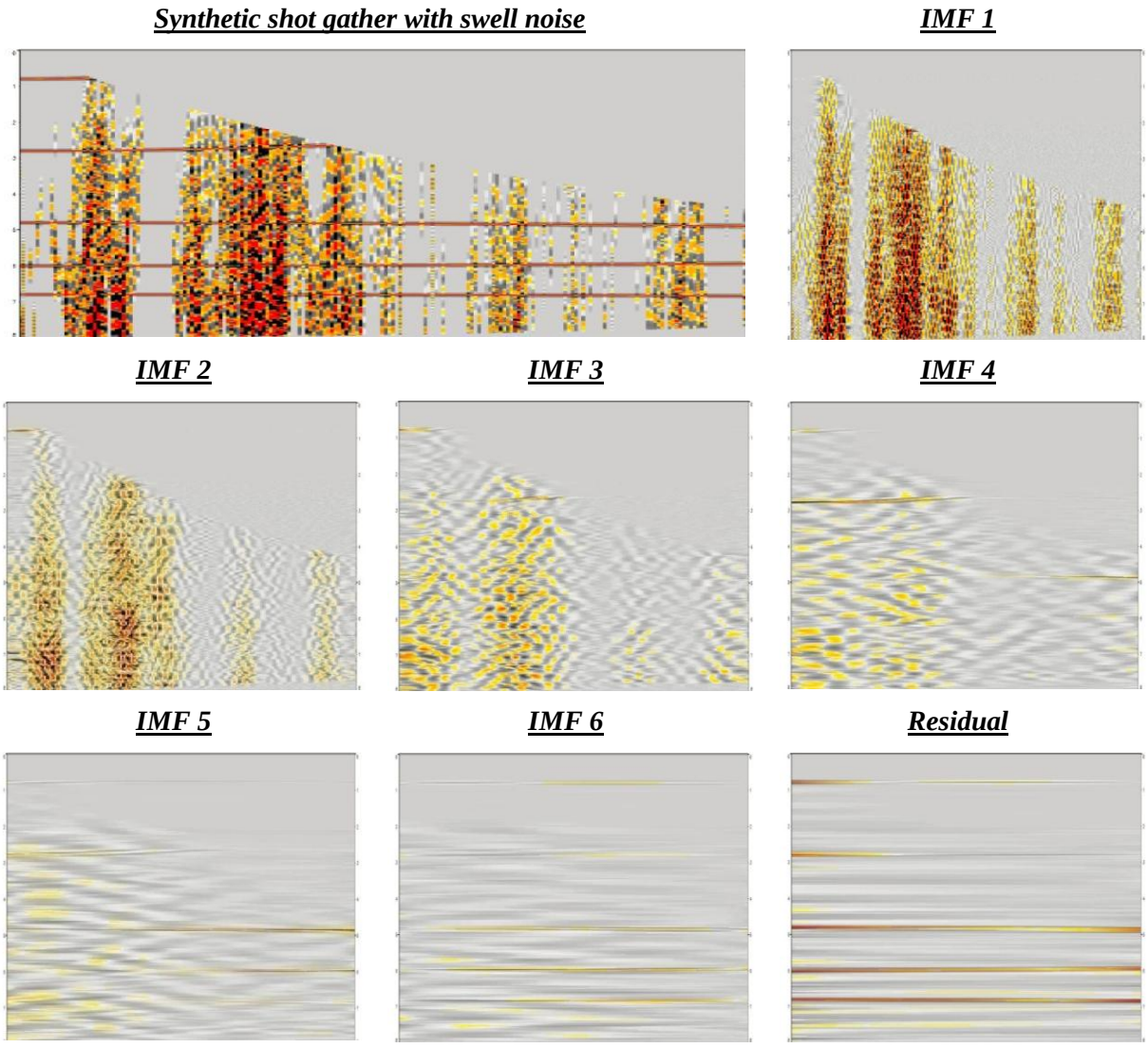

Figure 8.4: *Synthetic shot gather with swell noise and calculated IMFs by EEMD on constant-time slices.*

IMF 2 carries the mid range frequency band while IMFs 3-6 carry some of the reflected energy and high amplitude/low frequency noise. The residual, as expected, carries most of the flat seismic events.

I create a filtered section by removing IMFs 1 and 2 from the original dataset as shown in Fig. 8.5b. A small leakage of the first reflection can be observed in the removed noise (cf. fig. 8.5c) as discussed earlier.

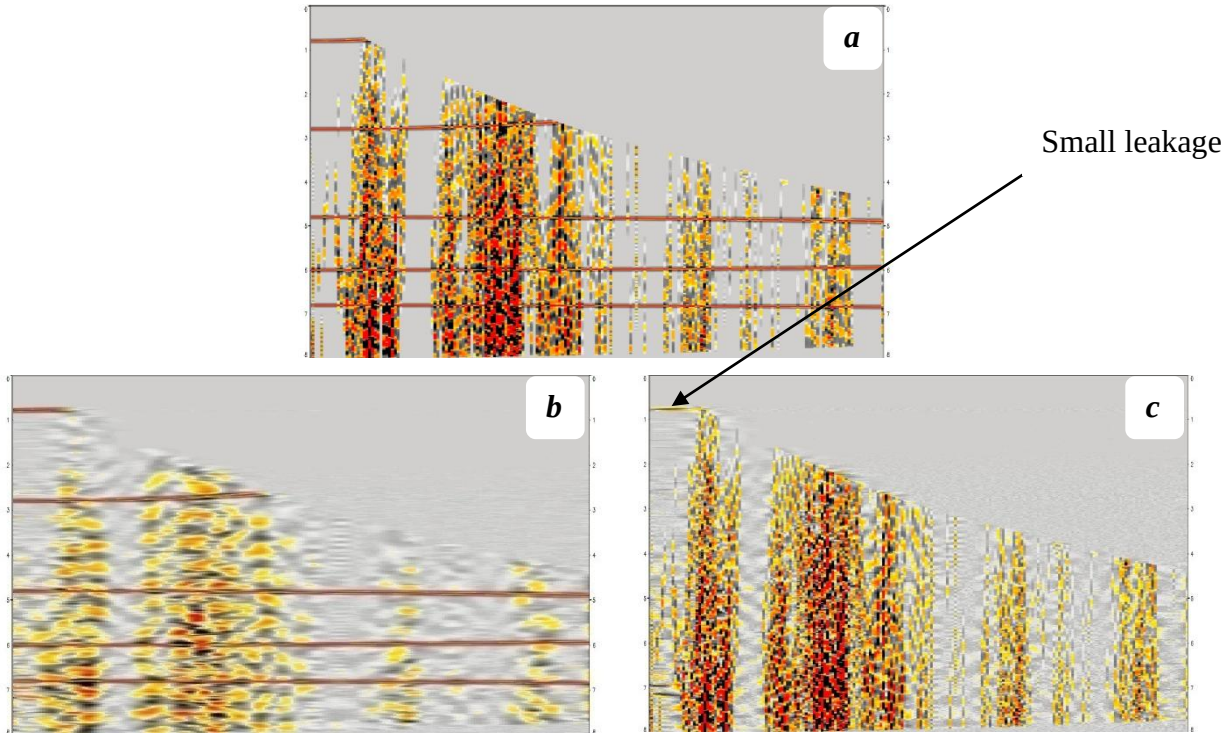

Figure 8.5: ***(a)*** *Original dataset.* ***(b)*** *After EEMD filtering using constant-window slices.* ***(c)*** *Associated difference (i.e. attenuated noise).*

To further attenuate noise, EEMD is applied trace by trace in the $t - x$ domain using a SD of 30% and 10 ensembles. EEMD produces 9 IMFs and a residual that shows a good separation between the remaining noise and the signal (cf. Fig. 8.6).

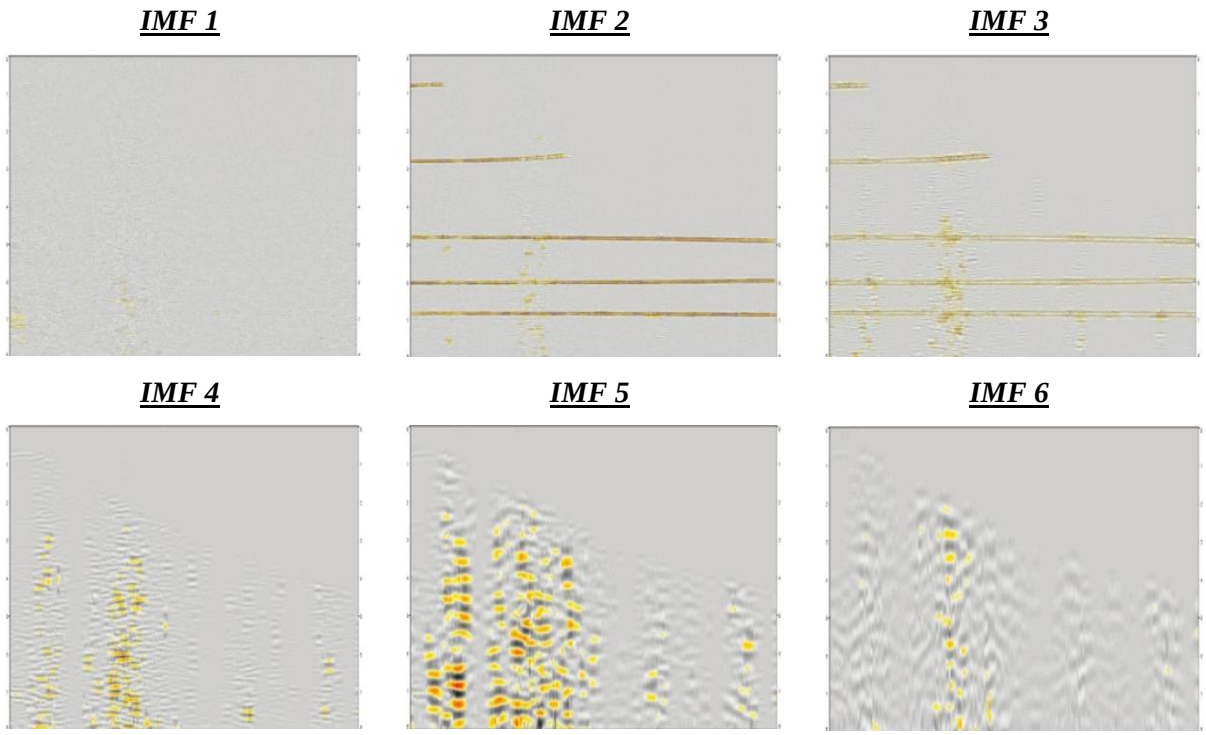

Figure 8.6: *Calculated IMFs by applying EEMD trace-by trace on the filtered EEMD data in Fig. 8.5b.*

The high frequency and low frequency/high amplitude noise can now be removed by keeping IMFs 2-3, and removing the rest of the IMFs from the input dataset. The final or second step filtered result shows that most of the noise has been attenuated and only small amounts of it falls in the signal band (cf. Fig. 8.7).

To check for any loss in the signal after applying the two step EEDM filtering approach, I compare the result with the NMO-corrected noise-free data (cf. Fig 8.7). Their difference demonstrates the efficiency of the two-step procedure with minimal signal leakage and low residual noise.

Input section to the trace-by-trace EEMD

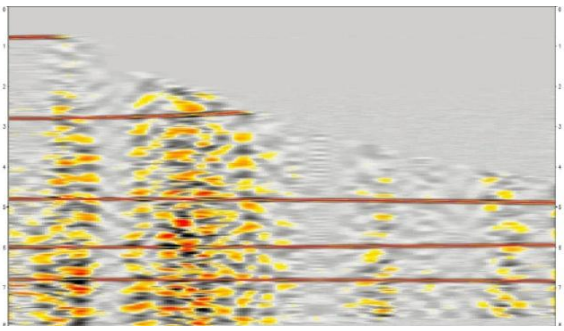

Final result of the $t-x$ EEMD

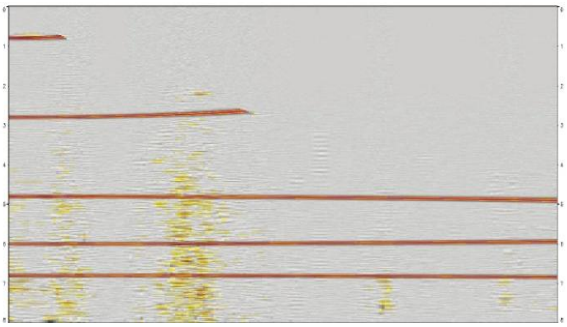

NMO corrected original noise-free synthetic

Difference section (attenuated noise)

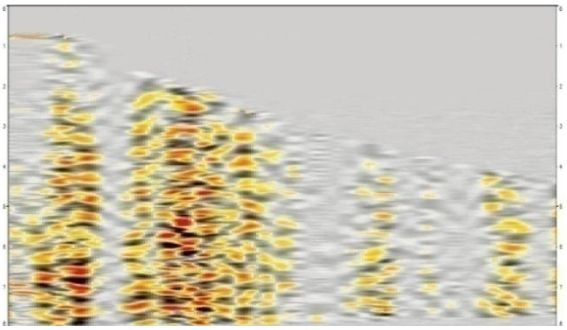

Difference between: Final result and NMO corrected original noise-free synthetic

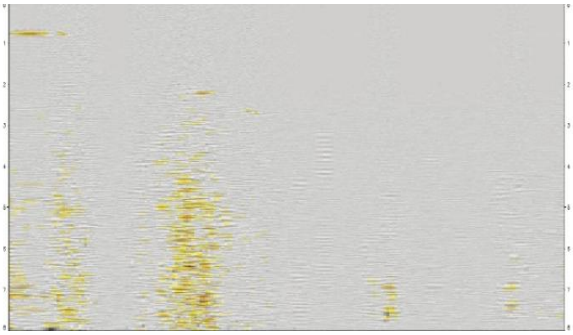

Figure 8.7: *Final filtered section compare to noise-free section.*

8.2.2 Real dataset with interference and swell noise

Next, I consider a real dataset consisting of three shot gathers. The same data has already been filtered employing $f-x$ EEMD as shown in Fig. 7.16. The dataset contains linear dipping events and swell noise. Now I apply EEMD within constant-time slices using a SD of 30% and 10 ensembles. A total of 8 IMFs plus residual were generated. IMF 1 carries most of the refracted events and interference noise present in the dataset (cf. Fig. 8.8).

IMFs 2-3 carry most of the swell noise and some parts of the interference noise and the refracted events.

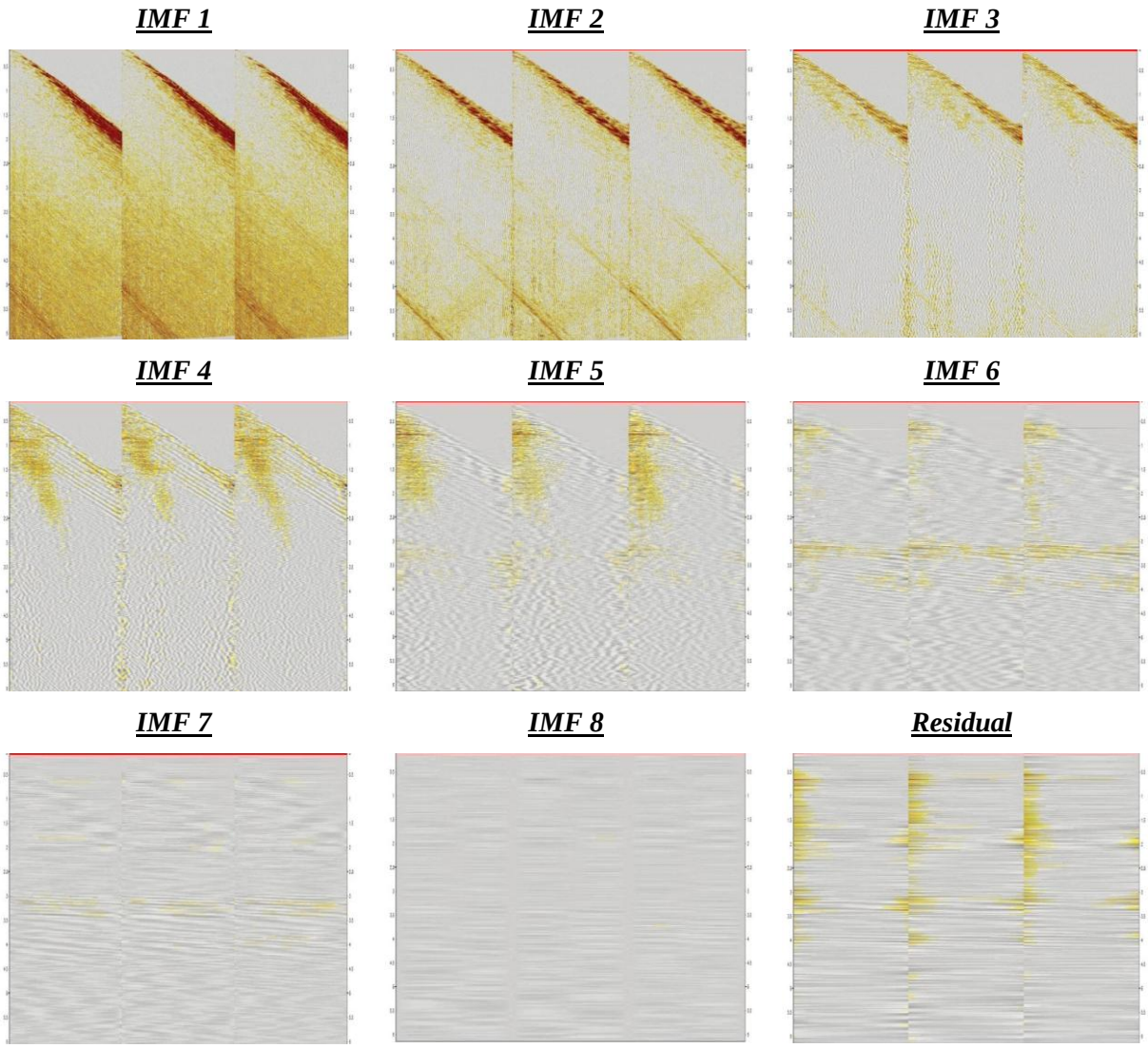

Figure 8.8: *The computed IMFs from EEMD when applied to constant-time slices.*

I construct a filtered section by removing the first three IMFs (i.e. IMFs 1- 3), that carry most of the target noise, from the original dataset (cf. Fig. 8.8). We see that most of the refracted events, interference and swell noise have been well attenuated. There is no leakage of energy from the target reflections; however, small amounts of leakage of the shallow reflections are present (cf. Fig. 8.9).

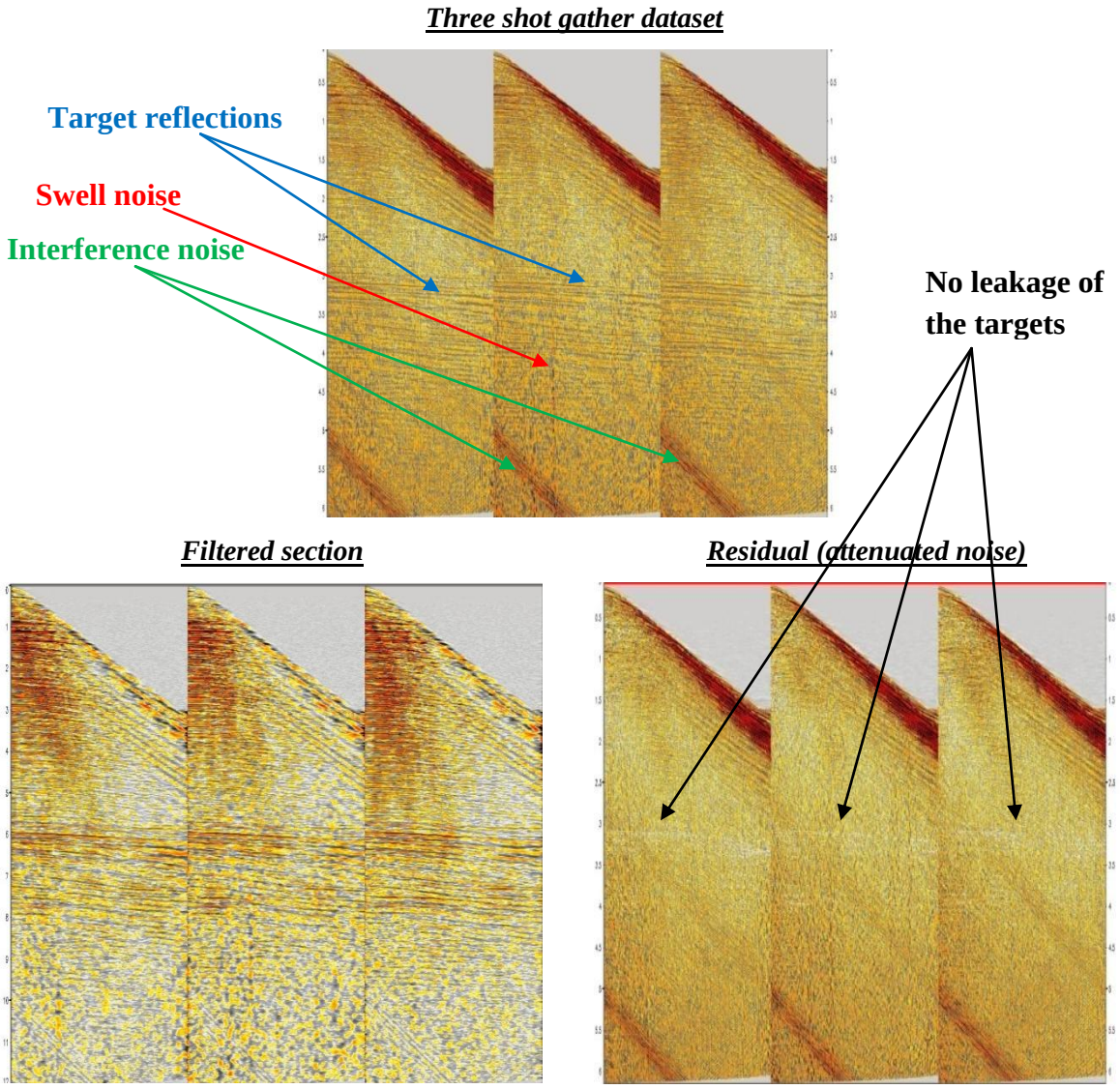

Figure 8.9: *Filtered section produced by EEMD technique on time-window slices.*

For further SNR enhancements and attenuation of the remaining high-amplitude low-frequency noise, I ran EEMD trace-by-trace on the filtered section in Fig 8.9. A total of nine IMFs and a residual were generated as shown in Fig. 8.10.

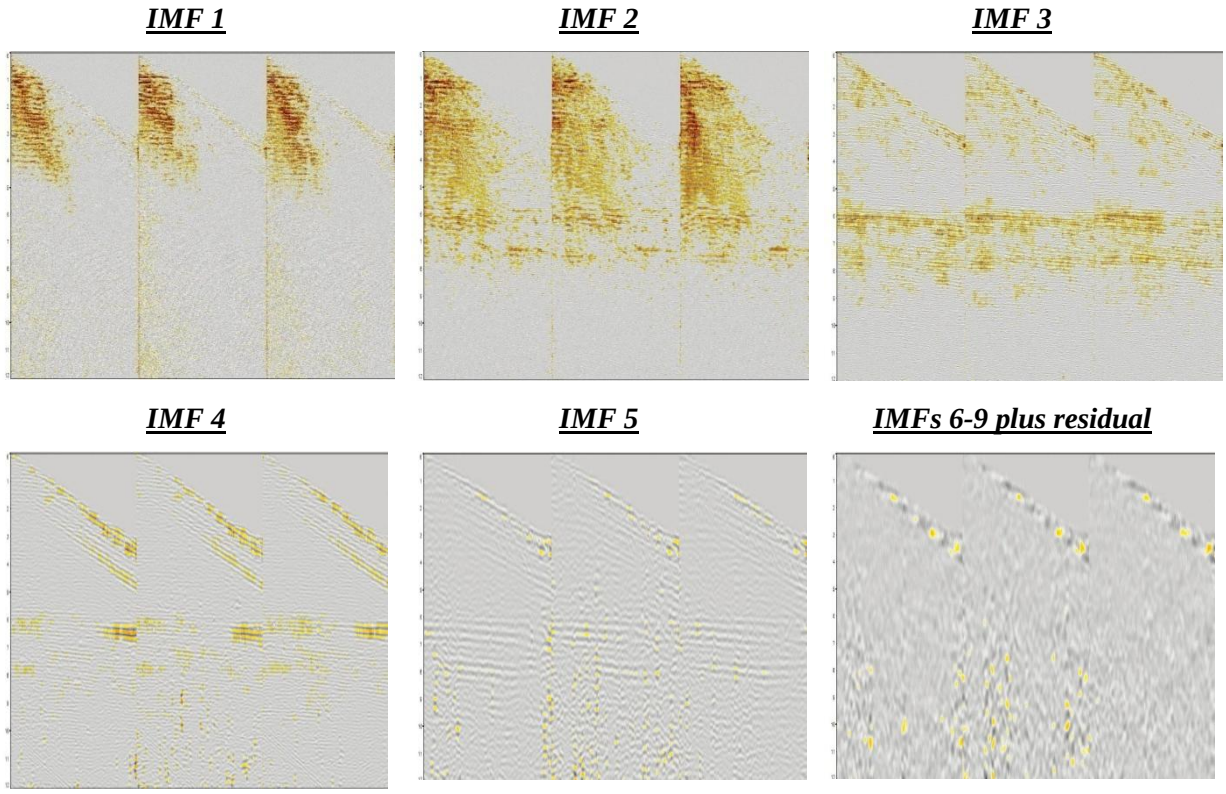

Figure 8.10: *The computed IMFs from trace-by-trace EEMD of the filtered section in Fig. 8.9.*

The final filtered section is obtained by removing the last four IMFs (i.e. 6-9) and residual from the input data. Figure 8.11 shows a small section of the second shot gather before and after trace-by-trace filtering.

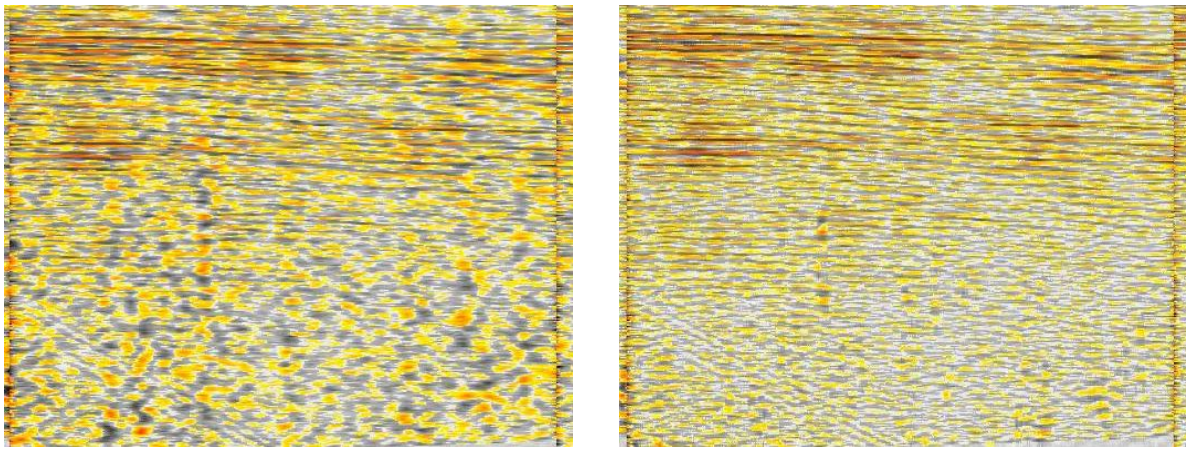

Figure 8.11: (Left) *before and* ***(Right)*** *after trace-by-trace EEMD filtering applied to the filtered EEMD (time-window slices) section.*

In Fig. 8.12 the corresponding filtered results obtained using the proposed two-step $t-x$ EEMD and $f-x$ EEMD (cf. Chapter 7) are shown together with the corresponding difference data.

Comparison between the two different approaches shows that they give similar results regarding target reflection enhancement. The time-slice approach seems to remove slightly more noise but at the expense of resolution. The technique is also computationally faster.

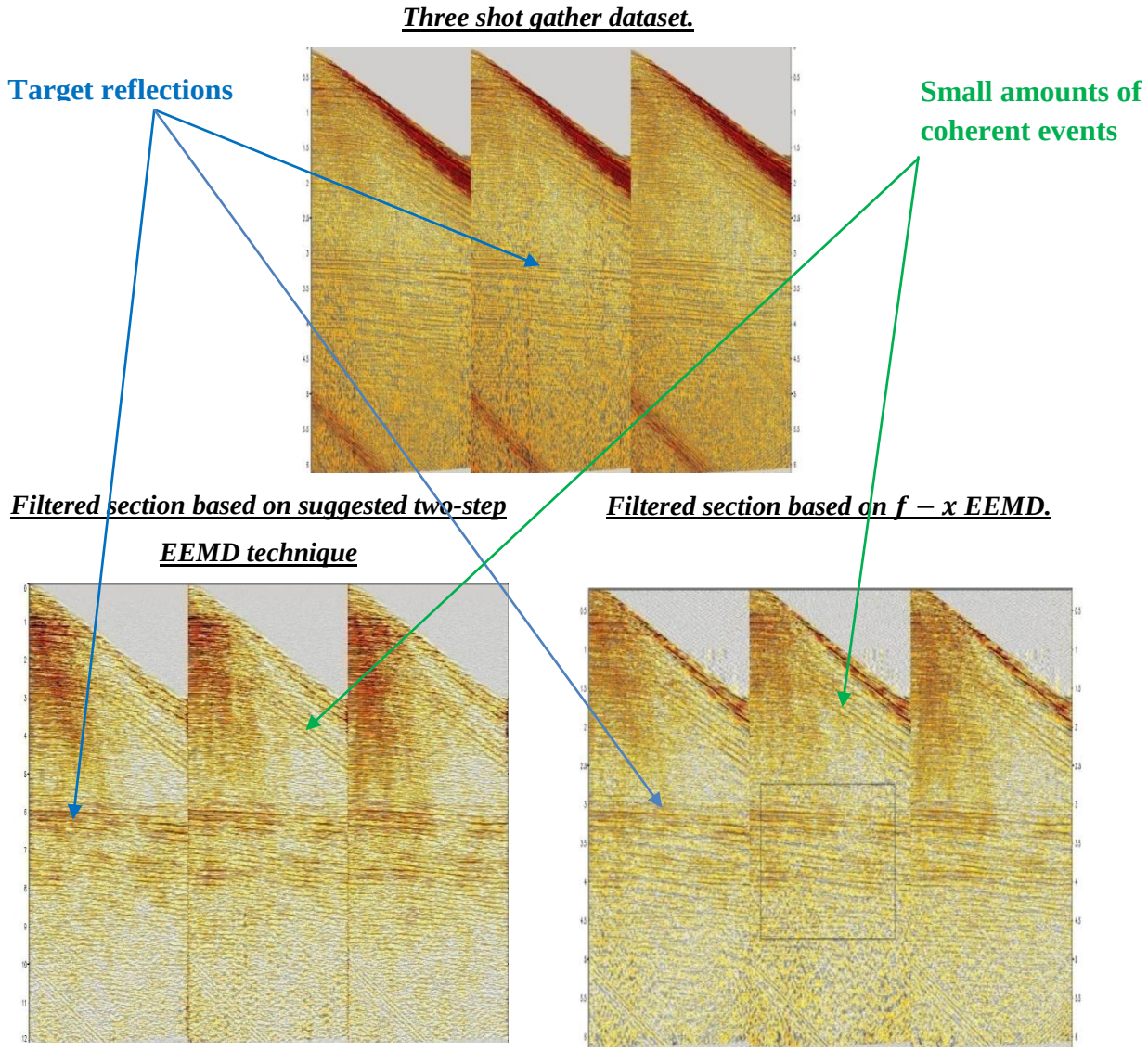

Figure 8.12: *Comparison between $t-x$ EEMD and $f-x$ EEMD filtering data.*

8.3 Discussion

In this chapter, I introduced a new filtering approach that uses the power of EMD/EEMD to extract the trend of the input data. I demonstrated for the first time that the EEMD technique can be used as a robust swell noise filter without essentially losing any of the target reflection energy. Flattening events can be performed on the whole dataset or within smaller parts of the data using time windows to reduce the computational time. Any coherent seismic event can be flattened and attenuated by subtracting the residual or eventually together with the few last IMFs from the input data.

Two important advantages exist in case of constant-time slice EEMD compared to the methodology of Bekara (2009):

i. Reduction of computational time by 50%.
ii. The ability to handle data with high percentage of high amplitude / low frequency noise such as swell noise.

When compared with the approach of Battista et al. (2007), the mixing modes between signal and noise are minimized, because essentially all noise located in the signal band has been attenuated by EEMD filtering on constant-time slices.

In order for the trend calculation to be robust, a certain length of a flat reflection is needed. This implies that shallower parts of the data will be more sensitive if NMO has been applied (due to muting of stretch).

Finally, I found that EEMD leads to better results than EMD based on the tests carried out in Chapters 6 and 7. For this reason, we tested this new approach using EEMD only.

9. CONCLUSIONS

Marine seismic acquisition is the most powerful geophysical method used in hydrocarbon exploration in the North Sea. Seismic data are always corrupted with various types of noise that reduce data quality. Noise such as refracted events, random, swell and interference noise are the most common ones in marine seismic acquisition. Noise attenuation therefore represents an important stage in seismic data processing to aid interpretation.

In this thesis, I have investigated the application of the Empirical Mode Decomposition (EMD) and Ensemble EMD techniques to attenuate random and coherent noise present in marine seismic data. The EMD acts as an auto-adaptive filter that determines which parts that can be removed from the original data. The main goal of this thesis was to find a reliable methodology to attenuate the seismic noise using EMD/EEMD. Marine seismic noise has been discussed in Chapter 2 and in Chapter 3 the most common seismic signal processing techniques have been reviewed with examples.

Empirical Mode Decomposition (EMD) (Huang et al. 1998) has been reviewed in Chapter 4. The purpose of using EMD, the algorithm and associated problems with solutions have been addressed in details. Extensive examples have been used to illustrate the behavior, stability and reliability of using the EMD/EEMD techniques in decomposing time series data. The EMD/EEMD algorithms developed in Matlab, and Fortran 90 are discussed in Chapter 5.

The application of EMD/EEMD in de-noising marine seismic data in the time –space domain has been investigated (Battista et al. 2007) in Chapter 6. The EMD/EEMD techniques have been applied to synthetic and real datasets contaminated with low-frequency/high-amplitude cable strum and swell noise. EEMD generated a narrower band of IMFs compared to EMD that reduced the mixing between signal and noise in the same IMF. However, EEMD did not solve the mixing mode problem completely.

The EEMD technique successfully attenuated cable strum and very low frequency swell noise (i.e. less than 15 Hz) in case the signal and noise fall in distinguishable frequency bands eliminating transition IMFs.

Another application of EMD/EEMD in de-noising marine seismic data in the frequency–space domain (Bekara and van der Baan, 2009) has been reviewed in Chapter 7. EEMD has been proven as a robust method to attenuate steeply dipping coherent noise. EEMD filtering produced small amplitude distortions compared to existing GeoCluster de-noise techniques but gave comparable results.

In Chapter 8, I proposed a new filtering method by applying EEMD on constant-time slices in the time-space domain to target swell noise and steeply dipping coherent noise. One important condition to apply this technique successfully is that the NMO correction must be carried out before decomposing the raw datasets. Consequently, NMO correction leads to a better separation between noise and the flat seismic events in the computed IMFs, by capturing the seismic events at the last IMFs and residual with the noise being captured by early IMFs. Therefore, the filtered section has enhanced SNR, and the method reduces the computational time by 50% compared to the frequency–space domain (Bekara and van der Baan, 2009) technique.

Most seismic filtering techniques are sensitive to the type of noise that corrupts the data; EMD is not an exception. Despite this fact, EMD and particularly EEMD, which I proposed for seismic de-noising in this thesis merges as a potentially effective technique for filtering seismic data.

The EMD/EEMD algorithms are simple of nature and in many cases gave results close in quality to those obtained from the more complex and robust techniques available in the commercial software package GeoCluster. However, there are still many issues that need to be addressed before these new techniques can be employed routinely within a professional environment. Among them are computational time and a more in depth qualitatively understanding of the fundamentals EMD/EEMD.

APPENDIX A

```
%  EMD/EEMD Matlab function that used in seismic de-noising tests
%
%   function IMFs=EEMD(Xin,Nstd,NE,itertions_max)
%
```

APPENDIX B

```
Subroutine EEMD(IMFs,Xin,Xsize, Max_NUM_iter ,maxIMF)

!   EEMD Fortran 90 function that used in seismic de-noising tests
!   function EEMD(IMFs,Xin,Xsize, Max_NUM_iter ,maxIMF)
!
```

REFERENCES

Alexandrov, T., S. Bianconcini, E. Bee Dagum, P. Maass, and T. Mc Elroy, 2009, A Review of Some Modern Approaches to the Problem of Trend Extraction. In Research Report Series, Statistics 2008-3, U.S. Census Bureau, Washington.

Battista, B. M., C. Knapp, T. McGee, and V. Goebel, 2007, Application of the empirical mode decomposition and Hilbert-Huang transform to seismic reflection data: Geophysics, **72**, no. 2, H29–H37.

Battista, B. M., 2007, Empirical mode decomposition MATLAB codes and data: http://software.seg.org/2007/0003.

Bekara, M., and M. van der Baan, 2007, Local singular value decomposition for signal enhancement of seismic data: Geophysics, **72**, no. 2, V59–V65.

Bekara, M., and M. van der Baan, 2009, Random and coherent noise attenuation by empirical mode decomposition: Geophysics, 74, no. 5, V89-V98.

Beylkin, G., 1987, Discrete Radon Transform: IEEE transactions on acoustics, speech, and signal processing, **35**, 162-172.

Bracewell, R. N., 1978, The Fourier Transform and its Applications, Second Edition: McGraw-Hill Book Co., New York.

Briggs, W. L., and V. E. Henson, 1995, The DFT: An Owner's Manual for the Discrete Fourier Transform: Society for Industrial and Applied Mathematics, Philadelphia.

Canales, L., 1984, Random noise reduction: 54thAnnual International Meeting, SEG, Expanded Abstracts, 525–527.

Cary, P., 1998, The simplest discrete Radon transform: Soc. of Expl. Geophys., 68th Ann. Internat, Mtg., 1999-2002.

Castle, R. J., 1994, A theory of normal moveout: Geophysics, 59, 983-999.

Chapman, S. J., 1998, Fortran 90/95 for Scientists and Engineers, 1st Ed., WCB/McGraw-Hill.

Chen, Q., N. Huang, S. Riemenschneider and Y. Xu, 2006, A B-spline approach for empirical mode decompositions. Advances in Computational Mathematics, 24, 171–195.

Damerval, C., S. Meignen, and V. Perrier, 2005, A fast algorithm for bidimensional EMD. IEEE Signal Processing Letters, 12(10), 701–704.

Datig, M., and T. Schlurmann, 2004, Performance and limitations of the Hilbert-Huang transformation (HHT) with an application to irregular water waves, Ocean Eng., 31, 1783 – 1834,doi:10.1016/j.oceaneng.2004.03.007.

De Boor, C., 2001, A Practical Guide to Splines, Revised Edition, Springer-Verlag, New York.

Diebold, J. B., and P. L. Stoffa, 1981, The traveltime equation, tau-p mapping, and inversion of common midpoint data, Geophysics 46, 238-254.

Elboth, T., D. Hermansen, and O. Andreassen, 2009, Some unusual types of noise: EAGE Technical Program Expanded Abstracts, **71**, 5658.

Elboth, T., H. Qaisrani, and T. Hertweck, 2008, De-noising seismic data in the time-frequency domain: SEG Technical Program Expanded Abstracts, **27**.

Evans, B.J., 1997, A handbook for Seismic Data Acquisition in Exploration, SEG.

Excess Geophysics, 1999, Seismic Tutorial. [Online]. [Cited: 20 May 2011.]: http://www.xsgeo.com.

Flandrin, P., and P. Gonçalves, 2004, Empirical mode decompositions as data-driven wavelet-like expansions for stochastic processes: International Journal of Wavelets, Multi-resolution and Information Processes, **2**, 477–496.

Frei, M. G., and I, Osorio, 2006, Intrinsic time-scale decomposition: Time-Frequency-Energy analysis and real-time filtering of non-stationary signals. Proceedings of the Royal Society A, First Cite Early Online Publishing, London, U.K.

Galbraith, M., 1991, Random noise attenuation by $f-x$ prediction: A tutorial: 61st Annual International Meeting, SEG, Expanded Abstracts, 1428–1431.

Gelius, L. J., and H. Westerdahl, 1997, Seismic Noise Modeling, Journal of Seismic Exploration, Vol. 6, pp. 351-366.

Gulunay, N., 1986, $F-x$ deconvolution and complex wiener prediction filter: 56th Annual Internat. Mtg., Soc. Expl. Geophys., Expanded Abstracts, Session:POS2.10.

Gulunay, N., 1990, F-X domain least-squares tau-p and tau-q, 60th Ann. Internat. Mtg: Soc. of Expl. Geophys., 1607-1610.

Gulunay, N., M. Magesan, and S. Baldock., 2001, Spatial prediction filters for attenuation of seismic interference noise. CGG. Americas Inc.

Harris, P. E., and R. E. White, 1997, Improving the performance of $f-x$ prediction at low signal- to-noise ratios: Geophysical Prospecting, **45**, 269–302.

Hassan, H., 2005, Empirical mode decomposition (EMD) of potential field data: Airborne gravity data as an example: 75th Annual International Meeting, SEG, Expanded Abstracts, 704–07.

Hassan, H., 2006, Empirical Mode Decomposition (EMD) of Turner Valley Airborne Gravity Data in the Foothills of Alberta, Canada, Expanded Abstract for CSPG-CSWL-CSEG convention.

Hatton, L., M. H. Worthington, J. Makin, 1986, Seismic Data Processing: Theory and Practice, Blackwell Science.

Hornbostel, S., 1991, Spatial prediction filtering in the $t-x$ and $f-x$ domain: Geophysics, **56**, no. 12, 2019-2026.

Huang, N. E., Z. Shen, S. R. Long, M. L. Wu, H. H. Shih, Q. Zheng, N. C.Yen, C. C. Tung, and H. H. Liu, 1998, The empirical mode decomposition and Hilbert spectrum for nonlinear and nonstationary time series analysis: Proceedings of the Royal Society of London Series A Mathematical Physical and Engineering Sciences, **454**, 903–995.

Huang, N. E., C. C. Chern, K. Huang, L. W. Salvino, S. R. Long, and K. L. Fan, 2001, A new spectral representation of earthquake data: Hilbert spectral analysis of station TCU129, Chi-Chi,Taiwan, 21 September 1999, Bull. Seismol. Soc. Am., 91, 1310– 338, doi:10.1785/0120000735.

Huang, N. E., M. Wu, W. Qu, S. Long, and S. Shen, 2003, Applications of Hilbert–Huang transform to non-stationary financial time series analysis. Appl Stochastic Models Business Industry; 19: 245–68.

Huang, N. E., 2005, Introduction to the Hilbert-Huang transform and its related mathematical problems, in the book Hilbert-Huang Transform and its Applications, (eds. N.E. Huang and S. S. P. Shen), World Scientific.

Huang, N. E., and N. O. Attoh-Okine, 2005, Hilbert-Huang Transforms in Engineering, 313 pp., CRC Press, Boca Raton,Fla.

Huang, N. E., and Wu, Z. , 2008, A review on Hilbert-Huang transform: Method and its applications to geophysical studies, Rev. Geophys., 46, RG2006, doi:10.1029/2007RG000228.

Huang, N. E., Z. Wu, S. R. Long, K. C. Arnold, K. Blank, and T. W. Liu, 2009, On instantaneous frequency, Adv. Adapt. Advances in Adaptive Data Analysis, Vol. 1, No.2, 177-229.

Jeng, Y., M. J. Lin, C. S. Chen, and Y. H. Wang, 2007, Noise reduction and data recovery for a VLF-EM survey using a nonlinear decomposition method, Geophysics **72**, F223.

Lancaster, P., K. Salkauskas, 1986, Curve and surface fitting, an introduction, Academic press.

Linderhed, A., 2002, 2D empirical mode decompositions in the spirit of image compression: Society of Photo-Optical Instrumentation Engineers (SPIE) Conference Series, 1–8.

Linderhed, A., 2004, Image compression based on empirical mode decomposition. Proceedings of the International Conference on Image and Graphics, Hong Kong, China, pp. 430–433.

Linderhed, A., 2004, Adaptive image compression with wavelet packets and empirical mode decomposition: Linkoping University: Ph.D. thesis, Linkoping, Sweden.

Linderhed, A., 2005, Variable sampling of the empirical mode decomposition of two-dimensional signals. International Journal of Wavelets, Multiresolution and Information Processing, 3(3), 435–452.

Liu, X., 1999, Ground roll suppression using the Karhunen-Loeve transform: Geophysics,**64**, 564-566.

Karagiannis, A., 2009, Constantine Ph. Electromagnetic Radiation Monitoring Time Series Analysis Based on Empirical Mode Decomposition. BIOEM, Davos, Switzerland.

Kaslovsky, D. N., F. G. Meyer, 2010, Noise corruption of Empirical Mode Decomposition and its effect on instantaneous frequency, Advances in Adaptive Data Analysis, Vol. 2, No. 3, 373-396.

Kijewski-Correa, T. L. and A. Kareem, 2007, Performance of wavelet transform and Empirical Mode Decomposition in extracting signals embedded in noise. *J. Eng. Mech-ASCE.*, 133: 849–852.

Kizhner, S., T.P. Flatley, N.E. Huang, K. Blank, E. Conwell, 2004, On the Hilbert-Huang Transform Data Processing System Development, 2004 IEEE Aerospace Conference Proceedings, vol. 3, pp. 1961–1979.

Magrin-Chagnolleau, I., 2002, EMD Matlab code: http://www.ddl.ish-lyon.cnrs.fr/membres.

Magrin-Chagnolleau, I., and R. Baraniuk, 1999, Empirical mode decomposition based time- frequency attributes: 69th Annual International Meeting, SEG, Expanded Abstracts, 1949–1952.

McGee, T., 2000, Pushing the limits of high-resolution in marine seismic profiling: Journal of Environmental and Engineering Geophysics, **5**, 43–53.

Olhovich, V. A., 1964, The causes of Noise in Seismic reflection and Refraction Work: Geophysics. Vol. XXIX, 6, pp. 1015-1030.

Poularikas, A. D., 2010, Transforms and Applications Hand Book, 3rd ed., CRC Press. Taylor & Francis Group.

Presterud, I. V., 2009, Time Frequency De-noising of Seismic Data: University of Oslo: M.Sc. thesis, Oslo, Norway.

Rao, A. R., 2008, Hilbert-Huang transform analysis of hydrological and environmental time series, pringer, 244 p.

Rilling, G., P. Flandrin, and P. Gonçalvès, 2002, Empirical mode decomposition MATLAB codes: http://perso.ens-lyon.fr/patrick.flandrin/emd.html

Rilling, G., P. Flandrin, and P. Gonçalvès, 2003, On empirical decomposition and its algorithms: Proceesing IEEE-EURASIP Workshop on Nonlinear Signal Image Process, Grado, Italy.

Rilling, G., P. Flandrin, and P. Gonçalvès, 2004a, Detrending and denoising with empirical mode decomposition: Eusipco, 12th European Signal Processing Conference.

Rilling, G., P. Flandrin, and P. Gonçalvès, 2004b, Empirical mode decomposition as a filter bank: IEEE Signal Processing Letters, **11**, 112–114.

Rilling, G., and P. Flandrin, 2009, Sampling effects on the empirical mode decomposition: Advanced adaptive data analysis, **1**, 43–59.

Russel, B., D. Hampson, and J. Chun, 1990a, Noise elimination and the Radon transform, part 1: The Leading Edge, 9, No. 10, 18–23.

Russel, B., D. Hampson, and J. Chun, 1990b, Noise elimination and the Radon transform, part 2: The Leading Edge, 9, No. 11, 31–37.

Sheriff, R. E., and L. P. Geldart, 1995, Exploration Seismology, 2nd ed, Cambridge Univ. Press.

Sipola, T., 2009, Applying Hilbert-Huang Transform to Mismatch Negativity: UNIVERSITY OF JYVASKYLA: M.Sc. thesis, Finland.

Spitz, S., 1991, Seismic trace interpolation in the $f-x$ domain: Geophysics, **56**, no. 6, 785-794.

Stein, S., and M. Wysession, 2003, An Introduction to Seismology, Earthquakes and Earth Structure, Blackwell Publication Data.

Suling, J., G. Yanqin, W. Qiang, and Z. Jian, 2009, Trend Extraction and Similarity Matching of Financial Time Series Based on EMD Method. In: World Congress on Engineering and Computer Science, 20-22 Oct 2009, San Francisco.

Telford, W. M., L. P. Geldart, and R. E. Sheriff, 1990, Applied Geophysics, 2nd ed., Cambridge Univ. Press.

Tufts, D.W., and R. Kumaresan, 1980, Estimation of frequencies of multiple sinusoids: Making linear prediction perform like maximum likelihood: Proceedings of the IEEE, **70**, 975–989.

Wu, Z., 2010, Empirical mode decomposition MATLAB codes: http://rcada.ncu.edu.tw.

Wu, Z., and N. E. Huang, 2004, Ensemble Empirical Mode Decomposition: a noise-assisted data analysis method, Centre for Ocean-Land-Atmosphere Studies, Tech. Rep. No.173.

Wu, Z., and N. E. Huang, 2009, Ensemble Empirical Mode Decomposition: a noise-assisted data analysis method, Advances in Adaptive Data Analysis, Vol. 1, No. 1, 1–41.

Wu, Z., N. E. Huang, and X. Chen, 2009, The Multi-Dimensional Ensemble Empirical Mode Decomposition Method, Advances in Adaptive Data Analysis, Vol. 1, No. 3, 339–372.

Xu, Y., B. Liu, J. Liu, and S. Riemenschneider, 2006, Two-dimensional empirical mode decomposition by finite elements. Proceedings of the Royal Society A, 462, 3081–3096.

Yilmaz, O., 2001, Seismic data Analysis: Processing, Inversion, and Interpretation of Seismic Data Soc. Expl. Geophys.

Zhou, N., D. Trudnowski, J. W. Pierre, S. Sarawgi, and N. Bhatt, 2008, An algorithm for removing trends from power-system oscillation data. In: IEEE PES. July 20-24, Pittsburgh, PA.